The Dissertation Committee for Benjamin Andrew Stephens
certifies that this is the approved version of the following dissertation:

Investigating a Tropical Atmospheric Trigger for Abrupt Climate Change

Committee:

Philip J. Morrison, Supervisor

Charles S. Jackson, Co-Supervisor

Richard Fitzpatrick

Irene Gamba

Claude W. Horton

Michael Marder

Investigating a Tropical Atmospheric Trigger for Abrupt Climate Change

by

Benjamin Andrew Stephens

DISSERTATION

Presented to the Faculty of the Graduate School of

The University of Texas at Austin

in Partial Fulfillment

of the Requirements

for the Degree of

DOCTOR OF PHILOSOPHY

THE UNIVERSITY OF TEXAS AT AUSTIN

December 2019

Dedicated to my parents Jeff and Sylvia.

Acknowledgments

Many people helped make this dissertation possible. First and foremost, thank you to my adviser Charles S. Jackson for welcoming me to the UT Institute for Geophysics and giving me the opportunity to work on these interesting problems, along with always being happy to talk and generous with his time. I also extend a big thank you to Philip J. Morrison for agreeing to co-advise me as I pursued a topic outside the UT Physics Department and for offering his advice and insights at crucial points along the way.

Special thanks to my former colleague Benj Wagman, who also studied under Charles, for his comments and collaboration. Thank you to Pedro di Nezio, Dargan Frierson, Phil Rasch, Courtney Schumacher, and three anonymous referees, whose comments and criticisms helped make Chapter 3 of this thesis possible. Thanks also to Adam Sobel and Shuguang Wang, whose version of the WRF model I used in the research for Chapter 4, and especially to Shuguang who happily answered many emails about model details.

Finally I thank my family and friends, with particular thanks to my parents, who supported and encouraged me as I sought degree after degree (this is the last one, I promise), and to my wife Sarah, whose awesome advice and unfailing moral support—especially after our son Seth was born—got me through many struggles in research and writing.

Investigating a Tropical Atmospheric Trigger for Abrupt Climate Change

Benjamin Andrew Stephens, Ph.D.
The University of Texas at Austin, 2019

Supervisor: Philip J. Morrison
Co-Supervisor: Charles S. Jackson

Abrupt climate change is known to have occurred in the distant past and may be a possibility in the future. Dominant theories of abrupt change have located the trigger for such change in the North Atlantic ocean, but some evidence suggests that the tropical atmosphere may play an important role, and advisory bodies have recommended further investigation. Using both single-column and general circulation models, both of which partition rainfall between parameterized convection (giving "convective" rain) and cloud microphysics (giving "large-scale" rain), I present findings indicating that the tropical atmosphere could indeed act as a trigger for abrupt change. I first show that different ratios of tropical rainfall partitioning in general circulation models are associated with very different types of large-scale atmospheric circulation, affecting also the response to CO_2 forcing. Secondly, I demonstrate that abrupt changes in rainfall partitioning can be induced in a single-column model using physics similar to that of a global model.

Table of Contents

List of Tables

List of Figures

Chapter 1

Introduction

It is known that Earth's climate has changed abruptly in the distant past. Early theories of global climate change, informed by physical evidence of past "ice ages" and based on the principles of uniformitarian geology, assumed gradual change over many years. By the mid-20th century, this gradual change was thought by some to be a consequence of long-term "Milankovitch cycles" in Earth's motion around the sun, whereby insolation—the amount of solar radiation absorbed by the climate system—changes slowly due to variations in Earth's axial tilt, the eccentricity of Earth's orbit, the precession of the equinoxes, and other effects of our planet's complex motion [116].

Over the course of the twentieth century, however, it became clear that the reality of climate change is more complex. Temperatures were colder on average before the onset of the Holocene epoch about 10,000 years ago (Figure 1.1), which will not surprise anyone who has seen the *Ice Age* movies, but the Pleistocene's dramatic variability is probably less well-known. Scandinavian pollen studies of the 1930s indicated the presence of a "Younger Dryas" cooling event at the end of the Pleistocene epoch roughly 11,500 years ago, whose termination involved as much as 5-10°C warming over Greenland in as

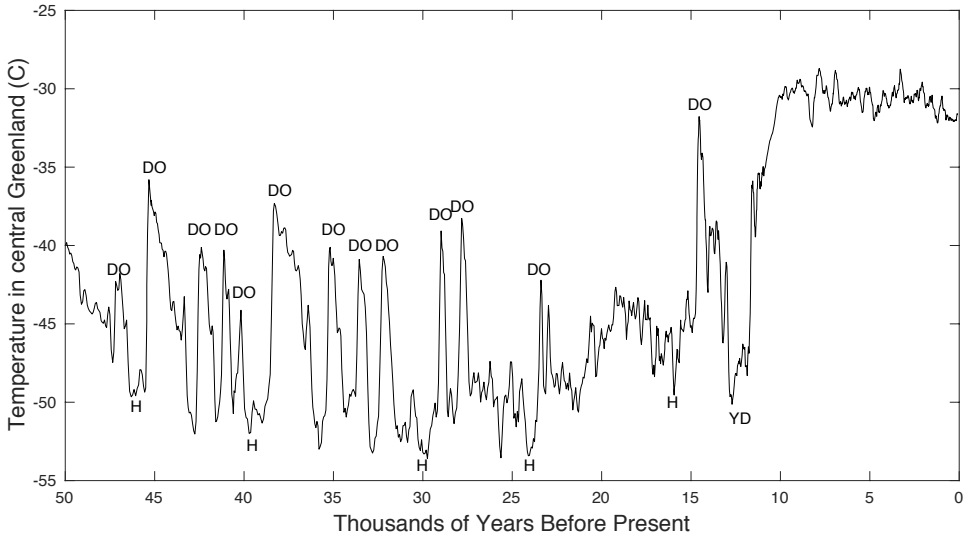

Figure 1.1: Greenland ice core temperature data for the last 50,000 years [2], retrieved from the National Oceanic and Atmospheric Administration (NOAA) website (www.ncdc.noaa.gov). Labeled are thirteen Dansgaard-Oeschger warming events (DO), five Heinrich cooling events (H), and the famous Younger Dryas cooling event (YD). The Younger Dryas's abrupt termination ended the Pleistocene geological epoch, leading into the relatively stable, warmer, and wetter Holocene epoch of the last ∼10,000 years.

little as a few decades [2]. This, along with additional discoveries such as the Dansgaard-Oeschger and Heinrich events—rapid warming and cooling events, respectively, indicated by periodic oscillations in climate proxy records going back deep into the Pleistocene—indicated that climate could change dramatically on large spatial scales well within the span of a human lifetime [116].

Unfortunately, rapid and far-reaching fluctuations in climate such as those shown in Figure 1.1 are not well understood. Various hypotheses have been advanced to explain them, with especial attention having been paid to the theory of abrupt shutdown of the Atlantic Meridional Overturning Circulation (AMOC) as a potential trigger for these events [9], but no consensus has

emerged, and strong arguments have been made against the AMOC[1] hypothesis [124]. The lack of scientific understanding of these events is troubling in the light of anthropogenic climate change and the possibility that CO_2 forcing could push the climate system across various theorized "tipping points" [55], with drastic consequences for some populations—often those least prepared to deal with them. Greater understanding of abrupt climate change is therefore essential both in evaluating the future likelihood of such events and in helping people to prepare for and manage them, should they be likely to occur.

While the ocean has heretofore been the primary focus of abrupt climate change studies, another conceivable mechanism for abrupt change, affecting especially worldwide precipitation, would be changes in atmospheric circulation. As the National Research Council wrote in its 2013 report on abrupt climate change, "The likelihood of abrupt changes in the atmospheric circulation remains unclear... As such, understanding abrupt changes in—and due to—the atmospheric circulation remains a key topic for future research" [26]. Fortunately, we are not without tools to approach this topic. This doctoral thesis draws on atmospheric physics, nonlinear dynamics, statistical methods, and two types of numerical climate model to address the question of how rainfall partitioning in models—i.e., partitioning of total precipitation between different types (primarily "convective" and "large-scale" rain), to be described in Chapter 2—relates to abrupt transitions and large-scale atmospheric effects in models. Exploration of this relationship was inspired by an unexpected ob-

[1] Appendix A contains a list of abbreviations used throughout this thesis.

servation, also described in Chapter 2, of abrupt change in a global model, in which sudden atmospheric circulatory changes which caused drying throughout the tropics seemed connected to a shift in the model's partitioning of tropical rainfall.

In Chapters 3 and 4 respectively, I draw two main conclusions: first, in global atmospheric models there are strong correlations between a model's rainfall partitioning and the patterns it shows in large-scale tropical circulation and in its response to CO_2 forcing. This suggests that abrupt changes in model rainfall partitioning may lead to abrupt climate change throughout the tropics; to the extent such changes are physical, they may represent real possibilities for abrupt change. Secondly, I find that under appropriate conditions, a one-dimensional "single-column" atmospheric model can be made to robustly exhibit just the kind of abrupt change in rainfall partitioning of interest in global models, strengthening the case for the physicality of such transitions.

Chapter 2

Background & Motivation

This chapter will prepare the reader to understand the methods and results described in Chapters 3 and 4. Section 2.1 covers the basics of atmospheric physics, including convection and cloud microphysics, and Section 2.2 describes how rainfall is typically handled by numerical atmospheric models. I then describe the basics of single-column atmospheric models in Section 2.3, including how they differ from global models and how they can be modified to simulate aspects of the large-scale dynamics. Sections 2.4 and 2.5 review the fundamentals of abrupt climate change and describe an intriguing observation in a global model which has inspired this study. Section 2.6 concludes with a review of literature relevant to the chapters that follow.

2.1 Atmospheric physics

A simple dry atmosphere is a fluid described at any location by six quantities: temperature, pressure, density, and the three components of wind velocity. Such a simple model could be elaborated in various ways, but the most important addition relevant to Earth's atmosphere is water vapor, typically quantified by the ratio of water vapor mass to dry air mass, called the

Name	Definition
Water vapor mixing ratio (q)	water vapor mass / dry air mass
Specific humidity	water vapor mass / total mass
Vapor pressure (e)	partial pressure of water vapor
Relative humidity (e/e_s)	vapor pressure / saturation vapor pressure

Table 2.1: Common ways of quantifying the water vapor content of air, with symbols given for those appearing in equations in this thesis.

mixing ratio $q \equiv m_v/m_d$. (Table 2.1 gives the definitions of several ways of quantifying the water vapor content of air, all of which are used in this thesis.) One can therefore describe a moist atmosphere with seven "primitive equations", beginning with Newton's second law,

$$\rho\vec{a} = -\nabla p + \rho\vec{g} - 2\rho\vec{\Omega} \times \vec{v} - \rho\vec{\Omega} \times (\vec{\Omega} \times \vec{r}) + \vec{f}. \tag{2.1}$$

Here ρ is mass density and the terms on the right-hand side are, in order from left to right, the pressure gradient force, the force due to gravity, the Coriolis and centrifugal forces, and frictional damping (including viscous and turbulent effects). This yields three equations, one for each spatial dimension. The remaining equations are the first law of thermodynamics,

$$c_p\, dT = \frac{dp}{\rho} + Q \tag{2.2}$$

(where c_p is the specific heat capacity of dry air at constant pressure and Q represents diabatic heating per unit mass), the ideal gas law,

$$p = \rho R_d T \tag{2.3}$$

(written in terms of mass density ρ and the specific gas constant for dry air R_d), and mass conservation equations for dry air and for water vapor:

$$\frac{\partial \rho}{\partial t} + \nabla \cdot (\rho \vec{v}) = 0 \tag{2.4}$$

$$\frac{\partial (\rho q)}{\partial t} + \nabla \cdot (\rho q \vec{v}) = M + \rho E. \tag{2.5}$$

Here M and E, respectively, are water vapor sinks (e.g., condensation) and sources (e.g., evaporation).

It is worth expanding one of these equations in spherical coordinates in order to further clarify some notation and terminology common in geophysics. Expanding (2.4), one obtains

$$\begin{aligned} &\frac{\partial \rho}{\partial t} + \frac{1}{r \cos\phi} \frac{\partial}{\partial \lambda}(\rho u) + \frac{1}{r \cos\phi} \frac{\partial}{\partial \phi}(\cos\phi \rho v) + \frac{1}{r^2} \frac{\partial}{\partial r}\left(r^2 \rho w\right) = 0 \\ &\quad \Longrightarrow \frac{\partial \rho}{\partial t} + \frac{1}{r_E \cos\phi} \left[\frac{\partial}{\partial \lambda}(\rho u) + \frac{\partial}{\partial \phi}(\cos\phi \rho v) \right] + \frac{\partial}{\partial z}(\rho w) = 0 \end{aligned}$$

(where in the second equation the "shallowness approximation" [115] has been used[1]). Worth emphasizing here is that in a geophysical context, λ is typically used as the east-west, longitudinal, or *zonal* coordinate, ϕ is typically used as the north-south, latitudinal or *meridional* coordinate, and z denotes vertical height above the earth's surface. The (λ, ϕ, z) notation and the terms "zonal" and "meridional" are used throughout this dissertation.

There are a number of alternative ways of quantifying temperature, two of which will be useful in this thesis. The more important of the two is

[1]Under the shallowness approximation, the vertical distance above the ground z is taken to be much less than the mean radius of the earth, $z \ll r_E$, allowing one to replace r $(= r_E + z)$ with r_E and dr with dz.

potential temperature, denoted θ and defined as

$$\theta \equiv T \left(\frac{p_0}{p} \right)^{R_d/c_p}, \tag{2.6}$$

where p_0 is the surface pressure. The potential temperature is the temperature a parcel of air would reach if brought adiabatically to the surface. Second is the *virtual temperature* T_v, which can simplify expressions when dealing with moist air. The virtual temperature is defined as

$$T_v \equiv \left(\frac{1 + q/\varepsilon}{1 + q} \right) T, \tag{2.7}$$

where $\varepsilon \equiv R_d/R_v$ is the ratio of the specific gas constant for dry air and that for water vapor R_v. The ideal gas law (2.3), for example, can be written simply as $p = \rho R_d T_v$ to incorporate the presence of moisture.[2]

Finally, it is useful to be familiar with the conventions of using pressure as a vertical coordinate and of expressing vertical velocity in terms of pressure. The *pressure velocity* ω, defined as

$$\omega \equiv \frac{dp}{dt} \tag{2.8}$$

with units of [pressure]/[time], is often used in place of $w = dz/dt$ in an atmospheric setting. The rationale here is that in atmospheric physics, pressure is often used as the vertical coordinate rather than height. (Note that by $\omega = -\rho g w$ the sign of ω is opposite to the direction of the vertical velocity

[2]Some derivations, including for the potential and virtual temperatures, can be found in Appendix B.

w—i.e., negative ω means upward motion.) Hence when a material derivative of some quantity A is expanded in terms of partial derivatives, the zonal and meridional (or, considered together, the "horizontal") components are often separated from the vertical component:

$$\frac{dA}{dt} = \frac{\partial A}{\partial t} + \vec{u}_h \cdot \nabla_h A + \omega \frac{\partial A}{\partial p},$$

where $\vec{u}_h$ and ∇_h contain only the horizontal velocities and derivatives respectively.

Eq. 2.2 can now be written more simply in terms of θ and ω, something useful to show, because this form of (2.2) will be used exclusively in Chapter 4. Manipulating the ideal gas law, one finds

$$\frac{dT}{T} = \frac{R_d}{c_p}\frac{dp}{p} + \frac{Q}{c_p T}. \tag{2.9}$$

From the definition of potential temperature, one also finds

$$\begin{aligned} dT &= d\theta \left(\frac{p}{p_0}\right)^{R_d/c_p} + \theta \left(\frac{p}{p_0}\right)^{R_d/c_p} \frac{R_d}{c_p}\frac{dp}{p} \\ \Longrightarrow \frac{dT}{T} &= \frac{d\theta}{\theta} + \frac{R_d}{c_p}\frac{dp}{p}. \end{aligned} \tag{2.10}$$

Combining (2.9) and (2.10), (2.2) becomes simply

$$\frac{d\theta}{dt} = Q' \qquad \text{or} \qquad \frac{\partial \theta}{\partial t} + \vec{u}_h \cdot \nabla_h \theta + \omega \frac{\partial \theta}{\partial p} = Q',$$

where $Q' \equiv (\theta / c_p T)\, Q$. In this version of (2.2), the adiabatic term has been absorbed within the potential temperature.

2.1.1 Atmospheric stability and convection

The dominant physical relationship governing the atmosphere is approximate hydrostatic equilibrium—this refers to the simple balance between gravity pulling down on the atmosphere and pressure holding it up. This is quickly derived from the vertical component of (2.1), assuming frictional, Coriolis, and centrifugal effects and vertical accelerations are small:

$$\frac{dp}{dz} = -\rho g. \tag{2.11}$$

To describe convective motion as a response to an unstable atmospheric stratification, one can begin by considering dry or unsaturated air—moisture is unnecessary, after all, for convection to occur. The basis of atmospheric stability is buoyancy: if a parcel of air of density ρ' is surrounded by ambient air of density ρ, then the net force on that parcel is the (upward) buoyant force plus the (downward) force of gravity: $F_{\text{net}} = gV\,(\rho - \rho')$. Using the ideal gas law (2.3), one can write the acceleration as

$$a = g\left(\frac{\rho - \rho'}{\rho'}\right) = g\left(\frac{T' - T}{T}\right), \tag{2.12}$$

which implies an upward acceleration if the parcel temperature T' is higher than the ambient temperature T and a downward acceleration if the opposite is true. This is consistent with the idea that "warm air rises."

Eq. (2.12) leads to consideration of how quickly temperature decreases with height—both that of a rising air parcel and that of the actual environment. The rate of temperature decrease with height is called the *lapse rate*,

and Eq. (2.11) is easily combined with the adiabatic version of (2.2) to derive what is known as the *dry adiabatic lapse rate* Γ_d:

$$\Gamma_d \equiv -\frac{dT}{dz} = \frac{g}{c_p}. \tag{2.13}$$

From this one concludes that, in the absence of condensation or other diabatic effects, a parcel of air will cool at a rate of approximately 10°C km^{-1} as it rises. If a parcel, upon rising and cooling slightly, finds itself surrounded by warmer environmental air, buoyant forces will return it to its previous height; hence, the criterion for convective stability for unsaturated air is that the environmental lapse rate Γ_e be less than the dry adiabatic lapse rate:

$$\Gamma_e < \Gamma_d \quad \text{(stable)}$$

$$\Gamma_e > \Gamma_d \quad \text{(unstable)}.$$

(Part of the usefulness of the potential temperature θ is that stability for dry air can be expressed simply as $\partial\theta/\partial z \geq 0$.)

When moisture is present and the rising parcel is nearing saturation, condensation and diabatic heating are possible and can significantly enhance the upward convective motion. In this context it is useful to quantify the water vapor content of the air using its vapor pressure e, which obeys the ideal gas law for water vapor,

$$e = \rho_v R_v T, \tag{2.14}$$

where ρ_v is the water vapor density. As a rising air parcel cools, it will eventually reach saturation at a height called the lifting condensation level (LCL),

and diabatic heating will commence as water vapor condenses. Beyond this point, the condensing parcel will cool more slowly at the *moist adiabatic lapse rate*[3] Γ_m, which can be derived from (2.2) with $Q = -L\,dq_s$, where L is the latent heat of vaporization and dq_s represents a differential change in the saturation mixing ratio. Together with the Clausius-Clapeyron equation,

$$\frac{de_s}{dT} = \frac{Le_s}{R_v T^2}, \tag{2.15}$$

where e_s is the saturation partial pressure, (2.2), (2.3), (2.11), and (2.14) can be shown to yield

$$\Gamma_m \equiv -\frac{dT}{dz} = \frac{g}{c_p}\left(1 + \frac{Lq_s}{RT}\right)\left(1 + \frac{L^2 q_s}{c_p R_v T^2}\right)^{-1}. \tag{2.16}$$

Above the LCL, the criterion for convective stability becomes $\Gamma_e < \Gamma_m$. It is worth noting that if the environmental lapse rate is between the moist and dry adiabatic lapse rates ($\Gamma_m < \Gamma_e < \Gamma_d$), then *conditional instability* is possible. A rising parcel first cooling at the dry adiabatic lapse may return to its previous height if vertical motions are weak, but if the parcel is forcibly raised beyond its LCL, it will cool more slowly at the moist adiabatic lapse rate. If lifted past a height called the level of free convection (LFC), the parcel will become warmer than the environmental air and continue to ascend on its own.

At a certain height called the equilibrium level (EL), the temperature of the rising parcel will become equal to that of the environment, at which

[3]This terminology may be confusing. While the moist "adiabatic" lapse rate takes account of *diabatic* latent heating due to water vapor condensation, the process is considered adiabatic as long as the condensation products do not leave the parcel. Otherwise the term *pseudoadiabatic lapse rate* may be used (e.g., see [87, 112]).

point convective lifting will cease. During the parcel's ascent, water vapor that condenses may either form clouds or rain out, and falling rain can also re-evaporate (see the next section on cloud microphysics).

Two related measures of the potential for convection to occur will appear later in this thesis. These are the *convective available potential energy* (CAPE) and *convective inhibition* (CIN), both usually measured in joules per kilogram. Essentially, CAPE measures energy encouraging convection and CIN measures energy discouraging convection. Mathematically, CAPE is the integral of buoyancy (Eq. 2.12, but where moisture is taken into account using the virtual temperature) from the LFC to the EL,

$$\text{CAPE} = \int_{\text{LFC}}^{\text{EL}} g \left(\frac{T_v' - T_v}{T_v} \right) \, dz, \tag{2.17}$$

and CIN is the same integral from the surface to the LFC:

$$\text{CIN} = \int_{0}^{\text{LFC}} g \left(\frac{T_v' - T_v}{T_v} \right) \, dz. \tag{2.18}$$

2.1.2 Cloud microphysics

Cloud microphysics—the study of processes by which water vapor condenses into liquid droplets or ice crystals and how those condensates interact with each other and precipitate—is complex and can only be briefly surveyed here. As water vapor is lifted higher into the atmosphere, whether by convection, frontal lifting, or other processes, relative humidity increases; eventually the air can become saturated with moisture and droplets can form. The details

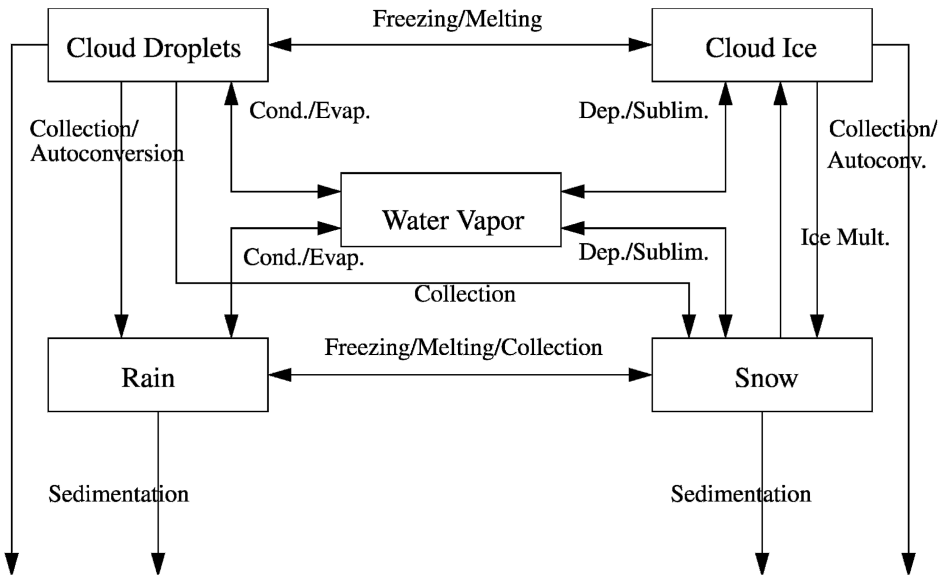

Figure 2.1: Cloud microphysics processes, including rain and snow but neglecting other forms of precipitation (e.g., hail or graupel). Diagram from Morrison et al. [65].

of droplet nucleation depend on the temperature of the cloud, which determines whether only water droplets can form (typically around aerosols) or whether ice crystals can also exist. Once droplets or crystals form, they can grow in size via various processes including condensation (for later reference, spontaneous conversion of cloud water to rain is called *autoconversion*) and collision/coalescence, and eventually they can grow large enough to precipitate out under the force of gravity. Falling raindrops can also re-evaporate, cooling the surrounding air—this phenomenon will be important in Chapter 4. However, as Figure 2.1 demonstrates, there are constant interactions between the different components of this type of microphysical system, and even in Figure 2.1, certain components such as hail are excluded for simplicity.

2.1.3 Atmospheric dynamics

The following is a description of some essential features of atmospheric circulation and dynamics relevant to the rest of the thesis. One of the most difficult elements of the set of equations presented above is the diabatic heating term Q in (2.2), which can be given no general analytical form due to the many and complex diabatic heating effects present in the climate system, including radiative heating, condensation and evaporation processes, turbulent heat fluxes, and so on [81]. Nevertheless, the primary driver of the climate system is solar radiation, which falls disproportionately near the equator. This radiative heating, some of which is absorbed by the atmosphere and some by the surface, supplies both the heat energy leading to convection and the evaporation from the land or ocean surface supplying the moisture to the air.

Convective lifting is the primary means by which energy is vertically transported high into the tropical free troposphere [84]—the *troposphere* being the lowest $\sim$10 km of the atmosphere where most weather occurs, including the *atmospheric boundary layer* near the surface and the *free troposphere* above—and the consequent latent heat release via upward water vapor transport provides roughly a third of the energy driving the atmospheric circulation [15]. At high altitudes, the now dry rising air diverges on either side toward the poles carrying primarily gravitational potential energy. Under different planetary conditions (a slower rotation for example), this air might travel nearly to the pole before descending and returning toward the equator, but on Earth the high-level air flows only to about 30° north or south before descending and

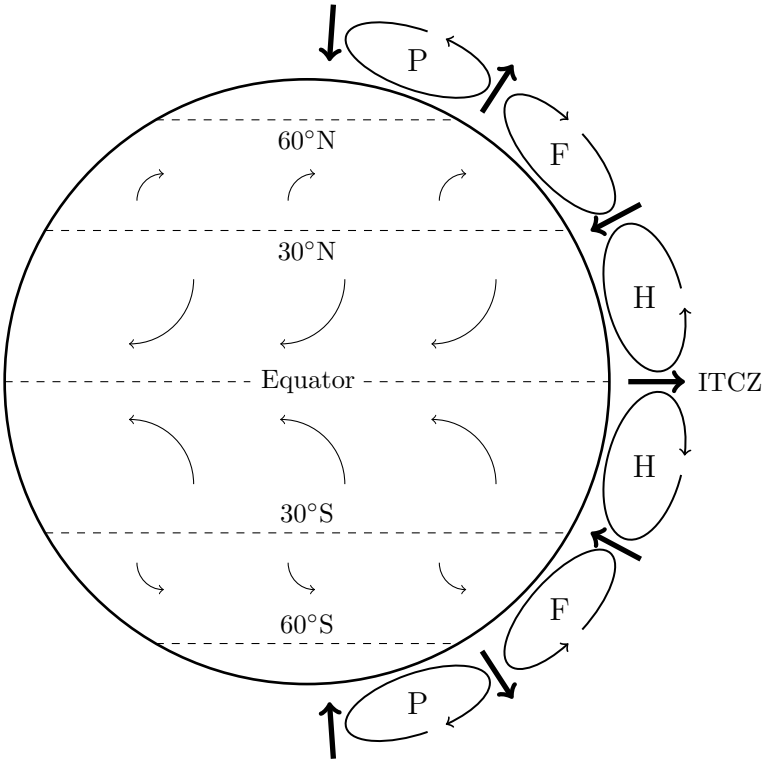

Figure 2.2: Major features of the global atmospheric circulation. Arrows indicate the direction of large-scale wind flow. The Intertropical Convergence Zone (ITCZ) is a band of highly active convection and vertically upward motion near the equator, and H, F, and P refer to the Hadley, Ferrel, and polar circulatory cells respectively.

heading back toward the equator. This meridional circulatory motion between the equator and roughly $\pm 30^\circ$ latitude describes what are known as the Hadley cells, the primary mechanism for transporting energy from the tropics toward higher latitudes (see Figure 2.2).

Energy moves poleward from the tropics in various forms (including gravitational potential energy, latent heat, etc.) and in various ways (including via the mean meridional motion, e.g. the Hadley cells, and eddies). To

calculate energy transports and break them down into these various components, one begins by writing down the total energy (per unit mass),

$$\mathcal{E} = \overbrace{\underbrace{c_p T + gz}_{\text{Dry static energy}} + Lq}^{\text{Moist static energy}} + \frac{1}{2}\left(u^2 + v^2\right), \tag{2.19}$$

where the terms in order are sensible heat (i.e. internal energy), potential energy, latent heat, and kinetic energy (which is usually small and often neglected). The geophysical definitions of *dry static energy* and *moist static energy* are indicated. By integrating (2.19),[4] one can obtain an expression for the meridional energy transport. The discretized version of that expression, including sensible heat, gravitational potential energy, and latent heat (but neglecting the kinetic energy term, as is usual), will be useful in Chapter 3:

$$P_j = \frac{2\pi R}{N_\lambda g} \cos\phi_j \sum_{i,k} v_{i,k} \left(c_p T_{i,k} + g z_{i,k} + L q_{i,k}\right) \Delta p_{i,k}. \tag{2.20}$$

Here, i, j, and k index the zonal, meridional, and vertical directions respectively, and ϕ_j is the latitude with the equator defined as zero degrees. N_λ is the number of model grid cells in the zonal direction; the factor of $1/N_\lambda$ comes from taking the zonal average.

From (2.20) can be derived a wealth of information about the global poleward energy transport. As written, P_j gives the total energy transport across some latitude ϕ_j, but the three pieces (2.20) can of course be considered separately to determine the transport of internal energy, gravitational

[4]The precise steps are given in Appendix B.

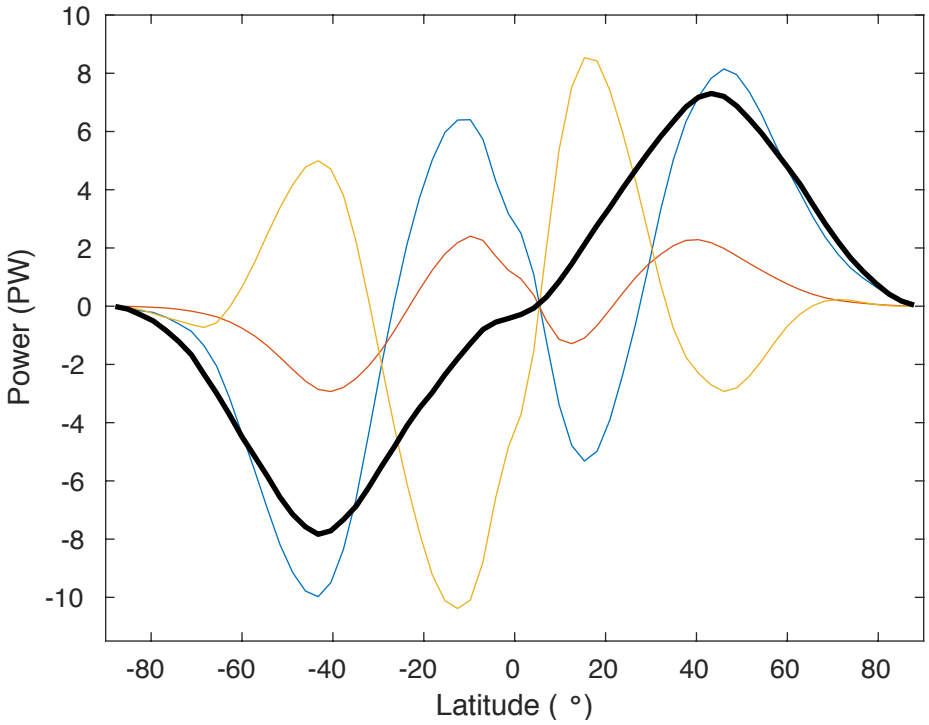

Figure 2.3: The results of a typical energy transport calculation using Eq. 2.20 and its components. The blue, red, and yellow lines indicate, respectively, total northward (i.e. negative meaning southward) energy transport of sensible heat, latent heat, and gravitational potential energy, while the thicker black line gives the sum of all three. Note that near the tropics, the plots indicate that sensible heat and latent heat are being carried toward the tropics, while export is in the form of gravitational potential energy. This is consistent with the way the Hadley cell is understood to function, with warm, moist air flowing toward the equator at low levels, and convection then carrying this air high into the troposphere, where the potential energy of the now cold, dry air can be exported toward the poles. These data come from a randomly selected experiment from the Community Atmosphere Model, version 3 (CAM3) ensemble described in Chapter 3.

potential energy, and latent heat (Figure 2.3). More interestingly, the components of (2.20) can be manipulated to extract information about the mode of energy transport, whether via the mean meridional transport or via transient or stationary eddies. For example, the meridional mean (MM), stationary eddy (SE), and transient eddy (TE) transport of sensible heat (internal energy) are given by

$$
\begin{aligned}
I_{\mathrm{MM}} &= \frac{2\pi R}{N_\lambda g} \cos\phi_j c_p \sum_{i,k} \langle v_{i,k} \rangle_\lambda \langle T_{i,k} \rangle_\lambda \Delta p_{i,k} \\
I_{\mathrm{SE}} &= \frac{2\pi R}{N_\lambda g} \cos\phi_j c_p \sum_{i,k} \left(v_{i,j} - \langle v_{i,k} \rangle_\lambda \right) \left(T_{i,j} - \langle T_{i,k} \rangle_\lambda \right) \Delta p_{i,k} \\
I_{\mathrm{TE}} &= \frac{2\pi R}{N_\lambda g} \cos\phi_j c_p \sum_{i,k} \left(v_{i,j} - \langle v_{i,k} \rangle_t \right) \left(T_{i,j} - \langle T_{i,k} \rangle_t \right) \Delta p_{i,k},
\end{aligned}
$$

where again $\langle\rangle_\lambda$ denotes the zonal mean and $\langle\rangle_t$ denotes the time average. The (meridional mean) Hadley circulation and transient eddies are very different means of transporting energy toward higher latitudes, and will be important in thinking about different modes of tropical circulation in both Section 2.5 below and in Chapter 3.

Another useful way of analyzing and also visualizing the large-scale tropical circulation, also used in Chapter 3, is via stream functions, denoted $\psi(\phi, z)$ or $\psi(\phi, p)$, which give a latitude-height or latitude-pressure profile of the zonal-mean circulation (Figure 2.4). These can be obtained from zonally averaging the conservation of mass equation (2.4) to obtain

$$
\frac{1}{R_E \cos\phi} \frac{\partial}{\partial \phi} \left(\cos\phi \langle v \rangle_\lambda \right) + \frac{\partial \langle \omega \rangle_\lambda}{\partial p} = 0, \tag{2.21}
$$

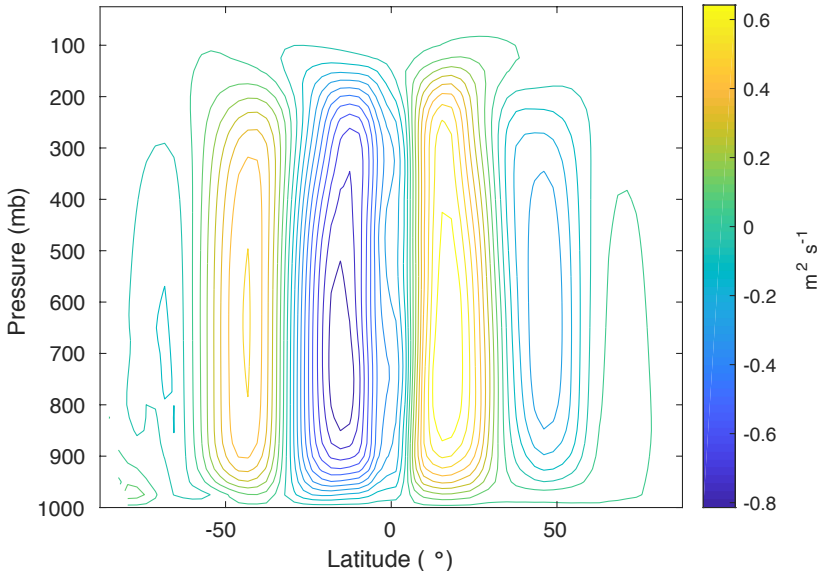

Figure 2.4: The results of a typical stream function transport calculation using Eq. 2.22. Positive values indicate clockwise motion. Note that these are annual-mean stream functions; in boreal summer, the counterclockwise cell dominates the tropics; in boreal winter, the clockwise cell dominates. [These data come from a randomly selected experiment from the Community Atmosphere Model, version 3 (CAM3) ensemble described in Chapter 3.]

which can be represented by the two equations

$$\langle v \rangle_\lambda = \frac{g}{2\pi R_E \cos\phi} \frac{\partial \psi}{\partial p} \quad \text{and} \quad \langle \omega \rangle_\lambda = -\frac{g}{2\pi R_E^2 \cos\phi} \frac{\partial \psi}{\partial \phi}. \tag{2.22}$$

2.2 Rainfall in climate models

Out of concern that greenhouse gas (GHG) forcing could cause significant changes in global climate, scientists have been working to find ways of anticipating these long-term changes, but with such a complex system, there are limits to what can be done analytically. Interesting results have been obtained via analytical methods (e.g., see [38]), but for the most part we must

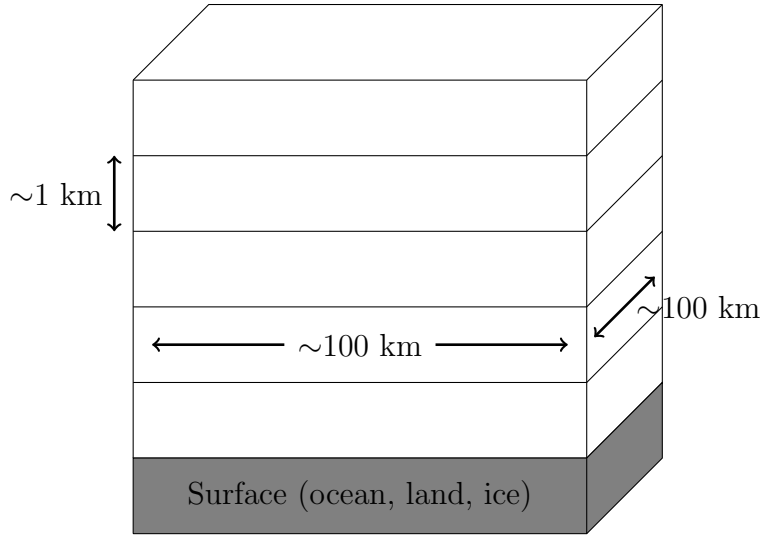

Figure 2.5: A simple depiction of vertical discretization in an atmospheric climate model, giving a sense of the dimensions of typical grid cells in this study. Note that only five vertical levels above the surface are shown for simplicity; a typical atmospheric model will have several tens of cells in the vertical direction.

use numerical models to investigate long-term climate change. A global climate model takes a spherical shell over the Earth's surface, included in which are the oceans, the land surface, the ice cover, and the atmosphere from the surface to the top of the troposphere or higher, and breaks that shell into a discrete set of grid cells. Various quantities associated with those grid cells are then calculated (pressure, temperature, humidity, etc.).

An important model feature is its resolution: the larger the number of grid cells, the smaller each cell will be, and the finer the resolution. With current computing technology, a typical atmospheric model will have grid cells with a horizontal resolution of about 100 km on a side—fairly large cells (Figure 2.5). Hence it is an ongoing and highly significant problem to account for

	Large-scale	Convective
Also called	nonconvective, stratiform	cumulus
Size	grid-scale (but see caption)	sub-grid-scale
Cause	frontal lifting/ambient cooling	buoyant lifting
Height	typically low	upper troposphere
Modeled by	microphysics param.	convective param.

Table 2.2: Typical characteristics of the two main types of precipitation in climate models, large-scale and convective. While large-scale rain is commonly associated with the grid scale, technically, the microphysics parameterization is capable of treating partial saturation of the grid cell, hence sub-grid effects can be present in the microphysics routine as well.

physical phenomena taking place on smaller scales. When physical processes take place on scales smaller than what the model resolves—and many crucial processes, including convection, condensation, and cloud formation, do—modelers must devise ways of adjusting the grid cell quantities to account for the expected effects of these smaller-scale processes. In the numerical climate modeling community, this accounting for the effects of small-scale processes on the larger-scale physics is known as *parameterization*, and "parameterization schemes" are a major source of uncertainty within models.

Rainfall processes involve many spatial scales, most of which are smaller than typical model resolution: convective plumes are on the order of kilometers across, while condensation and cloud formation take place on microscopic scales. Correspondingly, atmospheric models generate two main types of rainfall using two main parameterization schemes (see Table 2.2). The first type, "convective" or "cumulus" rainfall, is generated by a convective or cumulus parameterization scheme, while the second type, "large-scale", "grid-scale", or "stratiform" rain, is generated by a cloud microphysics parameterization [28].

Some models, including those used in this thesis, further partition convective rainfall between separate deep and shallow convection schemes. In this thesis, the terms "convective" and "large-scale" rain will be used for the two main types of model rainfall. Typically, convective rain is most active in the tropics, while large-scale rain is associated with midlatitudes, where fronts lift large air masses resulting in condensation.

While convection involves upward motion, a convective parameterization scheme may not. Because convection happens on a faster time scale than the mean vertical motion, a convective parameterization scheme—including those employed in the models discussed in this thesis [129]—merely "mixes" the column, removing heat and moisture from the lower part of the column and adding heat and moisture above, depending on how unstable the column is. This is important to note, because, as described in the next section, a single-column model will take account of convection but need not have any resolved vertical advection.

2.3 Single-column models

In addition to global atmospheric models, often called general circulation models (GCMs), the other type of model considered in this thesis is a "single-column model" (SCM). A SCM could be constructed by itself or could be extracted from a GCM; in either case, it is a one-dimensional vertical model extending from the surface (which may be ocean, ice, or land) to a desired height (e.g., the top of the troposphere).

2.3.1 Basic SCM equations

There are important ways in which SCMs are different from global models, the most important being the lack of mass, energy, and momentum conservation and large-scale dynamics. SCMs are based on conservation equations for energy and water vapor mass (Eqs. 2.2 and 2.5), but with both equations allowing for sources and sinks:

$$\frac{\partial T}{\partial t} + \omega \frac{T}{\theta} \frac{\partial \theta}{\partial p} = \sum \{\text{parameterized } T \text{ forcings}\} \tag{2.23}$$

$$\frac{\partial q}{\partial t} + \omega \frac{\partial q}{\partial p} = \sum \{\text{parameterized } q \text{ forcings}\}, \tag{2.24}$$

where in (2.23) I have combined the adiabatic and vertical advection terms using the potential temperature. Horizontal advection terms are absent due to the one-dimensional nature of the model—there are ways of mimicking horizontal advection in a SCM setting, but they are not utilized in this thesis. Furthermore, without coupling to the rest of the atmosphere or the other components of the global climate system, it is not possible to solve separately for ω. Hence the vertical motion within the column must either be prescribed (if one is interested in modeling a particular scenario or location) or set to zero (if one is interested in a global average). In the latter case, the vertical advection terms are absent as well:

$$\frac{\partial T}{\partial t} = \sum \{\text{parameterized } T \text{ forcings}\}$$

$$\frac{\partial q}{\partial t} = \sum \{\text{parameterized } q \text{ forcings}\}.$$

In this case, the steady state is just a balance between diabatic heating terms. The dominant balance is usually between radiative cooling and convective

heating, hence SCMs are sometimes called radiative-convective equilibrium (RCE) models.

2.3.2 The weak temperature gradient approximation

As noted, SCMs are generally unable to account for large-scale dynamics. However, following early work by Charney [16] and Bretherton and Smolarkiewicz [8] among others, Sobel and Bretherton [99] developed a scheme, called the weak temperature gradient (WTG) approximation, that attempts to "parameterize" the effects of large-scale motion. This is very useful because it restores the coupling between convection and large-scale dynamics in the less computationally expensive SCM setting. In the WTG approximation, the single-column vertical motion, rather than being set to a fixed profile or set to zero, is calculated to keep free-tropospheric temperatures equal (or roughly equal) to a specified temperature profile, usually representing RCE. Below the free troposphere within the atmospheric boundary layer, temperatures are unconstrained and the vertical velocity is usually reduced linearly from its value at the base of the free troposphere to zero at the ground.

To see the justification for the WTG approximation, consider Newton's second law (2.1). Assuming frictional effects are small in the free troposphere (friction is largest near the surface) and restricting ourselves to the horizontal dimensions where the dominant effect is geostrophic balance (in which the Coriolis force balances the pressure gradient force), one can write (2.1) simply

as

$$\nabla p = -\rho f \vec{k} \times v,$$

where $\vec{k}$ is the vertical unit vector and $f \equiv 2\,\Omega \sin\phi$ is known as the Coriolis parameter. In the tropics where ϕ is small, $f \approx 0$ and horizontal pressure gradients are small. The basic physical explanation for this is that atmospheric gravity waves quickly flatten out any pressure and temperature anomalies in the deep tropics [8]. Under the standard WTG framework, it is assumed that horizontal temperature gradients are also small [99], an assumption that holds up well empirically (Figure 2.6), although a "weak pressure gradient approximation" has been proposed as an alternative framework [88].

Now considering Eq. (2.23) again, one can see that if pressure and temperature anomalies are quickly eliminated by gravity waves and hence temperatures are stable in time (i.e. $\partial T/\partial t \approx 0$), and furthermore if horizontal advection is neglected within the single-column framework, the dominant balance in the deep tropics is between vertical heat transport and diabatic heating. Generally speaking, diabatic heating will lead to upward average motion, while for example radiative cooling will be associated with large-scale descent.

There are different ways to implement the WTG approximation in practice, two of which I now briefly describe.[5]

[5]For an "intercomparison" study exploring different methods and models for coupling convection to large-scale dynamics, see [29].

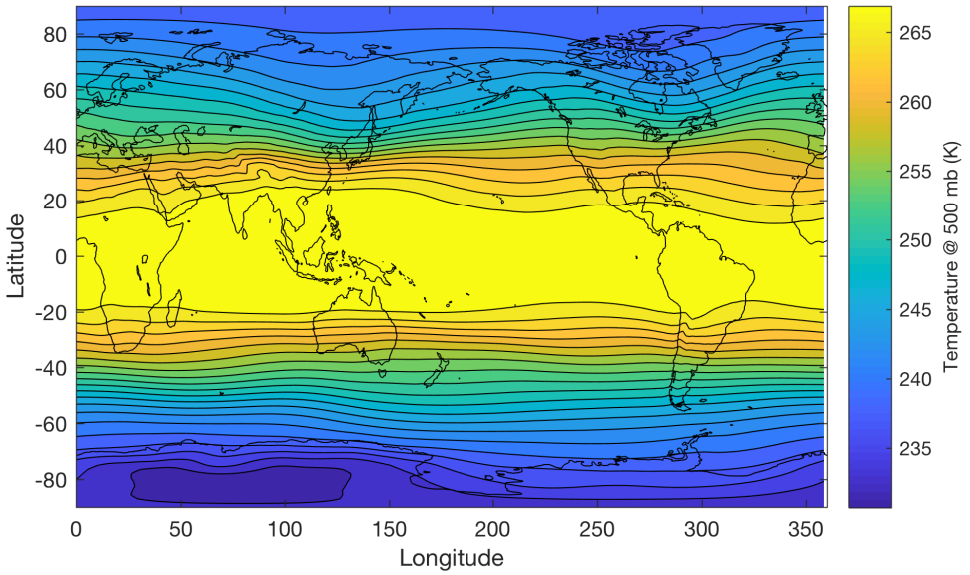

Figure 2.6: Observed temperatures at 500 mb. Tropical temperatures in the free troposphere show a high degree of horizontal homogeneity. This figure was created from ERA-Interim reanalysis data [30], which is observational data that has been "reanalyzed" by computer to create a complete dataset.

2.3.2.1 Fixed-temperature implementation

One approach is to assume that the tropical free-tropospheric temperatures do not evolve in time at all, so that

$$\frac{dT}{dt} = \cancelto{0}{\frac{\partial T}{\partial t}} + w\frac{\partial T}{\partial z}.$$

The grid-scale vertical velocity, rather than being prescribed or set to zero, is then calculated from (2.2). Starting with

$$w\frac{\partial T}{\partial z} = \frac{dz}{dt}\frac{\partial T}{\partial z} = \frac{dp}{dt}\frac{\partial T}{\partial p} = \frac{1}{c_p}\left(\frac{1}{\rho}\frac{dp}{dt} + Q\right),$$

one can obtain

$$\omega\frac{\partial T}{\partial p} = \omega\frac{RT}{c_p p} + \frac{Q}{c_p}$$
$$\implies \quad \omega = -\frac{Q}{c_p}\left(\frac{RT}{c_p p} - \frac{\partial T}{\partial p}\right)^{-1}, \tag{2.25}$$

where the pressure velocity (2.8) is used. Eq. (2.25) indicates that diabatic heating ($Q > 0$) gives an upward vertical velocity while cooling gives a downward velocity, as expected based on the theory described above. The denominator is, practically speaking, always positive: one can see this by noting that the two terms in the denominator would be equal if the environmental temperature sounding followed the dry adiabatic lapse rate (i.e., if $\partial T/\partial z = -g/c_p$),

$$\frac{\partial T}{\partial p} = \frac{\partial z}{\partial p}\frac{\partial T}{\partial z} = \left(-\frac{1}{\rho g}\right)\left(-\frac{g}{c_p}\right) = \frac{RT}{c_p p},$$

but a realistic profile will cool more slowly than Γ_d.

2.3.2.2 "Newtonian relaxation" implementation

The other way of implementing the WTG approximation is via "Newtonian relaxation", meaning instead of free-tropospheric temperatures being held fixed, they are continuously nudged back toward a target profile on some time scale τ. This is how the WTG approximation is implemented in the Weather Research and Forecasting (WRF) model [113] used in Chapter 4 of this thesis. In this case,

$$\omega\frac{\partial \theta}{\partial p} = \frac{\theta - \theta_{\mathrm{RCE}}}{\tau},$$

where θ_{RCE} is a vertical radiative-convective equilibrium potential temperature profile. Here, it is not diabatic heating (cooling) that produces an upward

(downward) velocity, but simply a potential temperature higher (lower) than that of the radiative-convective equilibrium profile at a given height.

Both WTG approximation schemes re-introduce the vertical advection term $\omega\,\partial q/\partial p$ into the moisture advection equation, as in (2.24). This additional term acts as a source or sink for moisture within the column.

2.4 Abrupt climate change

As indicated in the introduction, it has long been understood that the climate system has gone through dramatic changes on geological time scales, the most salient of which are Pleistocene transitions between stadial (ice age) and interstadial (thawed) phases. It is now clear that the climate system is capable of changing significantly on time scales shorter than a human lifespan. This gets to the heart of most definitions of abrupt climate change, usually defined as a threshold-crossing in some component of the climate system, leading to a spatially large-scale change in climate on a time scale short enough to disrupt biological (and particularly human) systems. The new climate regime is expected to persist in time for several decades or longer. For a review of various definitions of abrupt climate change, see [26].

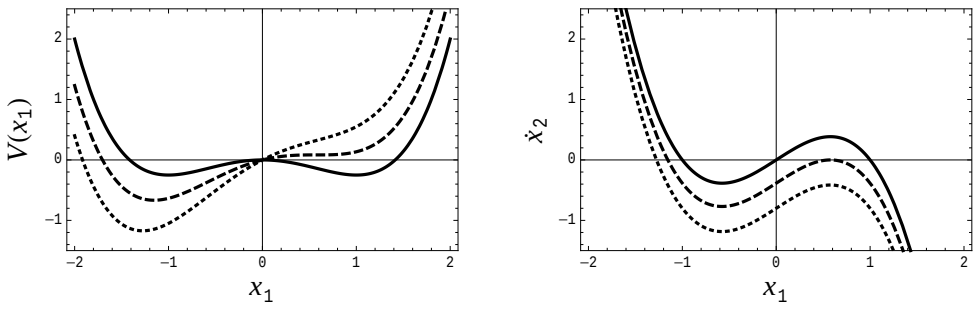

Figure 2.7: On the left, the potential (2.26) is plotted for three different values of β; on the right, (2.27) is plotted for the same three β values. For $\beta = 0$ (solid), there are three equilibria (points where $\dot{x}_2 = 0$), two stable and one unstable. For a critical value of $\beta_c = -\sqrt{12}/9$ (dashed), there are two solutions, one stable and one unstable. For $\beta < \beta_c$ (dotted), only one stable solution remains.

2.4.1 A simple example

Nonlinear systems can exhibit abrupt transitions. As a simple example, consider a physical system described by the potential

$$V(x_1) = -\beta x_1 - \frac{1}{2}x_1^2 + \frac{1}{4}x_1^4, \tag{2.26}$$

where x_1 describes the position of a mass m and β is some parameter (other parameters would be required to make the units work; I ignore this here). Using $F = -dV/dx_1$, this yields a second-order nonlinear system described by

$$\begin{aligned} \dot{x}_1(t) &= x_2 \\ \dot{x}_2(t) &= \beta + x_1 - x_1^3, \end{aligned} \tag{2.27}$$

where I assume the mass $m = 1$ and introduce the variable x_2 to put the system into the customary form $\dot{x}_i = f_i(x_1, x_2, \ldots, x_n)$, $i = 1, \ldots, n$. Equilibria are found by setting $\dot{x}_i = 0$ and solving for x_i. Clearly, the second equation is

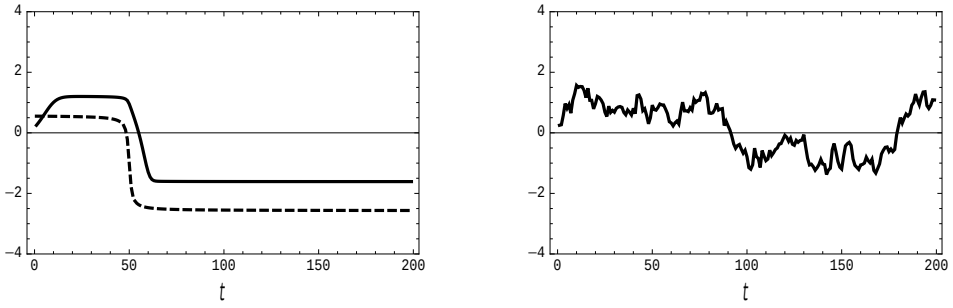

Figure 2.8: Two types of abrupt transitions for our simple example. On the left, the position of the mass (solid) drifts toward the positive equilibrium and remains there until the value of β (dashed) is reduced across a critical value around time $t = 50$, at which point the mass rolls into the negative equilibrium. On the right, β is held constant at zero, while the mass is nudged with a stochastic forcing. The mass tends to stay close to one of the two stable equilibria, but can transition between them if the stochastic forcing is large enough, and does so around $t = 90$ and $t = 180$.

more interesting; I will ignore the first. There are two ways to see an abrupt transition in this system, which can be described with reference to Figure 2.7. One way is to imagine a mass resting in the right well of the potential when $\beta = 0$, and then continuously change the value of β. As β is reduced below a critical value, there is no longer a well on the right and the mass is forced into the only remaining well on the left hand side. It is also possible to hold β constant and stochastically force the system into the other stable state. One can imagine this as a series of nudges on the resting mass, and a strong enough nudge will cause the mass to cross over into the left well. Examples of the actual transitions are shown in Figure 2.8.

2.4.2 Abrupt climate change in the ocean and atmosphere

These concepts carry over into a discussion of the climate system, which exhibits numerous nonlinearities; however, climate "equilibria" are much more complicated than the solutions of our toy model. For one thing, no part of the climate system is ever at rest. The atmosphere and ocean are ceaselessly circulating; the ice caps periodically grow and shrink; even the lithosphere is in motion over long enough time scales. There are also numerous components of the climate system with potential tipping points, such as the AMOC, the arctic permafrost (which could melt, releasing GHGs into the atmosphere causing further warming), the Amazon rainforest (which could be deforested, thus eliminating a carbon sink while simultaneously releasing additional carbon into the atmosphere), the El Niño/Southern Oscillation (whose amplitude or frequency could change), and many others. For a nice summary of a number of climate tipping points, see [55].

Solid evidence exists for abrupt climate change in the distant past. One example, known as a Heinrich event (labeled with an 'H' in Figure 1.1), is worth discussing in some detail since it will be relevant for the discussion in the next section. In a Heinrich event, it is believed that pieces of North Atlantic glaciers would break away and icebergs would float into the Atlantic Ocean, where they would melt. Evidence of Heinrich events is found at the bottom of the ocean, where sediment layers abruptly transition, with Heinrich events being associated with "ice-rafted debris" only found in glacial ice, indicating that large chunks of ice were melting in the mid-North Atlantic [27]. More

significantly for our purposes, there would be an influx of cold freshwater into the North Atlantic Ocean. This leads to a local decrease in ocean salinity, and therefore a decrease in the density of the water, possibly interrupting the downwelling of water at high latitudes. This leads us into a discussion of the most studied mechanism advanced to explain abrupt climate change: a shutdown in the AMOC, which forms part of the thermohaline circulation, the global ocean "conveyor belt" that moves heat and salt around the ocean. A slowdown or shutdown of the AMOC, as a result of a Heinrich event for example, could cause changes in global climate by diminishing the efficiency of heat transport from the tropics toward the north pole.

The relationship between abrupt climate change and multiple equilibria in the ocean's overturning circulation traces back to 1984, when Hans Oeschger proposed that oscillations between the different equilibrium oceanic states were the cause of the rapid climatic shifts understood to have occurred during the last glacial period [73]. Evidence for such abrupt transitions is based on analysis of ice cores from Greenland and Antarctica, and multiple equilibria in ocean circulation have been observed in simplified models [103]. Yet there are questions about whether the AMOC-shutdown hypothesis is sufficient. Carl Wunsch in particular has raised objections to the AMOC mechanism based on the empirical complexities of the ocean circulation [124]. And given mixed evidence for precursor signals (i.e. critical slowdown or increased variance) in the paleoclimate record [54] along with the rapidity of the abrupt transitions, we can ask whether there may be an atmospheric trigger for abrupt climate

change instead of or in addition to an ocean trigger. In particular, considering the importance of atmospheric circulation in transporting energy throughout the climate system—the atmosphere transports five petawatts (PW) of energy poleward, while the oceans transport 1 PW [96]—it is conceivable that the tropics could participate in triggering abrupt transitions via changes in those circulation patterns. (Forcings for abrupt climate change originating from outside the climate system, for example periodic changes in solar activity or in insolation due to Earth's orbital motion, are still being considered as well, but no consensus has emerged. For some interesting studies relevant to solar forcing, see [80] and [49].)

2.5 CCSM3 Experiments

The projects discussed in Chapters 3 and 4 below were motivated by a set of modeling experiments carried out by Jackson et al. [44] using the Community Climate System Model, version 3 (CCSM3), developed by the National Center for Atmospheric Research (NCAR). These experiments simulated a large influx of cold freshwater into the North Atlantic, qualitatively not unlike a Heinrich event, although including forcings of larger amplitude. The CCSM3 forcings vary from 0.3 to 1.5 sverdrups (Sv), where 1 Sv = 10^6 m^3/s, while, for example, the freshwater influx for Heinrich Event 4 may have been about 0.3 Sv [85]. According to Paleoclimate Modeling Intercomparison Project (PMIP) studies, the typical response to this kind of forcing is a cooling of the North Atlantic and a reduction in the efficiency of the AMOC. With that ocean cir-

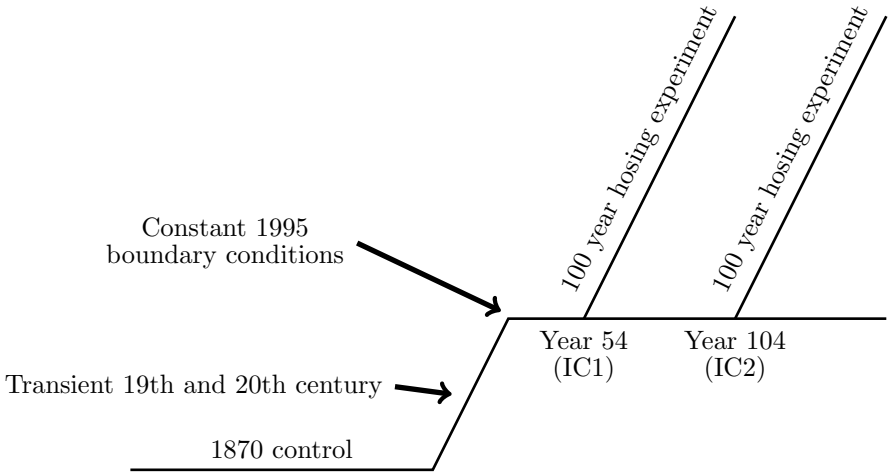

Figure 2.9: The experimental setup of the CCSM3 hosing experiments, showing the origin of the initial conditions IC1 and IC2. Adapted from Charles Jackson's unpublished notes.

culation not transporting energy northward at its typical rate, the tropical ocean heats up and the band of warm temperatures and convection known as the intertropical convergence zone (ITCZ) is pushed southward [74].

Temperatures are generally warmest in the tropics near the ITCZ, and this band of warm temperatures is a highly active region for convection; the rising air here forms the upward branches of the Hadley cells. After a freshwater forcing in the North Atlantic and subsequent tropical heating, the now warmer tropical air will give a more efficient Hadley circulation; that is, since the ocean isn't transporting as much heat northward, the atmospheric circulation compensates to move more of that heat poleward.[6]

This type of response was seen in one set of CCSM3 experiments, those

[6]This type of energy-transport handoff between atmosphere and ocean is sometimes called *Bjerknes compensation* [96].

starting from a certain set of initial conditions I will call IC1. But, starting from another set of initial conditions I will call IC2, the model produced a very different response. Figure 2.9 illustrates the experimental setup and shows where these two initial states originate. The experiment started from a pre-industrial environment, then applied the known forcings during the industrial era up to the year 1995, complete with the anthropogenic GHG emissions up to that point. Then, GHG levels were held constant and the experiment was allowed to equilibrate and run for several hundred years. The initial states IC1 and IC2 for the hosing experiments were taken from this equilibrium distribution fifty years apart. The subsequent hosing experiments were run a number of times with varying rates of freshwater influx.

Figure 2.10 shows the two precipitation response patterns observed in the CCSM3 hosing experiments; this is total rainfall averaged over the last twenty years of the 100-year forcing simulation minus the total rainfall in the equilibrated control simulation running after 1995. These patterns are in response to a freshwater influx of 0.4 Sv. (Note that in Figure 2.10, red indicates more precipitation, blue less.) The upper panel of Figure 2.10, which was run from IC1, shows the rainfall response of the more typical scenario described above. It is evident in the tropics that a zonal band of strong precipitation has moved toward the south, consistent with a shift of the ITCZ. In the lower panel showing the rainfall response from IC2, however, there was a very different outcome, with a number of noteworthy features. Most dramatically, the very different precipitation patterns evident in the lower panel of Figure 2.10,

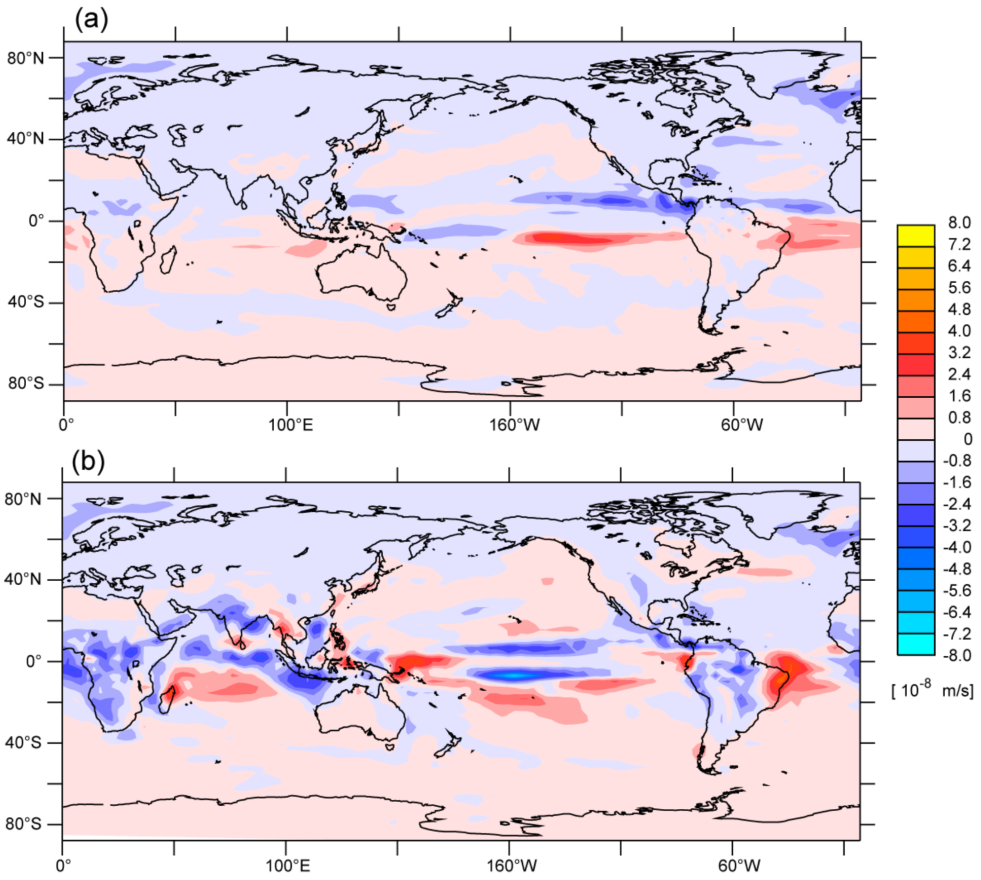

Figure 2.10: Rainfall response for 0.4 Sv forcing into the North Atlantic in the CCSM3 models starting from two statistically identical sets of initial conditions. (a) shows the "typical" response pattern starting from IC1, with a southward shift of the Intertropical Convergence Zone, while (b) shows a novel response starting from IC2, including extreme drying throughout much of the tropics, evident in this figure, along with a weakening of the zonal mean tropical circulation and increase in the fraction of large-scale rainfall.

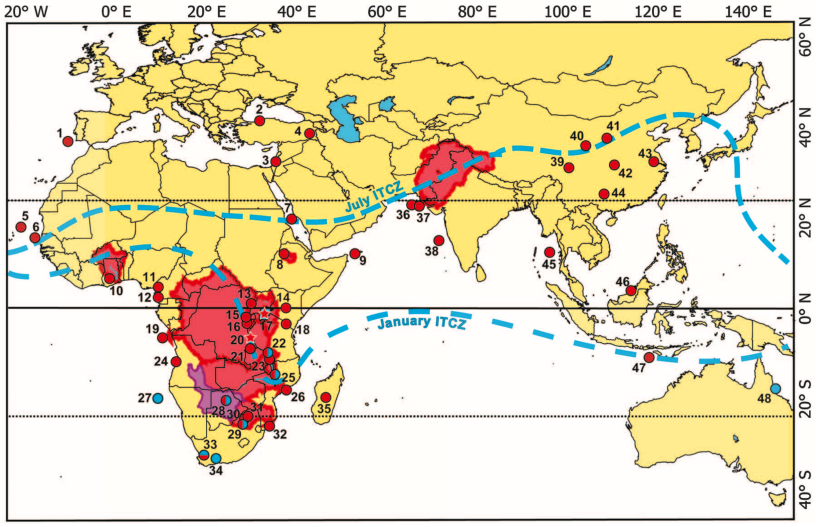

Figure 2.11: Climate proxies indicate a "megadrought" in association with Heinrich Event 1, 16-17 thousand years ago. Red dots indicate test sites where evidence of drying is found, although the total area likely to have been affected by this drying is not indicated (some is shaded in red). Blue dots indicate moistening. Figure from [101].

and described in more detail presently, did not emerge gradually in the IC2 simulation but set in abruptly within one month, with the year of onset depending on the amplitude of the forcing (with larger amplitude forcings leading to earlier transitions). The novel state to which the model abruptly transitions shows, first, a dramatic drying over large regions, including Africa, south Asia, and South America, and, as Figure 2.11 shows, this feature in particular is reminiscent of what may have occurred during Heinrich Event 1 [101]. Second, the novel state shows a different rainfall distribution: in the upper panel, east-west bands of precipitation show a fair amount of zonal symmetry, but in the lower panel there is much more asymmetry in the zonal rainfall distribution. This is likely due to the fact that the Hadley circulation, whose meridional

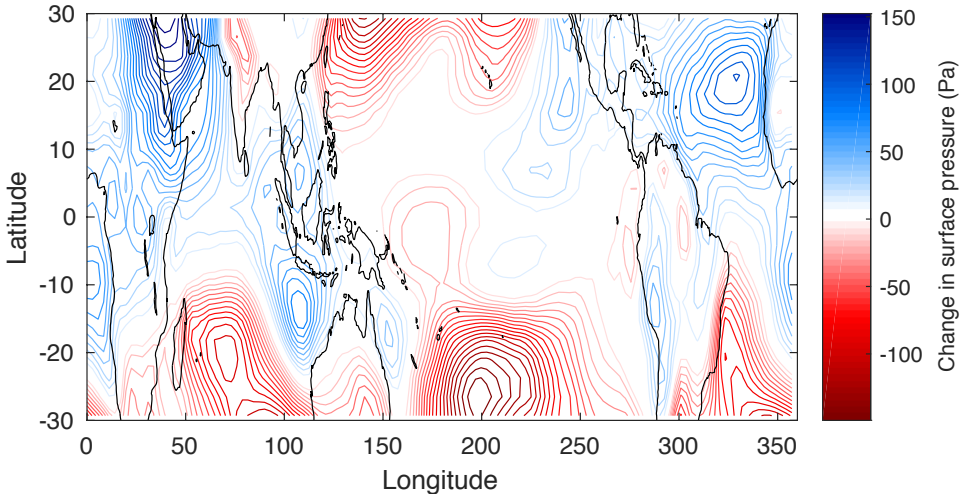

Figure 2.12: The novel CCSM3 experiment response includes a drop in pressure in the west Pacific "warm pool" region, where the abrupt transition is initiated. The contour lines show the surface pressure averaged over the last 20 years of the 100-year hosing experiment, minus the surface pressure averaged over the first 20 years of that experiment. The area of interest is just east of the Maritime Continent, where an area of low pressure can be seen.

orientation is a major source of zonal symmetry in large-scale precipitation patterns, *weakened* in the IC2 case rather than strengthening as in the IC1 response. With a weakened Hadley cell, other effects become more prominent, in particular monsoonal circulations which are spatially more complex and less zonally symmetric. The heat that collects in the tropics and caused a stronger Hadley circulation in the IC1 case is dissipated in the IC2 case by transient eddies, a mode of energy transport more often seen at higher latitudes.

Third and finally, there is an outcome not obvious from Figure 2.10—this effect is related to there being two different types of precipitation generated by the model (convective and large-scale) as described in Section 2.2. In the IC2 case, large-scale precipitation increases and convective precipitation

decreases across the tropics as the transition occurs; the fraction of large-scale precipitation abruptly increases from roughly 7% to 14%. Given these very different features resulting from the same forcing applied to different initial states, one can ask whether we are seeing a new regime with different circulatory and rainfall characteristics, where the distribution and type of rainfall, along with the Hadley cell response, are all very different.

Output from the IC2 experiments suggests that the abrupt transition is initiated in the western Pacific near the Maritime Continent and may be caused by low-level convergence there (Figure 2.12). In other words, the output suggests that a rapid energy increase near the surface may cause a reorganization in the GCM physics which can then be dispersed across the tropics.

2.6 Literature review

Key questions raised by the CCSM3 results described above include (1) the large-scale effects of model partitioning between convective and large-scale rainfall, and (2) the effects of sea surface temperature (SST) and low-level convergence on this partitioning. The following two chapters address these questions in turn. Before moving on, however, it is useful to review results from several papers that provided insights and connections helpful in designing the experiments and analyses described in Chapters 3 and 4.

Valuable insight into the interaction between convective and large-scale parameterizations is provided by Frierson [33], who analyzed the dependence of tropical rainfall and circulation patterns on the convection scheme. Using

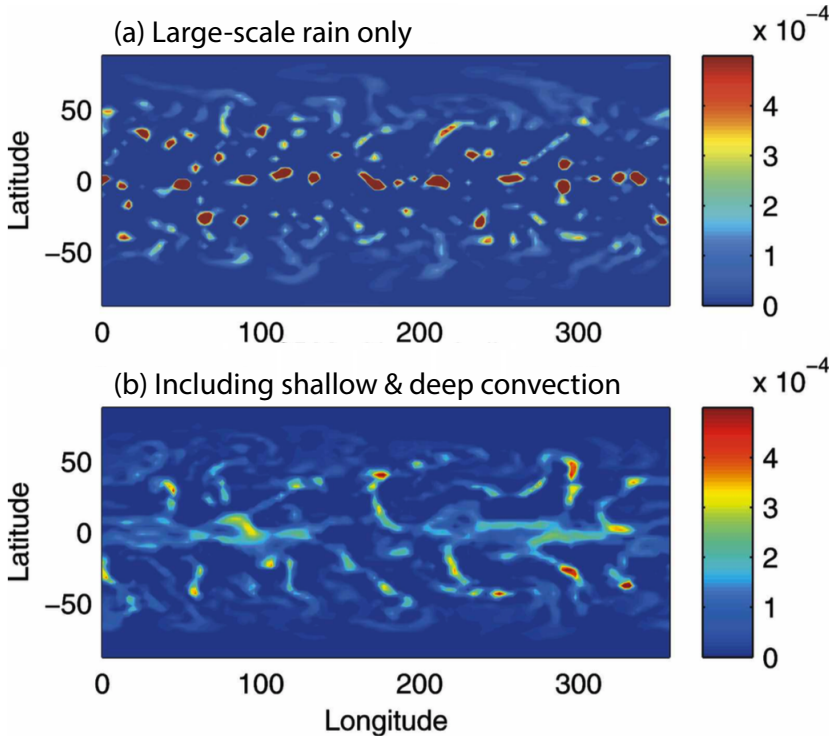

Figure 2.13: Results from Frierson's aquaplanet experiments [33]. (a) shows the precipitation when large-scale rain only was allowed by the model configuration; (b) shows the precipitation when both deep and shallow convective parameterizations were active as well. Image adapted from [33].

an aquaplanet model (a global model without any land surface), Frierson [33] used several different parameterization configurations, including large-scale rainfall only and large-scale rain in addition to deep and/or shallow convection schemes. When only large-scale rain was permitted, there was reduced zonal symmetry in the tropical rainfall distribution (which appeared as a collection of localized storms) along with a stronger Hadley circulation and an increase in small-scale eddies exporting latent heat from the tropics. When convective parameterization schemes were active as well (whether deep con-

vection only or in addition to shallow convection), the Hadley cell turned more slowly and zonal bands of rainfall appeared (Figure 2.13). While an aquaplanet configuration will differ in important ways from the more realistic GCM experiments described in Chapter 3, these effects have clear and intriguing similarities with the CCSM3 experiments described above. Frierson's [33] findings furthermore suggest a hypothesis: a larger fraction of large-scale rain reduces the efficiency of poleward energy transport by the mean meridional circulation, because fewer convective plumes means less energy is injected deep into the free troposphere. A corollary hypothesis is that model configurations with larger fractions of large-scale rain will be associated with stronger zonally asymmetric circulations, hence greater monsoonal rainfall and greater energy export from the tropics via transient eddies.

Held et al. [40] studied GCM physics in another type of idealized setting—a large, ocean-surface domain with doubly-periodic lateral boundary conditions lacking rotation or spherical geometry. This limited-domain model showed similar outcomes at low and high resolutions: higher SSTs resulted in larger fractions of large-scale rainfall and very intense regions of precipitation they called "gridpoint storms" (Figure 2.14). Among other things, Held et al. [40] considered the dependence of rainfall type on SST, finding larger fractions of large-scale precipitation for higher SSTs, consistent with the CCSM3 experiments described above.

Findings reported by Sobel et al. [98] are interesting in the context of the extreme tropical drying observed in the CCSM3 experiments. Using a

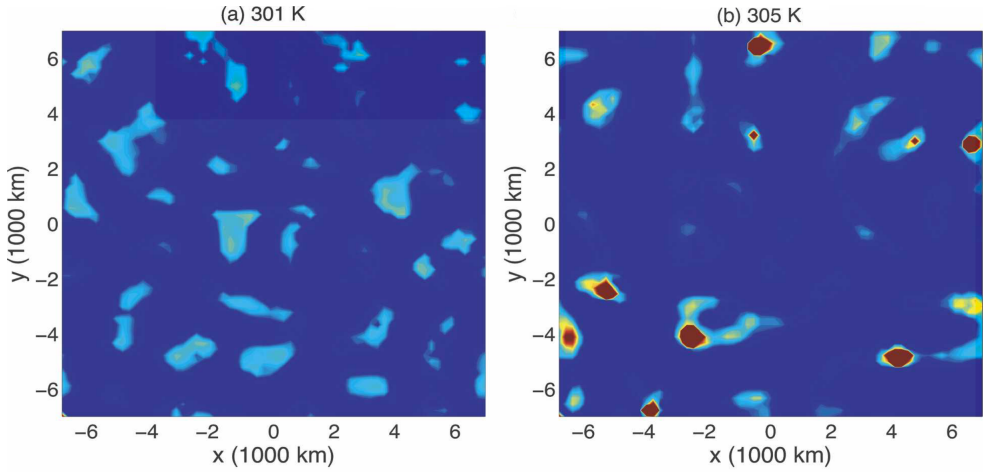

Figure 2.14: Results from Held et al. [40]. For a large, doubly-periodic domain run at GCM (i.e., low) resolution, different surface temperatures (a) 301 K and (b) 305 K give different precipitation effects. In particular, although not obvious from the figures, the darker red spots in the high-temperature experiment (which Held et al. call "gridpoint storms") are regions of heavy large-scale (as opposed to convective) rainfall. Figure adapted from [40].

SCM with the WTG approximation, Sobel and collaborators found multiple equilibria (rainy and dry states) for the same column boundary conditions. Starting with a dry column, they found they could inhibit precipitation—even for SSTs consistent with large rainfall rates—as long as the column was moistened at a small enough rate (Figure 2.15). This is interesting in the context of the CCSM3 experiments, because there the tropics did show drying despite tropical SSTs increasing over the course of the hosing experiment. Sessions et al. [95] found the same rainy and dry equilibria using the WTG approximation in a high-resolution regional model made up of interacting columns.

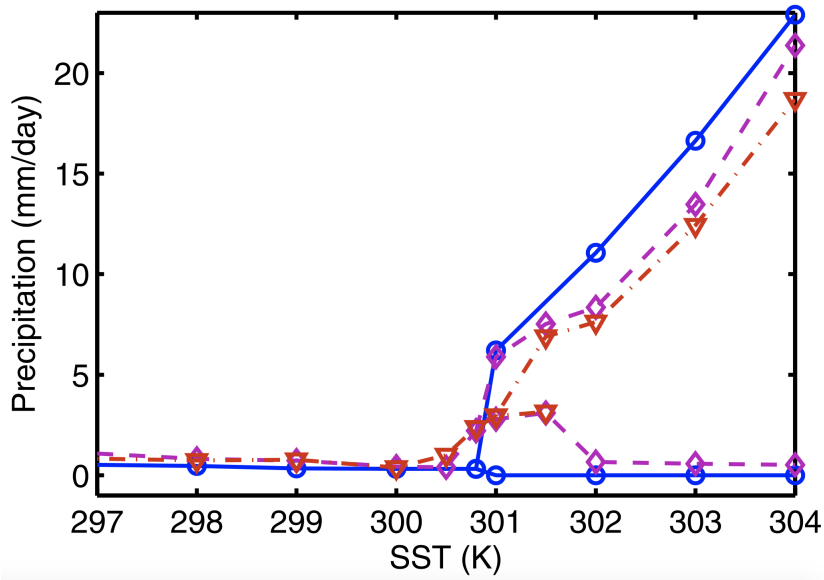

Figure 2.15: Precipitation rates versus sea surface temperature for a number of SCM experiments from Sobel et al. [98]. The different colored lines show rainy and dry equilibria for no horizontal moisture advection (blue), horizontal moisture advection with a 6-day time scale (magenta), and horizontal moisture advection with a 3-day time scale (red). The upper (rainy) and lower (dry) curves on the right side of the figure correspond to experiments initialized with moist and dry profiles respectively. These results show that for sufficiently high surface temperature and sufficiently long moisture advection time scale, either rainy or dry states can be achieved for the same final-state boundary conditions. Figure from [98].

Chapter 3

The Effect of Tropical Non-Convective Condensation on Uncertainty in Modeled Projections of Rainfall[1]

3.1 Introduction

There is more uncertainty in model projections of rainfall than surface air temperature under global warming scenarios, with models disagreeing not only on the local magnitude of the rainfall response but also its sign [25, 89, 14, 48, 53, 123, 78], the tropics being the region of highest uncertainty [18]. Given this uncertainty and the expectation that global warming will increase water shortage risks and the number of droughts and heavy precipitation events [43], greater understanding of model variation in rainfall response characteristics is essential in predicting and adapting to climate change.

While a great deal of effort has been spent to better understand and improve modeled rainfall, a critical and underexplored aspect of rainfall in climate models arises from the sometimes arbitrary partitioning of rainfall generation between two or more subroutines. Parameter settings and details

[1] A different version of this chapter has been published in *Journal of Climate* with coauthors Charles S. Jackson and Benjamin M. Wagman [102]. My contribution to this paper included performing all of the data analysis, helping to develop the conceptual models for the two CAM ensembles' behavior, and writing the paper itself including creating all figures.

of the parameterization schemes can have important consequences for the partitioning of total rainfall, which can vary a great deal. As described below, even in the tropics, different model configurations can yield a large-scale rainfall fraction ranging from a few percent to well over half. Throughout this chapter I designate this tropical large-scale rainfall fraction as f_{LS}, defined between 30S and 30N as

$$f_{\mathrm{LS}} \equiv \frac{\sum_{\mathrm{tropics}} P_{\mathrm{LS}}}{\sum_{\mathrm{tropics}} P_{\mathrm{LS}} + P_{\mathrm{C}}}, \tag{3.1}$$

where P_{LS} and P_{C} are the large-scale and convective rainfall rates respectively; I focus on the tropics because that is where the fraction of large-scale rain will typically show the most variation (not shown). I will demonstrate that, first, as a consequence of the tight coupling between tropical latent heating and circulation, f_{LS} is correlated with various features of model rainfall, including the rainfall response to CO_2 forcing. Second, I will show that the way in which the responses and spatial distributions change with f_{LS} depends on the model—even within two versions of the same model, changing f_{LS} can impact circulation and rainfall patterns in nearly opposite ways.

This documentation of the impact of f_{LS} within control and global warming simulations adds to the literature regarding the response of the hydrological cycle to global warming and may help to further clarify uncertainties in model responses. How circulation and precipitation respond to GHG forcing has been the subject of numerous studies, which have led to some important observations and hypotheses. The "rich-get-richer" (or "wet-get-wetter") hypothesis [7, 69, 21, 39] links changes in precipitation to present-day rainfall

distributions, with rainfall growing more intense deep within convective zones (hence "rich-get-richer") and less intense at the margins of such zones. Neelin and collaborators have posited an "upped-ante" mechanism for these rainfall changes at the margins, wherein a warmer troposphere requires more moisture in the planetary boundary layer to maintain positive CAPE, while low-level inflow of dry air into the adjacent regions leads to less rainfall there. These effects have been considered with respect to the zonal mean [39], but the rich-get-richer mechanism struggles to fully account for modeled *local* rainfall changes in the tropics. Studies have shown that the mechanism may be problematic over land [12, 50], and in the Coupled Model Intercomparison Project phase 5 (CMIP5) ensemble, the spatial correlation between precipitation patterns for climatological rain and the RCP8.5 response[2] was only 0.2 for the ensemble mean [14]. Chadwick et al. [14] draw on [39] and [61] in arguing that Neelin's primarily thermodynamic mechanism is countered by the dynamical effect of a weaker tropical circulation leading to a reduced convective mass flux. Held and Soden [39] argued from Clausius-Clapeyron scaling that the hydrological cycle will respond in several robust ways to global warming, beginning with a roughly 7% increase in column-integrated water vapor for each degree increase in global mean surface temperature. However, since the global-mean precipitation increases at a slower rate of around 2% K^{-1}, there must be a decrease in convective mass flux, suggesting a slowdown of the tropical circulation in

[2]Representative Concentration Pathway (RCP) experiments, in which GHGs are elevated to various levels depending on different emissions mitigation scenarios, are part of the CMIP datasets. RCP8.5 is the scenario with the most warming.

response to climate change. A weakening of the tropical circulation is a robust feature of climate projections, but there is not yet consensus on how this occurs [61]. According to Vecchi and Soden [107], in CMIP3 the weakening occurs mainly in the zonally asymmetric Walker circulation rather than in the zonally symmetric Hadley cells; however, Feldl and Bordoni [32] write that a weakening or slowdown of the Hadley circulation is a robust feature of climate projections. Ma et al. [61] have postulated the mean advection of stratification change (MASC) hypothesis to explain this modeled slowdown of the tropical circulation in both the Walker and Hadley cells (under MASC, climatological cooling/heating in regions of convection/subsidence counteracts the motion of these circulatory cells), while others have attributed the slowdown to an increase in gross moist stability [21, 22, 20, 23, 121]. Ultimately, Chadwick et al. [14] find that the spatial signatures of the thermodynamic (rich-get-richer) and dynamic (circulation slowdown) effects largely cancel in CMIP5; Wills et al. [120] also conclude from an analysis of precipitation minus evaporation that CMIP5 shows little spatial signature of the rich-get-richer mechanism.

A separate line of thinking, sometimes called the "warmer-get-wetter" hypothesis, attributes changes in rainfall under global warming primarily to sea surface temperature (SST) changes [125, 60]. This is related to the weak temperature gradient theory, according to which temperatures in the tropical troposphere show high spatial uniformity due to a small Coriolis effect and fast gravity waves smoothing out inhomogeneities [16, 17, 99], hence convection will be most sensitive to low-level SST variations. Meanwhile, Chadwick et

al. [14] argue that the spatial pattern of rainfall change is dominated by shifting convergence zones. None of these investigations into the precipitation response to GHG forcing, however, has emphasized the partitioning between convective and large-scale rain or explored the effect this structural constraint may have upon modeled rainfall projections.

Apart from global warming studies, I note again (see Section 2.6) Frierson's aquaplanet study of the interaction between convective and large-scale parameterizations [33]. Frierson [33] discovered that with only large-scale precipitation allowed, the tropical rainfall pattern showed reduced zonal symmetry, a stronger Hadley circulation, and an increase in energy export via transient eddies. With deep and shallow convective parameterizations active too, the Hadley circulation slowed and zonal rainfall bands appeared. Frierson's results suggest that larger f_{LS} will correlate with reduced efficiency of poleward energy transport by the Hadley circulation; it also suggests that models with larger f_{LS} will show stronger zonally asymmetric circulations with stronger monsoons and more energy export from the tropics via transient eddies.

In this chapter, I will argue that the circulatory and precipitation effects of CO_2 forcing can be greatly affected by the partitioning of convective and large-scale rainfall, although whether circulation and precipitation are enhanced or suppressed will depend on details of the model. Awareness of the impact of rainfall partitioning may allow for greater understanding of uncertainty in modeled rainfall projections. To this end, I use three climate model ensembles (described below) to explore connections between f_{LS} and other

variables, including projected precipitation patterns under global warming. In Sections 2 and 3, I describe the ensembles and use them to explore the relationship between f_{LS}, precipitation, and circulation both in control/historical climatologies and in the response to CO_2 forcing. Section 4 presents hypotheses explaining my findings and comments on the relationship between modeled and observed rainfall. Section 5 summarizes and concludes the chapter.

3.2 Ensembles

I use three climate model ensembles in this study. The first is a single-model ensemble (SME) representing a Bayesian calibration of the National Center for Atmospheric Research (NCAR) Community Atmosphere Model version 3.1 (CAM3.1) at a (T42) resolution of $2.8^\circ \times 2.8^\circ$ with 26 vertical levels. A collection of 3,336 fixed-SST experiments were computed with this model as part of a Markov Chain Monte Carlo sampling via Multiple Very Fast Simulated Annealing (MVFSA), by varying 15 model parameters related to clouds and precipitation and running each parameter setting for four years. From the 3,336 simulations, roughly half represented samples from the posterior distribution. These 1,800 models were ordered based on a test statistic of model skill [47, 46, 127, 45, 110], and every tenth model was used to create a 180-member ensemble. Each member of this ensemble performed as well as or better than the CAM3.1 default configuration. The parameter settings from these experiments were then used to conduct global warming experiments, running CAM3.1 coupled to a slab ocean for forty years with modern CO_2

levels and forty years doubled CO_2, the last twenty years of each being averaged for analysis. The same calculated set of ocean heat fluxes was used for all experiments in both control and $2\times CO_2$ runs.[3]

An updated version of the NCAR model, the Community Atmosphere Model version 5.3 (CAM5.3), was used to create a second, 98-member SME at a 0.9° latitude by 1.25° longitude resolution with 30 vertical levels selected from 505 experiments using MVFSA sampling. Using a finite-volume dynamical core, these experiments were run for 4.5 years each, with the last four years averaged for analysis. The response to $2\times CO_2$ made use of a "modified Cess" experiment design intended to reduce computational expense. In the original Cess experiment design, experiments are carried out with prescribed SSTs, which are uniformly increased for the $2\times CO_2$ experiments. In a modified Cess experiment, SSTs remain fixed, but for the $2\times CO_2$ experiments they are increased according to a predetermined spatial pattern, for example, one found by running a single $2\times CO_2$ experiment to equilibrium [13, 35, 111]. The modified Cess experiments provide an efficient means to estimate cloud feedbacks in response to CO_2 forcing. Here these same experiments are evaluated for CO_2-forced changes in precipitation. It is not clear how this experiment design affects the response relative to a coupled system model. For instance, where the CAM3.1 model and CMIP datasets show greater globally-averaged precipitation responses for higher climate sensitivities, the CAM5.3 ensemble

[3]For details on Bayesian calibration, the MVFSA sampling method, and the test statistic and observational records used in generating the CAM3.1 ensemble, see Appendix C.

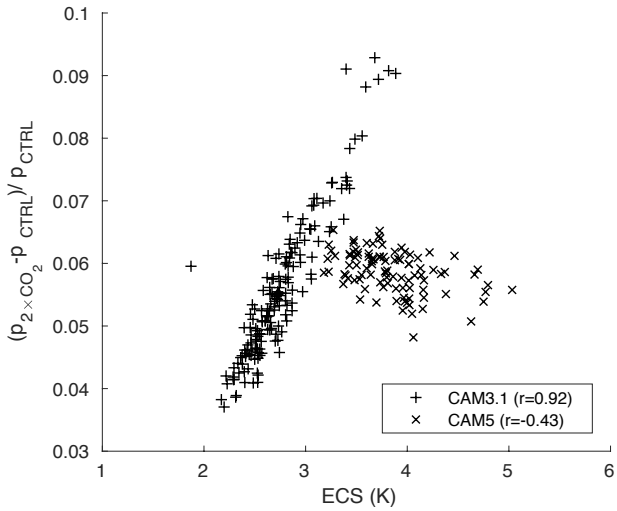

Figure 3.1: Global mean precipitation response ($\Delta P/P$) for the CAM3.1 and CAM5.3 ensembles versus equilibrium climate sensitivity (ECS). The CAM3.1 slab ocean experiments are consistent with results from CMIP, while the CAM5.3 modified Cess experiments show a negative though weaker trend.

shows a slight decrease in rainfall response for higher sensitivities (Figure 3.1). Despite questions about the modified Cess experiments, the spatial pattern of the response had features in common with the CMIP5 dataset and therefore it was decided to include the CAM5.3 ensemble results as well.[4]

The CMIP5 data used here were taken from the "historical" simulations and the RCP8.5 (high emissions) experiments. I averaged precipitation data over the final twenty-year intervals: 1986-2005 for the historical experiments and 2081-2100 for the RCP8.5 scenarios. I was able to gather the necessary data from 33 CMIP5 models, which I regridded to match the CAM3.1 grid for comparison. Three of the 33 CMIP5 models had responses noticeably further

[4]Again, see Appendix C for additional details.

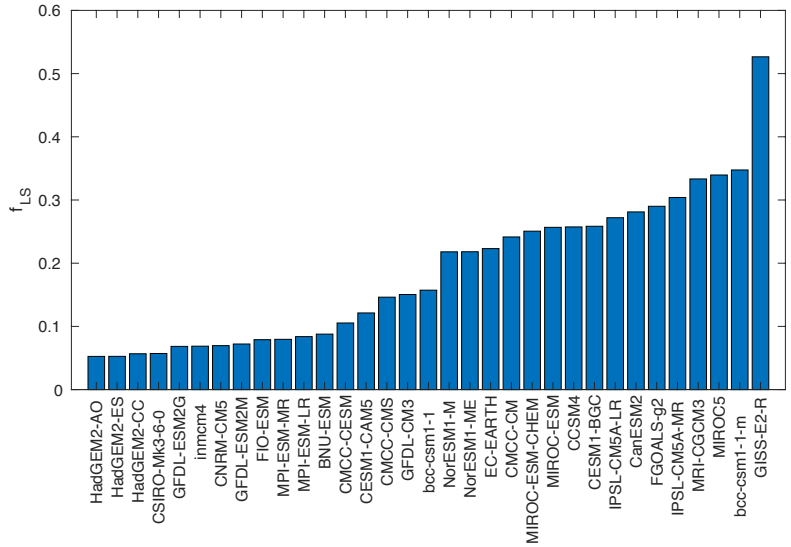

Figure 3.2: The range of f_{LS} for the 33 CMIP5 ensemble members. The f_{LS} range for CMIP5 is comparable to that for the CAM5.3 ensemble and much wider than the range for the CAM3.1 ensemble.

from the mean response, but excluding these experiments does not greatly affect these results, so they were kept. Noteworthy differences between the two CAM and the CMIP5 ensembles are first that, in the latter, CO_2 is not specifically doubled but rather increased to a level consistent with the RCP8.5 scenario at year 2100, and second, the CMIP5 models include dynamic oceans whereas the CAM ensembles do not.

These ensembles show different ranges of f_{LS}. For the CAM3.1 ensemble, f_{LS} ranges from roughly 3% to 12% with an average of about 6%. (CAM3.1 also includes a shallow convective precipitation rate; however, this is included in the total convective rainfall rate. I comment briefly on the relationship between convective, shallow convective, and large-scale rain in the CAM3.1 ensemble below.) For the other ensembles, f_{LS} values can be much

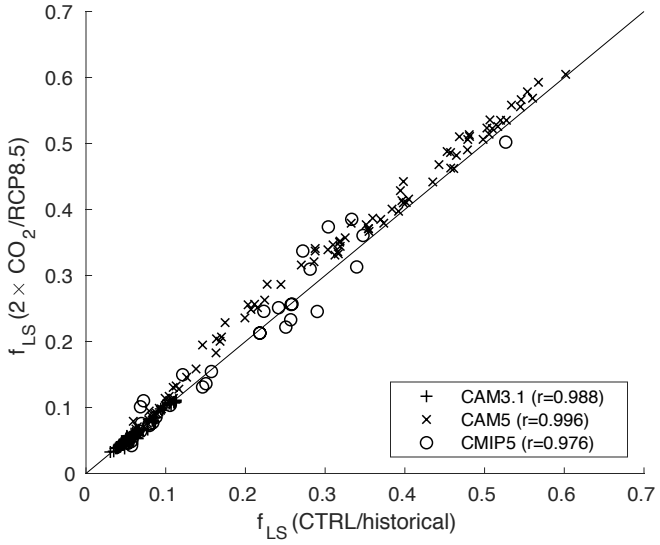

Figure 3.3: The fraction of tropical large-scale rain is a relatively fixed property of a climate model in both CAM ensembles and in CMIP5.

larger: in CAM5.3, the range is from roughly 5% to 60% (average ∼29%), while for CMIP5, the range is from roughly 6% to 53% (average ∼19%, see Figure 3.2). However, while f_{LS} may exhibit a wide range of values, once the physical parameters of a particular climate model are set, the fraction of tropical large-scale rainfall is a relatively fixed property of that model: correlations between control and global-warming f_{LS} are very high (of the three ensembles, the lowest correlation was ∼0.98 for CMIP5), and f_{LS} only changes by a few percent on average with global warming (Figure 3.3). The ensemble showing the most change with global warming is the CAM5.3 ensemble, with an average increase in f_{LS} of about 8.5%. Hence I use the control (CAM) or historical (CMIP5) f_{LS} for sorting ensemble members throughout this chapter.

This experimental design allows one to determine the parameters most

closely correlated with f_{LS} in the CAM ensembles. Because a number of parameters related to clouds and rainfall were perturbed in the CAM3.1 and CAM5.3 ensembles,[5] it is difficult to tease apart the effects of individual parameters on f_{LS}, and indeed this was not the original intention behind the construction of these ensembles. More careful studies of specific parameters have been carried out; the CAPE-consumption time-scale *tau* in particular has been studied in some detail in various settings [64, 126, 118, 36, 56]. In the CAM3.1 ensemble, f_{LS} is most sensitive to changes in *icritc* (the cold ice autoconversion threshold, with a correlation with f_{LS} of about 0.68), *alfa* (the initial cloud downdraft mass flux, correlation $\sim$0.61), and, consistent with previous studies, *tau* (correlation $\sim$0.50). These parameters are not necessarily independent of each other: I find that both *tau* and *alfa* are correlated with *icritc* (with coefficients of $\sim$0.72 and $\sim$0.44 respectively). Negative correlations with f_{LS} are weaker, but the strongest is with *c0*, the precipitation efficiency, which determines how much condensate rains out; a less efficient rainout leaves more condensate in the atmosphere, allowing for more grid-scale rain later [130]. In the CAM5.3 ensemble, f_{LS} is most sensitive to changes in *tau* ($\sim$0.84 correlation with f_{LS}). The other parameters show much weaker correlations, starting with *criqc* (the maximum updraft condensate) at $\sim$0.34. However, there is a very strong correlation ($\sim$0.92) in the CAM5.3 ensemble between f_{LS} and the globally averaged 10-meter wind speed. I speculate that this sensitivity to

[5] Fifteen and seven parameters were varied in the CAM3.1 and CAM5.3 ensembles respectively—a detailed list is given in Table C.1.

the surface wind, and the resultant effect on evaporation and precipitation, is a result of changes to the CAM Zhang-McFarlane convection scheme, which was modified starting with CAM4 to include convective momentum transport [83, 68]. It is possible, however, that the causality runs in the opposite direction: less convection could lead to greater instability, higher levels of CAPE, and stronger surface winds. Other papers have looked at relationships between parameters and rainfall [40, 118, 117, 62, 36], as well as the connection between rainfall partitioning and rainfall intensity [51, 72]. Jackson et al. [46] found that larger values of *tau* are correlated with extreme rain events in CAM3.1, which suggests a connection between rainfall intensity and f_{LS}, but with only monthly-averaged data I am unable to comment on that relationship here.

I further considered the effect of model resolution on f_{LS} in the ensembles, since as resolution grows higher, grid cells become smaller, conceivably making it easier to reach the saturation threshold for the microphysics parameterization to generate large-scale rain. A number of studies have shown that resolution is important in determining f_{LS} [3, 51, 72], but this experimental setup limits what I can conclude in this regard. Based on the CAM ensembles, wherein the higher-resolution CAM5.3 ensemble is capable of generating much larger f_{LS}, one might conclude there is a connection, but would need to test each model independently at different resolutions to draw a robust conclusion. (I find that the CMIP5 ensemble, which includes a range of model resolutions, shows a weak relationship between horizontal resolution and f_{LS}, with a correlation of 0.17 between them.)

3.3 Findings

Rainfall and circulation patterns within the CAM ensembles show clear and strong relationships with f_{LS}, both within control climatologies and in response to CO_2 forcing. In the first part of this section, I document the strong relationships between control and response spatial rainfall patterns and f_{LS}, and I quantify their significance. In the second part, I discuss the important ways in which models show different or even opposite behavior with f_{LS}, despite their shared strong correlations between f_{LS} and rainfall and circulation.

3.3.1 Variations in rainfall and circulation with f_{LS}

Despite the comparatively small range of f_{LS} in the CAM3.1 ensemble, I find a fairly smooth transition between rainfall response patterns when binning response anomalies by f_{LS} (Figure 3.4). The most dramatic transition is in the Pacific, where for smaller f_{LS} (i.e., more convective rainfall) there is a greater increase in rainfall along the equator and comparatively less on the poleward flanks. These patterns are reversed across much of the Pacific in the high-f_{LS} case, where there is less of an increase in rainfall in the deep tropics and less of a decrease in the subtropics. A connection between f_{LS} and monsoonal circulations is evident as well: for low f_{LS}, India dries in the response, while for large f_{LS}, India gets wetter (this effect also shows up in the Figure 3.4 anomalies). The highest-f_{LS} experiments for the CAM3.1 ensemble are anomalous in some ways which I point out as necessary below. This anomalous behavior for the highest-f_{LS} experiments illustrates the complexity

and nonlinearity of the handoff from convective to large-scale rain and suggests the possibility of different kinds of equilibria as f_{LS} rises.

Locally the rainfall response with f_{LS} can be substantial. In the deep tropical Pacific (160W, 0N), the high-f_{LS} experiments show on average 49% less of a response while the low-f_{LS} experiments show on average 47% more. In the Caribbean (60W, 15N) the corresponding numbers are about 26% more for high-f_{LS} and 19% less for low-f_{LS}. In the Indian Ocean (90E, 15S), the corresponding numbers are about 31% less for high-f_{LS} and 14% more for low-f_{LS}. Hence f_{LS} can have a considerable impact on local rainfall responses.

In the CAM5.3 ensemble, I again find a smooth transition between bins; Figure 3.5 includes only three bins due to the smaller sample size. The pattern is more complex for the CAM5.3 ensemble than for the CAM3.1 ensemble, due in large part to a Pacific zonal asymmetry. In CMIP5, again with three bins in Figure 3.6, some areas, for example the northern Pacific, show a transition, but overall the transition with f_{LS} is less smooth than in the CAM ensembles. I expect this is due at least partly to small sample size and greater scatter among the CMIP5 models, several of which are noticeably different from the mean CMIP5 response, in addition to the dynamic oceans in CMIP5 models.

The response anomaly maps shown in Figures 3.4-3.6 are suggestive of a correlation between f_{LS} and the precipitation response pattern, particularly within the CAM ensembles, but to quantify the importance of f_{LS} for the response patterns and remove any dependence on an arbitrary binning scheme, I employ a standard analysis using empirical orthogonal functions (EOFs).

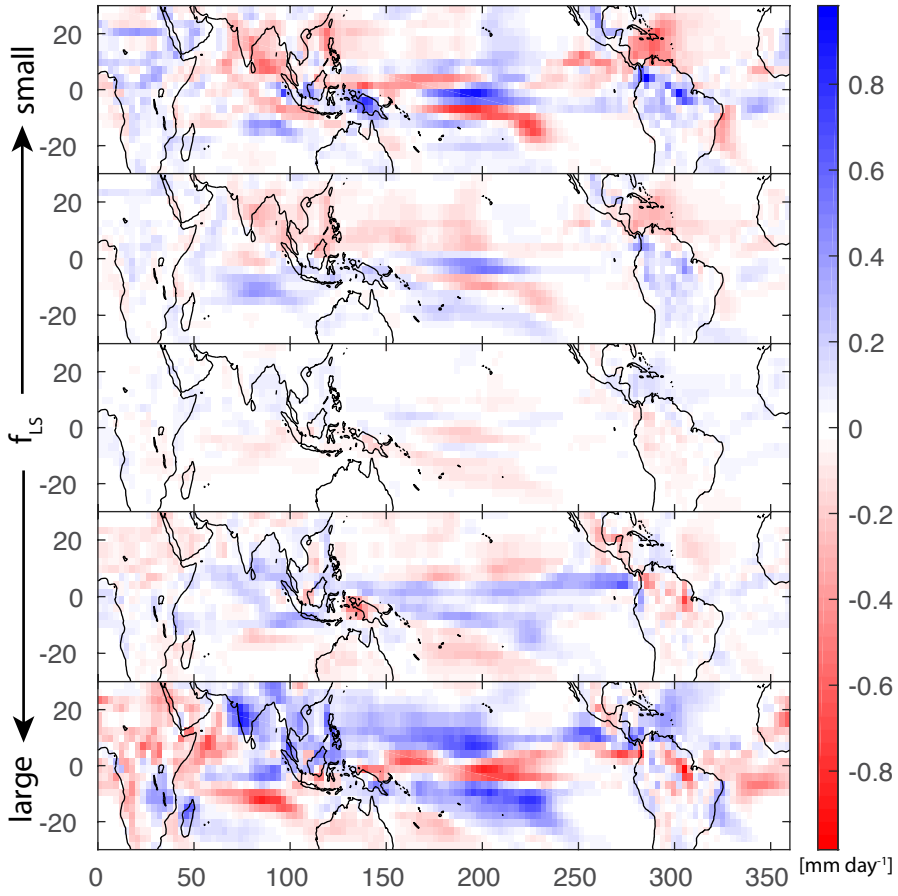

Figure 3.4: Rainfall response ($2\times CO_2$ minus control) anomalies for the CAM3.1 ensemble, averaged over five bins defined by a simple scheme based on the mean and standard deviation for f_{LS} (Figure C.1). From top to bottom, the bins contain 8, 42, 90, 9, and 16 experiments.

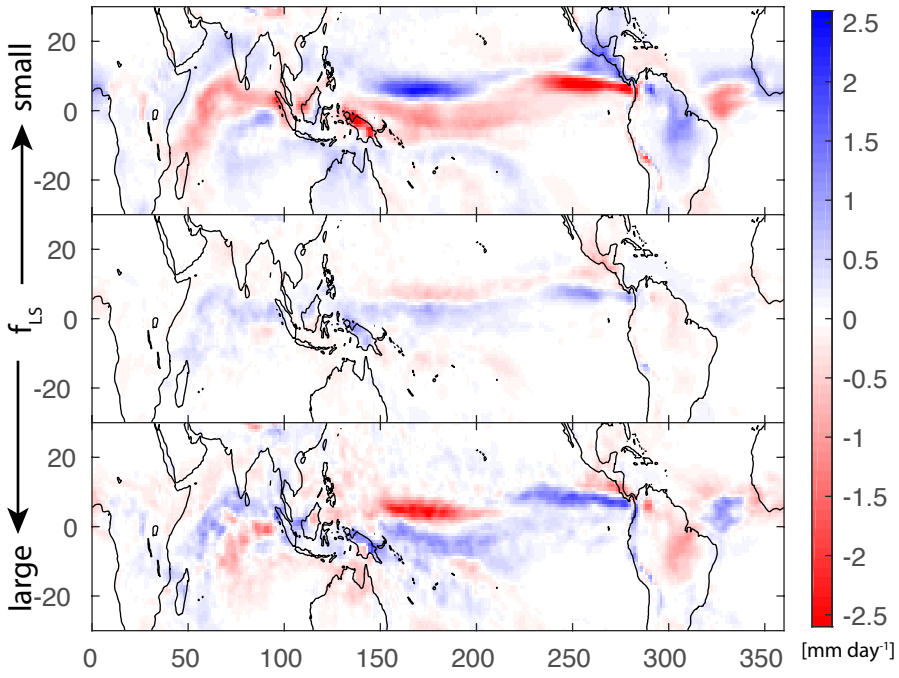

Figure 3.5: Rainfall response ($2\times CO_2$ minus control) anomalies for the CAM5.3 ensemble, averaged over three bins defined by a simple scheme based on the mean and standard deviation for f_{LS} (Figure C.1). From top to bottom, the bins contain 27, 49, and 22 experiments.

By the method described in Appendix D, in which I defined maps $\Delta R'$ representing the effect of f_{LS} on each ensemble's precipitation response pattern (Figure 3.7), I conclude that for the CAM3.1, CAM5.3, and CMIP5 ensembles, the respective $\Delta R'$ patterns account for 13.6%, 35.6%, and 11.0% of the total precipitation response variance. I expect the dynamic oceans in CMIP5 models to contribute significantly to the response variance.

One can also quantify the linearity of the transition from the low-f_{LS} pattern to the high-f_{LS} pattern by projecting onto $\Delta R'$ each of the response anomalies ($A_i \cdot \Delta R'$) as in Figure 3.8. For the two CAM ensembles, this pro-

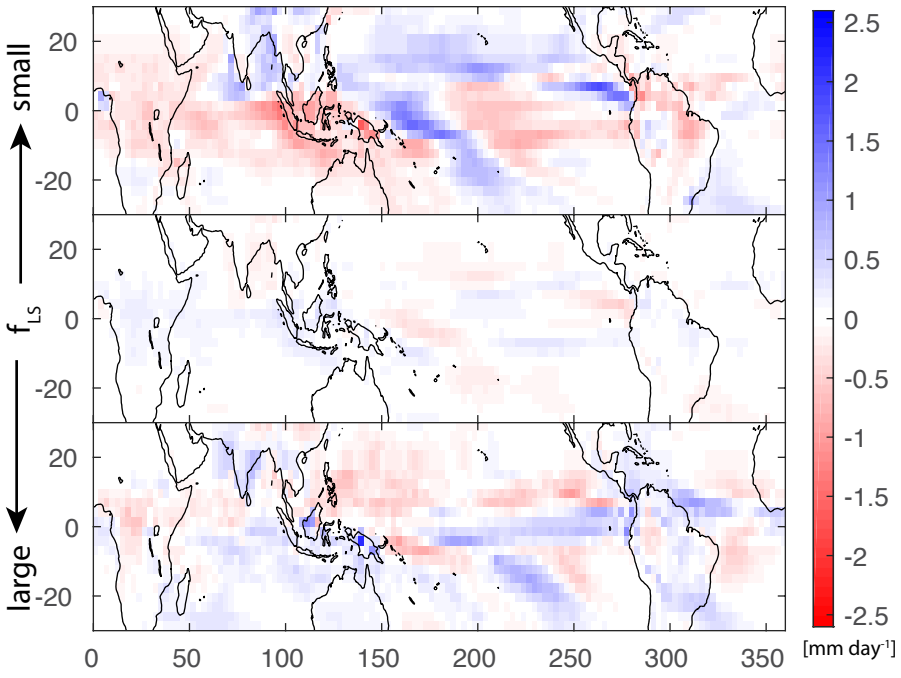

Figure 3.6: Rainfall response (RCP8.5 minus historical) anomalies for the CMIP5 ensemble, averaged over three bins defined by a simple scheme based on the mean and standard deviation for f_{LS} (Figure C.1). From top to bottom, the bins contain 6, 22, and 5 experiments.

duces fairly linear plots. For the CAM3.1 ensemble, the correlation is ∼0.75, with the somewhat anomalous behavior of the highest-f_{LS} experiments (mentioned above) evident in the graph. For the CAM5.3 ensemble, the correlation is ∼0.95 and the transition is smoother. For the smaller CMIP5 ensemble, a smooth transition is less apparent in the maps of Figure 3.6, but in this calculation some linearity is still evident with a correlation of ∼0.61 (as noted above, the CMIP5 dataset includes several models that are noticeably far from the mean response; these models bring down the correlation slightly). To quantify these results' dependence on the high- and low-f_{LS} cutoffs, I carried out the same calculation while varying the number of experiments in the high and low

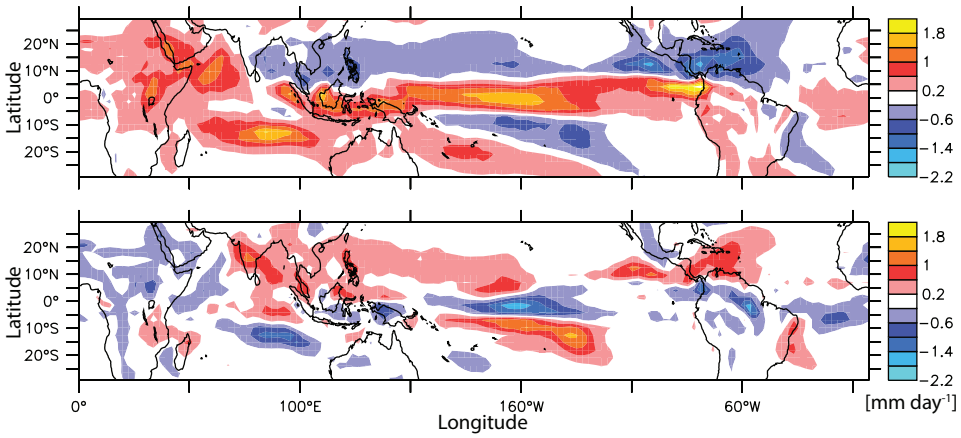

Figure 3.7: Top: the average response of the CAM3.1 ensemble to a doubling of atmospheric CO_2. Bottom: ΔR as defined by Eq. (D.1), showing the effect of f_{LS}. High f_{LS} has the effect of counteracting much of the ensemble mean response.

bins separately from two to 30 experiments each. Over all 841 calculations, the average correlation for the CAM3.1 ensemble is $\sim$0.72 with a standard deviation of $\sim$0.06. Over the same calculations for the CAM5.3 ensemble, the average correlation is $\sim$0.96 with standard deviation < 0.01. I therefore conclude that the changing spatial patterns of the rainfall response with f_{LS} is a robust result that does not depend strongly on the binning scheme.

The CAM5.3 ensemble shows a larger response anomaly amplitude than the CAM3.1 ensemble or the CMIP5 dataset; I believe the reasons for the larger spread with respect to the CAM3.1 ensemble are twofold. First, while the adjusted parameters for the CAM5.3 ensemble are not all the same as those for the CAM3.1 ensemble, those parameters that are adjusted in both ensembles (e.g. *tau, rhminl*) range more broadly for the CAM5.3 ensemble.[6]

[6]See Table C.1.

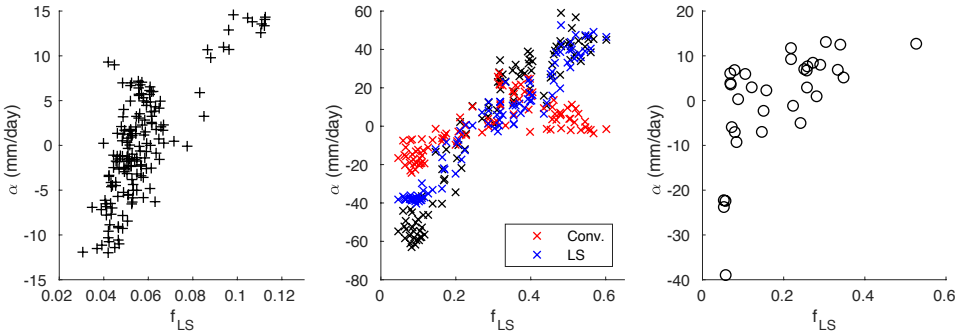

Figure 3.8: In black: the dot product of rainfall anomalies $\alpha_i = A_i \cdot \Delta R'$ (see Eq. D.3), versus $f_{\rm LS}$. From left to right, the CAM3.1 ensemble ($r = 0.75$), the CAM5.3 ensemble ($r = 0.95$), and the CMIP5 dataset ($r = 0.61$). (Note that the p-values for all of the scatter plot correlations given throughout this chapter are very small, $P < 0.001$, and henceforth I only report the correlations.) The linearity of these data points gives an indication of how smoothly the response varies between extremes with $f_{\rm LS}$. For the CAM5.3 ensemble, I have also included the contribution to the total (black) data from convective rain only (red) and large-scale rain only (blue). In this case, fitting the total, convective, and large-scale rain α values using linear regression indicates that large-scale rain makes up roughly 77% of the total pattern, with convective raining making up the remaining 23%. (For the CAM3.1 ensemble and the CMIP5 dataset, convective rain dominates the total pattern.)

Hence a wider range of responses may be expected for the CAM5.3 ensemble. Second, the large-scale rain rate in the CAM5.3 ensemble shows more sensitivity to these adjustments than in the CAM3.1 ensemble. In Figure 3.8, the vertical spread for the CAM3.1 ensemble is due almost entirely to variation in convective rainfall, while for the CAM5.3 ensemble, both convective and large-scale rain contribute to the overall spread, with large-scale rain contributing more (as shown in Figure 3.8, large-scale rain makes up about 77% of the overall pattern, with convective rain making up for the remaining 23%). Hence the greater sensitivity of the large-scale rainfall in the CAM5.3 ensemble contributes to an overall larger amplitude of response anomaly. The CMIP5 ensemble follows the CAM3.1 ensemble pattern, with a greater contribution

from convective rain to the total spread in response anomaly.

Neither CAM ensemble shows a strong signature of the rich-get-richer mechanism between 30°S and 30°N (Figure 3.9 shows the ensemble control rainfall patterns). For the CAM3.1 ensemble, the largest spatial correlation between control rainfall P and the $2\times CO_2$ response ΔP in this region is close to 0.5, but the average spatial correlation is $\sim$0.12, while for the CAM5.3 ensemble, the largest correlation is less than 0.25 with a similar average of $\sim$0.12. In the zonal mean, the ensemble-mean correlations between P and ΔP are $\sim$0.47 and $\sim$0.41 respectively. (For the 33-member CMIP5 dataset, I find, consistent with [14], that the ensemble-mean spatial correlation between between P and ΔP is close to 0.3. However, in the zonal mean, the ensemble-mean correlation between P and ΔP rises to about 0.73.) Nevertheless, the spatial patterns of both control and $2\times CO_2$ rainfall do show a relationship with f_{LS}. As f_{LS} increases in the control experiments, the spatial correlation between large-scale and convective rain (between 30S and 30N and globally as well) grows more positive, as shown in Figure 3.10. In the CAM5.3 ensemble, this effect appears to saturate as f_{LS} gets large, but for the CMIP5 ensemble, which has a similar range of f_{LS}, this is less clear. Judging by Figure 3.10, large-scale and convective rain tend to be active in different areas for low f_{LS}, while for larger f_{LS} they tend to work in tandem. The same effect is observed for the $2\times CO_2$ experiments, also shown in Figure 3.10.

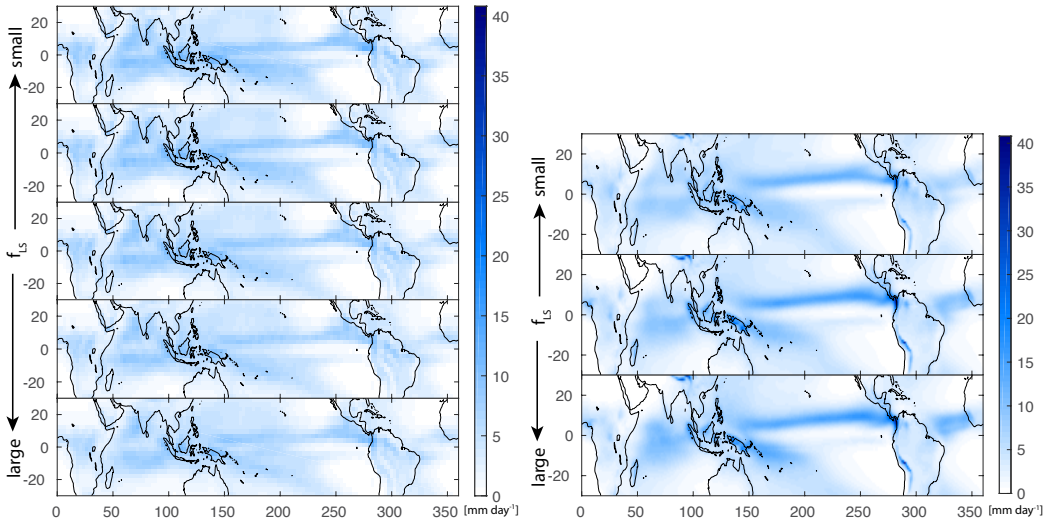

Figure 3.9: Left: control precipitation climatology for the CAM3.1 ensemble, averaged over five bins defined by a simple scheme defined in Appendix C (Figure C.1) and used in Figure 3.4. Right: control precipitation climatology for the CAM5.3 ensemble, averaged over the three bins defined by Figure C.1 and used in Figure 3.5. It is fairly clear from a comparison of these figures with Figures 3.4 and 3.5 that there is not a strong spatial signature of the rich-get-richer mechanism in the CAM ensembles.

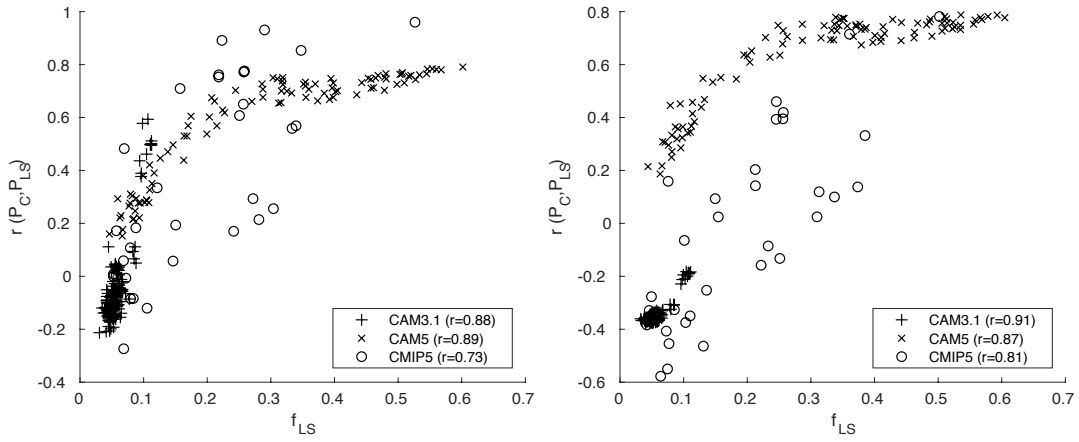

Figure 3.10: Left: The tropical (30S-30N) spatial correlation r between convective (P_{C}) and large-scale (P_{LS}) components of rainfall versus f_{LS} for the control/historical experiments for the three ensembles. The correlation becomes more positive as f_{LS} increases; the same trend applies globally as well, with even higher correlations for all three ensembles (not shown). Right: The same figure for the $2\times CO_2$ experiments. I believe these correlations are meaningful even at small f_{LS}, because as maps of the CAM3.1 ensemble large-scale rain shows (Figure 3.20), small amplitude is still consistent with a coherent spatial pattern.

3.3.2 Differing dependence on f_{LS} in CAM3.1 and CAM5.3

I have shown that the CAM ensembles and the CMIP5 dataset show strong and systematic variations with f_{LS}; however, despite these strong correlations, there are important ways in which the models differ in their dependence on f_{LS}. In the CAM3.1 control simulations, as f_{LS} grows the annual mean convective rain rate tends to decrease at all latitudes, and especially in the tropics. Large-scale rain shows less systematic variation with f_{LS}, except in the tropics and subtropics where it increases slightly (but with considerable percentage changes) and consistently with f_{LS} (Figure 3.11). However, large-scale rain is unable to make up for the loss of convective rain, with the possible exception of the highest-f_{LS} experiments: as f_{LS} gets into the higher

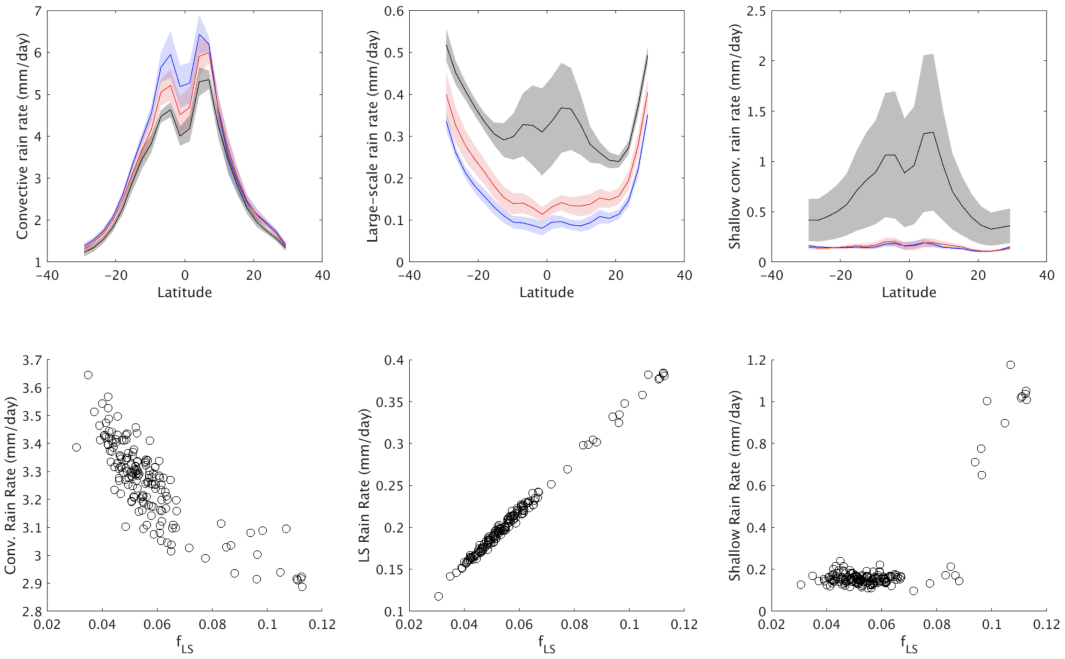

Figure 3.11: Top row: from left to right, the zonal mean convective, large-scale, and shallow rain rates for the CAM3.1 ensemble divided into three bins by f_{LS} similar to Figure 3.5 (blue, $f_{\mathrm{LS}} < 0.041$; red, $0.041 < 0.073$; black, $f_{\mathrm{LS}} > 0.073$). The shading behind each line shows one standard deviation for each bin. While convective rain falls off gradually with rising f_{LS}, the large-scale rainfall gradually rises until the highest-f_{LS} experiments show a more abrupt increase. A similar pattern holds for the shallow convection, except the lower-f_{LS} experiments largely overlap. Bottom row: from left to right, the tropical average convective, large-scale, and shallow rain rates for the CAM3.1 ensemble versus f_{LS}. Again it is evident that the shallow convection exhibits an abrupt increase for sufficiently high f_{LS}.

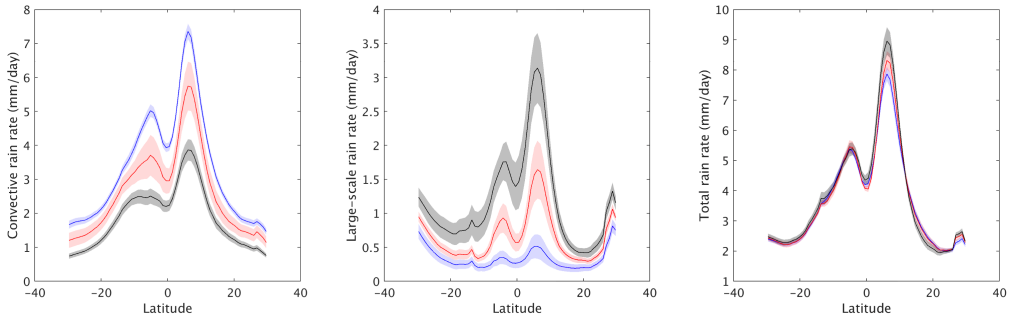

Figure 3.12: The zonal mean convective (left), large-scale (middle), and total (right) rain rates for the CAM5.3 ensemble binned by f_{LS} according to the scheme described in Appendix C accompanying Figure C.1 (blue, $f_{\mathrm{LS}} < 0.13$; red, $0.13 < f_{\mathrm{LS}} < 0.46$; black, $f_{\mathrm{LS}} > 0.46$). The shading behind each line shows one standard deviation for each bin.

range for the CAM3.1 ensemble (7-13%), there is a more substantial increase in large-scale rain in the deep tropics and along the Intertropical Convergence Zone (ITCZ). In the CAM5.3 ensemble, the situation is different, again with a substantial decrease in convective rain (about 50%) as f_{LS} rises, but with more-than-compensating increases in large-scale rain, hence the total amount of rainfall increases slightly (Figure 3.12). In the CAM3.1 ensemble, therefore, as parameter settings inhibit the convective parameterization, moisture that is not used up by the convective subroutine may or may not flow to other areas which then see more large-scale rain, but for the most part there is simply less convective rain, hence f_{LS} increases. In the CAM5.3 ensemble, parameter settings that inhibit convective rain ultimately allow for even more large-scale rain, increasing the amount of total rainfall.

Upon investigating the spatial patterns of the large-scale rainfall in the CAM3.1 ensemble, it became apparent that the large-scale rain grows steadily in the tropics and subtropics as f_{LS} rises while convective rain falls with f_{LS}

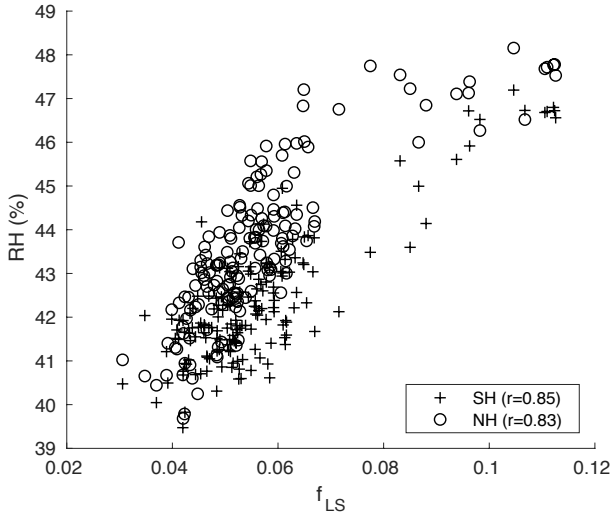

Figure 3.13: Annual-mean relative humidity versus $f_{\rm LS}$ for the northern hemisphere (NH) and southern hemisphere (SH) in the CAM3.1 ensemble. For the NH, the relative humidity is zonally- and column-averaged between 10°N and 30°N. For the SH, I plot the same quantity between 10°S and 30°S.

in both regions (this can be seen in the top middle panel of Figure 3.11). I subsequently found that $f_{\rm LS}$ correlates well with relative humidity throughout the tropics, but especially strongly in the subtropics. Between 10°N-30°N and 10°S-30°S respectively, the correlations between $f_{\rm LS}$ and the zonal-mean, column-averaged relative humidity are $\sim$0.83 and $\sim$0.85 (see Figures 3.13 and 3.14). I considered zonal averages of various quantities over the Pacific. These quantities show systematic variations with $f_{\rm LS}$, and I therefore chose the boxes to highlight changes in features of interest. Figure 3.14 shows the Pacific-averaged (130°E-260°E) relative humidity in the tropics, which increases with $f_{\rm LS}$, and the Pacific-averaged specific humidity tendency due to moist processes (anomaly) in the tropics, which shows that evaporation (condensation) decreases (increases) in the subtropics with $f_{\rm LS}$. Figure 3.15 shows the Pacific-

averaged omega and omega anomaly for the same experiments, together with the boxes ultimately selected for presentation in Figure 3.16.

I proceeded to explore the source of the moisture associated with the large-scale rainfall in the subtropical Pacific. In annual averages, I find that, averaged over the Pacific Ocean (130E-260E), averaged between 15°N and 20°N for the northern hemisphere (NH) and between 20°S and 25°S for the southern hemisphere (SH), and averaged between 500 and 700 mb, there are several variables correlated with f_{LS} (Figure 3.16): VQ (the product of the meridional wind and specific humidity), the cloud fraction, and the vertical pressure velocity *omega*. These relationships, which are evident seasonally as well, are most evident for $f_{\mathrm{LS}} < 0.08$ (shown in blue in Figure 3.16), where the correlation between VQ and f_{LS} is 0.63 in the NH and 0.72 for the SH. Within this region, there are also fairly strong correlations with cloud fraction and *omega*. This set of correlated variables suggests that for CAM3.1 parameter settings that give less rainout from the convective parameterization, more moisture is being detrained at midlevels in the tropics. There are nearly identical patterns, but with slightly stronger correlations, in the $2\times\mathrm{CO}_2$ experiments (not shown).

Along with these differences in rainfall behavior I find corresponding effects on the modeled tropical circulation, another way in which the models differ with f_{LS}. In the CAM3.1 ensemble, increasing f_{LS} in the CAM3.1 ensemble correlates with reductions in circulation and meridional fluxes of total (meridional mean, stationary, and transient eddy) potential energy and total

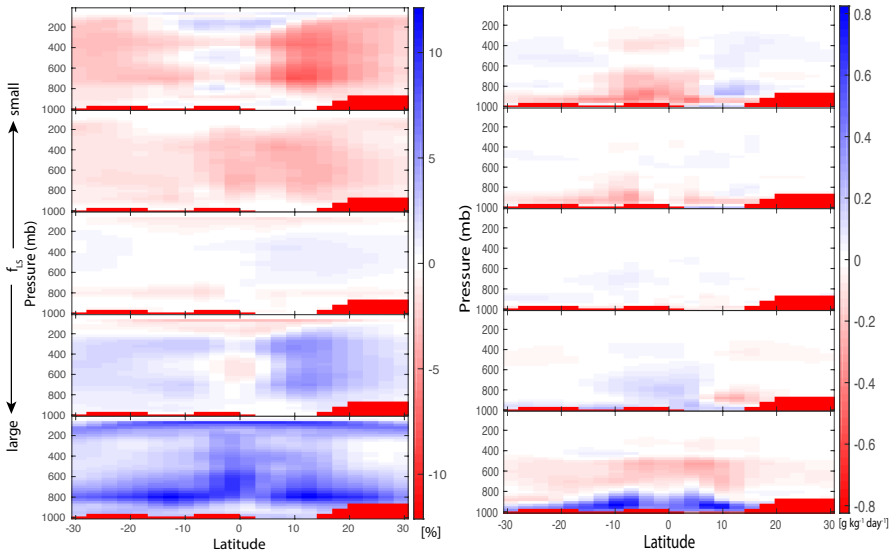

Figure 3.14: Left: Pacific-averaged (130°E-260°E) annual-mean relative humidity anomaly (i.e. with the ensemble mean relative humidity subtracted) in the tropics for CAM3.1 (same binning scheme as Figure C.1 above). The presence of greater amounts of moisture in the subtropics as $f_{\rm LS}$ increases leads one to ask the source of moisture for the subtropics, which would be associated with large-scale descent and drying. Right: For the CAM3.1 ensemble, the specific humidity tendency due to moist processes (with evaporation > 0 and condensation < 0) annual- and Pacific-mean (130°E-260°E) anomaly (i.e. with the ensemble-mean subtracted), binned by $f_{\rm LS}$ as in Figure C.1. Although the behavior of this variable is complex, it is evident that between 10°S-30°S and 10°N-30°N there is a tendency toward less evaporation and more condensation at mid-levels as $f_{\rm LS}$ increases.

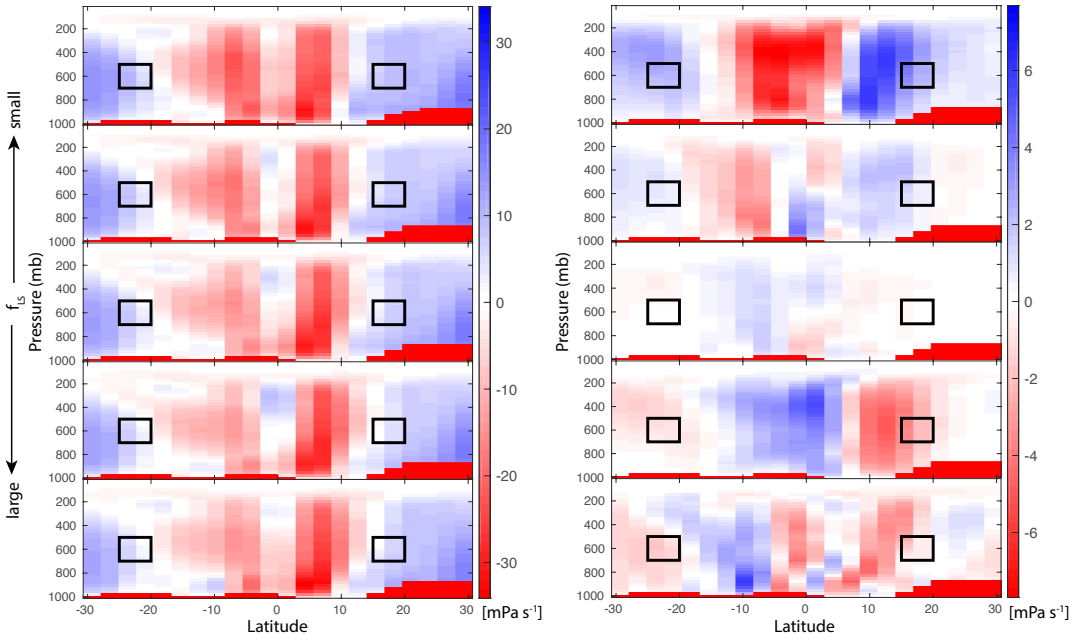

Figure 3.15: Pacific-averaged (130°E-260°E) annual-mean vertical pressure velocity omega (left) and the Pacific-averaged omega anomaly (right) in the tropics for CAM3.1 (same binning scheme as Figure 3.4). The anomaly is with respect to the ensemble mean omega (i.e. the ensemble mean is subtracted). Boxes indicate the regions ultimately selected for averaging in Figure 3.16.

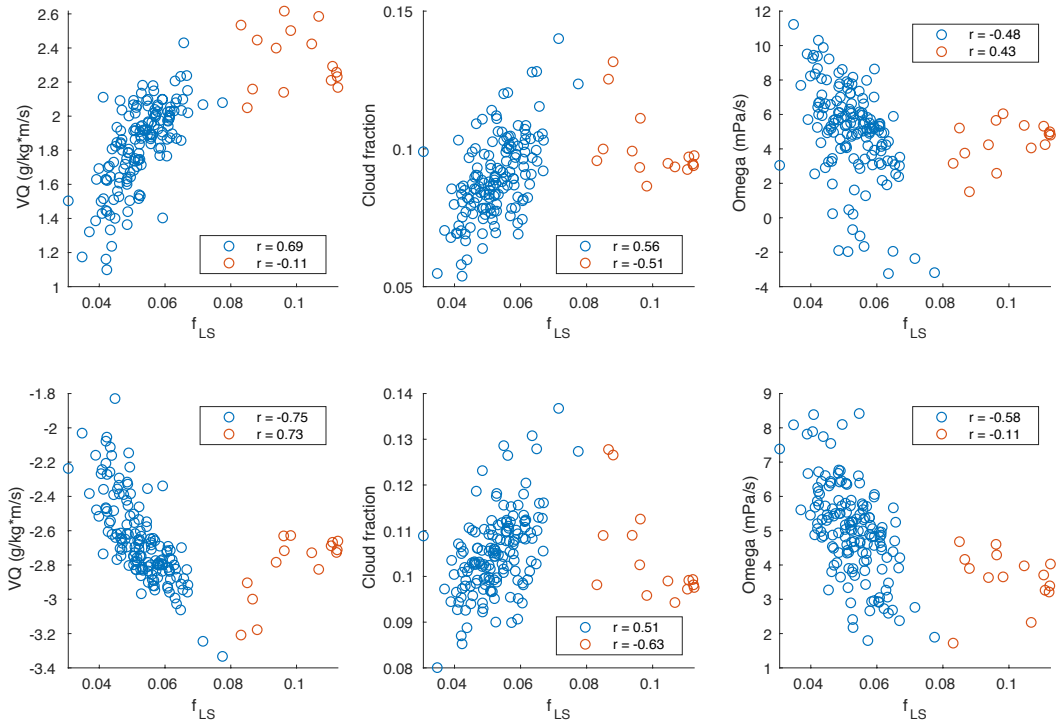

Figure 3.16: For both hemispheres, *VQ* (left), cloud fraction (middle), and vertical pressure velocity *omega* (right) in the CAM3.1 ensemble, averaged annually, over the Pacific (130°E-260°E), and between 500-700 mb, versus f_{LS}. The northern hemisphere quantities (top row) are averaged from 15°N-20°N, and the southern hemisphere quantities (bottom row) are averaged from 20°S-25°S (see supplemental material for details). Except for the highest-f_{LS} experiments (with $f_{\mathrm{LS}} > 0.08$, in red), these three variables show correlations of varying strength with f_{LS}, suggesting that midlevel detrainment of moisture from the deep tropics, and subsequent condensation in the subtropics, may play a role in weakening the mean meridional circulation.

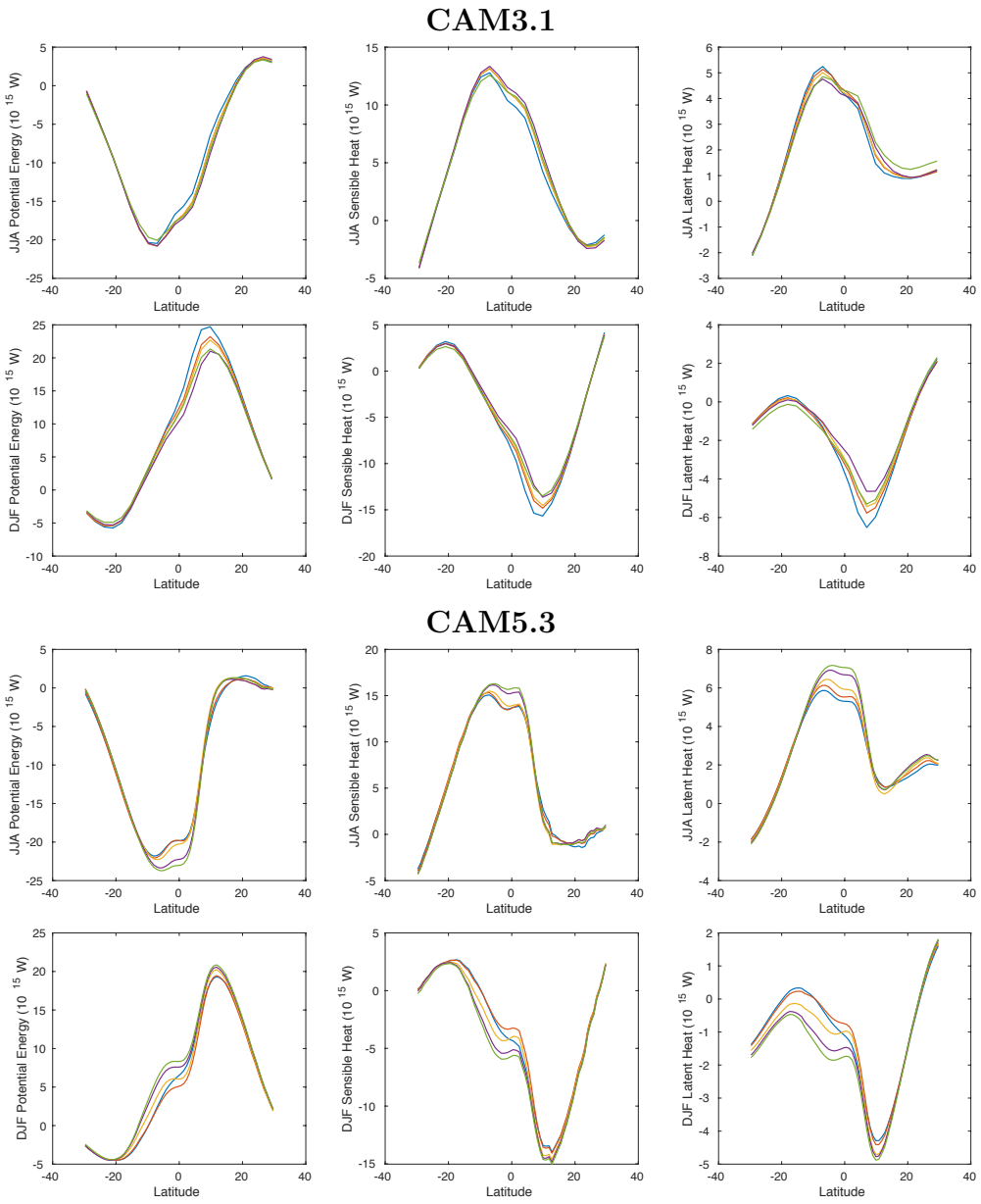

Figure 3.17: Upper half: Meridional fluxes of potential energy (left), sensible heat (center), and latent heat (right) for JJA (top) and DJF (bottom) for the CAM3.1 ensemble, binned by f_{LS} according to the scheme described in Appendix C. Particularly for DJF, the reduction in strength of the hydrological cycle is evident as f_{LS} increases. Lower half: the same figures for CAM5.3, binned by f_{LS} according to the scheme described in Appendix C.

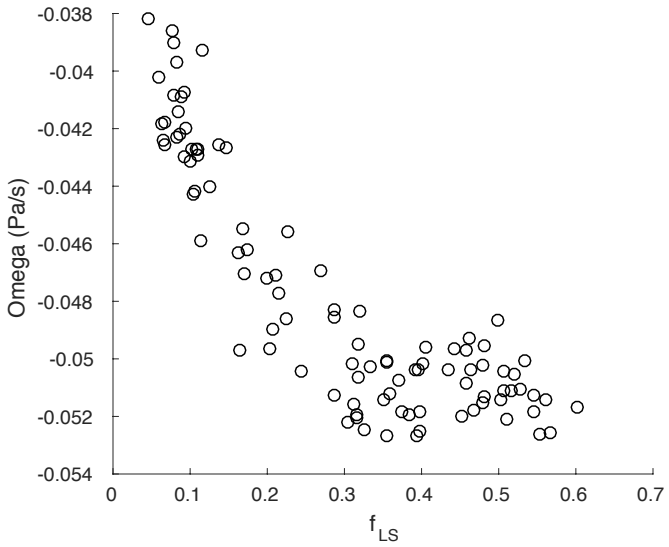

Figure 3.18: The CAM5.3 ensemble vertical pressure velocity (*omega*) at 800 mb on the ITCZ (approximately 6N) grows stronger with f_{LS}, similar to what was observed in Frierson (2007). The vertical average follows a roughly similar pattern. The effect seems to saturate as f_{LS} gets large, similar to the behavior of the CAM5.3 ensemble's spatial correlations between convective and large-scale rainfall in Figure 6.

sensible and latent heat. In the CAM3.1 control experiments, as f_{LS} grows there are reductions in the circulation of moist static energy, particularly in DJF (see Figure 3.17). The Pacific-averaged (130°E-260°E) vertical wind at 900 mb along the ITCZ (~ 5°N) weakens in DJF and JJA by about 70% in both cases as f_{LS} rises to $\sim$0.08. On the other hand, in the CAM5.3 ensemble the circulation strengthens with f_{LS}. On the ITCZ (about 6°N in this ensemble), the annual- and zonal-mean pressure velocity *omega* strengthens (*omega* grows more negative) until about $f_{\mathrm{LS}} = 0.35$ at which point the effect seems to saturate (Figure 3.18), similar to the behavior of the CAM5.3 ensemble's spatial correlations between convective and large-scale rainfall in Figure 3.10. This effect is further borne out by inspection of the stream func-

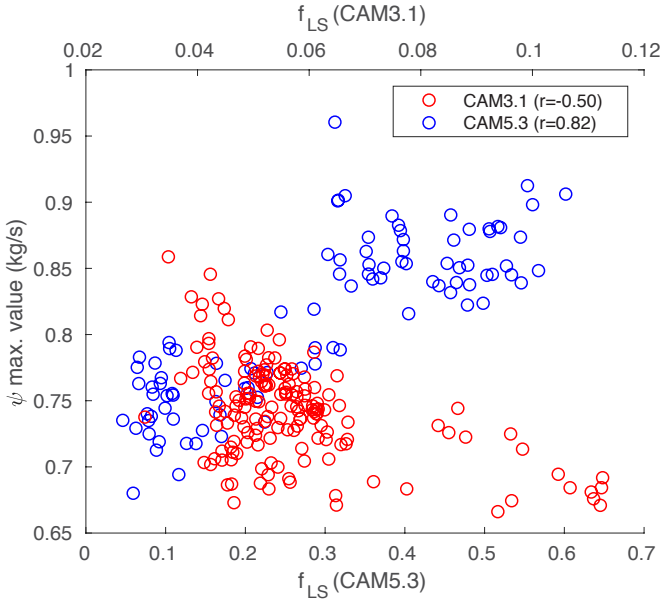

Figure 3.19: Maximum values of the annual-mean stream functions ψ for the CAM3.1 (blue) and CAM5.3 (red) ensembles. Note that the upper horizontal axis refers to CAM3.1 and the lower horizontal axis refers to CAM5.3. Consistent with Figure 3.18, the CAM5.3 ensemble ψ show increasing maxima as f_{LS} rises with a correlation of 0.82. For the CAM3.1 ensemble, maximum ψ values decrease with f_{LS}, although the correlation is weaker at -0.50. (Maximum values correspond to the northern branch of the mean meridional circulation, which shows up more clearly in the annual mean.)

tions, which show increasing transport via the mean meridional circulation for the CAM5.3 ensemble (Figure 3.19). Approximate seasonal meridional energy transport calculations are consistent with a strengthening of the Hadley circulation with increasing f_{LS}, showing that the Hadley cell is carrying more potential (sensible and latent heat) energy at higher (lower) levels as f_{LS} rises (Figure 3.17). Note that this does not imply total energy export from the tropics is increasing, since greater high-level energy outflow is offset by greater low-level inflow.

I note here a further observation specific to the CAM3.1 ensemble that is not evident in the CAM5.3 ensemble. Figure 3.11 shows large increases in both large-scale and shallow rain in the highest-f_{LS} experiments, as both seem to "turn on" abruptly for small convective rain rates. Spatially, the increase is largely in the areas where these rainfall types were already present; an exception is east of the Maritime Continent, where both large-scale and shallow rain increase suddenly in an area where lower-f_{LS} experiments show very little (see Figure 3.20). Shallow convection is present in both CAM ensembles, but the data were only kept for the CAM3.1 ensemble; nevertheless, the CAM5.3 ensemble does not show such abrupt rainfall changes with f_{LS}.

3.4 Discussion

My findings in the CAM ensembles demonstrate the considerable impacts that small differences in model parameterizations can have on control climatologies and on a model's response to global warming. However, my results also demonstrate that different models will not necessarily respond in the same way to such differences in parameterization. The CAM5.3 ensemble shows similarities to what Frierson [33] observed in his aquaplanet model, where more large-scale rain was associated with a stronger Hadley circulation and more rainfall. A similar mechanism may be at work here, and for the same reasons Frierson [33] supposes: a faster circulation makes up for a less efficient energy transport from the tropics caused by fewer convective plumes carrying moist static energy upward.

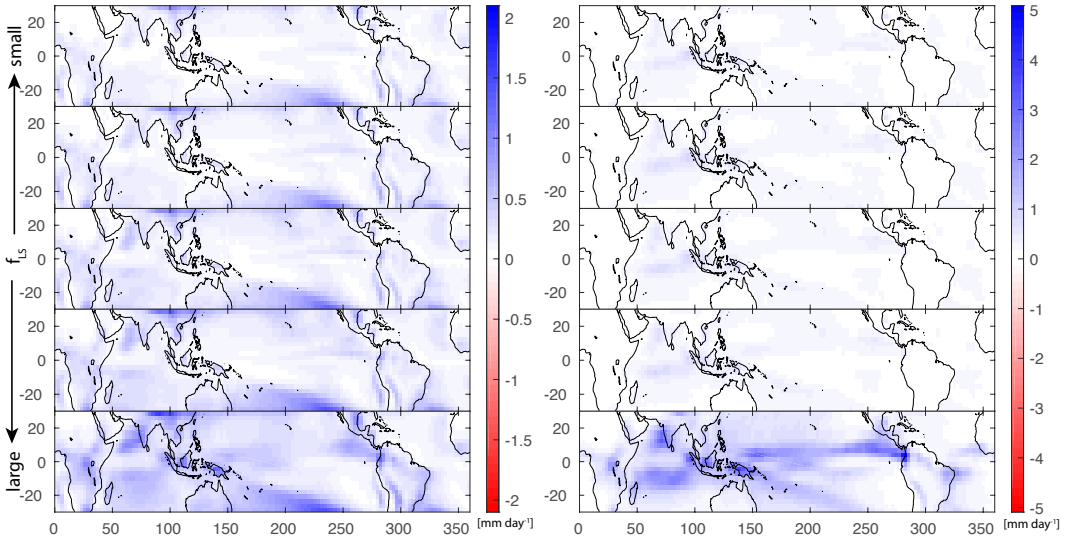

Figure 3.20: Control large-scale rainfall (left) and shallow rainfall (right) for the CAM3.1 ensemble, averaged over five bins defined by a simple scheme based on the mean and standard deviation for f_{LS} (see Figure C.1). For the highest-f_{LS} experiments, shallow rainfall rates increase dramatically throughout the tropics, and for both large-scale and shallow rain a patch of precipitation appears in the west Pacific, east of the Maritime Continent, which is unpronounced for lower-f_{LS} experiments. Pacific subtropical large-scale rainfall increases fairly steadily with f_{LS}.

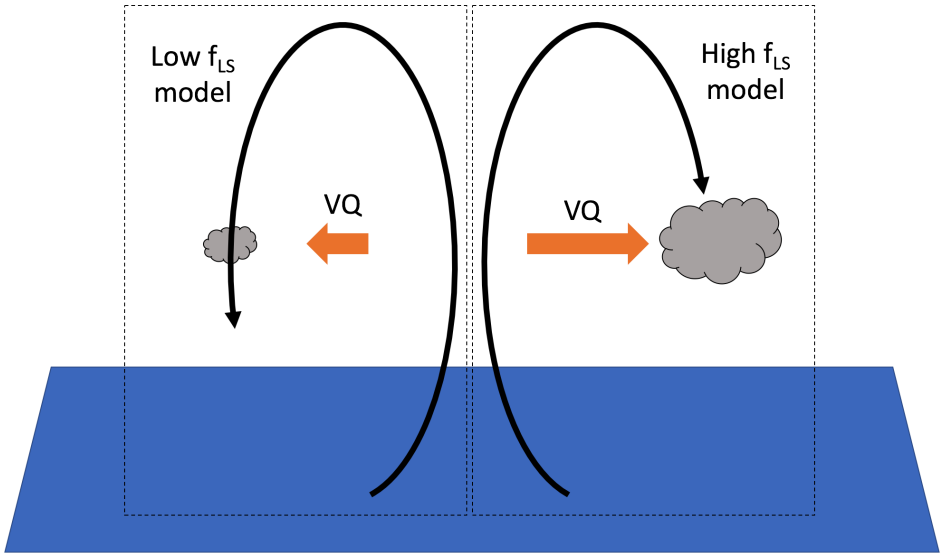

Figure 3.21: Under the "short-circuit hypothesis", parameter settings that give less convective rainfall in the tropics result in greater midlevel moisture transport from the tropics, resulting in condensation in the subtropics and counteracting the downward motion of the Hadley cell's descending branch.

The CAM3.1 ensemble shows different behavior with increasing f_{LS}, notably a weakening Hadley circulation, which requires a different explanation. I noted above that for parameter settings inhibiting convective rainout in the CAM3.1 ensemble, and therefore yielding higher f_{LS}, moisture deposited in the mid-troposphere by deep convection is being detrained to the subtropics at midlevels. I hypothesize that when this moisture condenses in the subtropics, the resulting diabatic heating (which would be associated with upward motion) counteracts the descending branch of the Hadley cell, weakening the downward motion. I refer to this as the "short-circuit mechanism" (Figure 3.21).

It is worth emphasizing the dramatic impact condensation in the sub-

tropics has on the vertical winds in these regions: in Figure 3.16, the magnitude of *omega* averaged between 500-700 mb varies by large fractions as f_{LS} rises from its lowest value up to $f_{\mathrm{LS}} \approx 0.08$. In the NH, *omega* varies by about 290% of the mean, while in the SH it varies by about 130%. These large reductions in the downward vertical wind strength are also observed seasonally. Subtropical large-scale condensation provides a plausible mechanism for what is observed in the CAM3.1 ensemble and highlights the remarkable sensitivity of the subtropics to condensation. This sensitivity may represent an important component of uncertainty in modeled rainfall responses to CO_2 forcing. Note that the ratio of mid-level detrainment to deep convection in the control climate has also been speculated to relate to the low cloud feedback [97].

That slight variations in how rainfall is partitioned in climate models have such dramatic effects on the modeled climate suggests more attention be paid to the ratio and distribution of convective and large-scale rain. Some efforts have touched on this topic [52, 105, 59]; in particular, Yang et al. [126] attempt to optimize a set of CAM5 parameters such that the model would agree with the conclusion of Schumacher and Houze [92] that about 40% of tropical rainfall is stratiform based on Tropical Rainfall Measuring Mission (TRMM) data. Either implicitly or explicitly, such studies typically assume that model-world convective and large-scale rain correspond to real-world convective and stratiform rain, but this assumption is questionable. Indeed, because f_{LS} is an artifact of climate model construction, it has no exact observational counterpart, and it is unclear how observational categories such as "convective" and

"stratiform" rain correspond to modeled convective and large-scale rainfall. The Schumacher and Houze [92] analysis of the TRMM data, for example, refers to high-level stratiform clouds in the tropics originating from deeply-penetrating convective clouds. It is not clear that the CAM large-scale rain variable always corresponds to this type of rain, particularly when considering that anvil-type clouds, which would fall into the category analyzed by Schumacher and Houze [92], are not explicitly represented in climate models.

There are various ways convective and stratiform rain can be distinguished in observations, including various algorithms [90] or by studying rainfall isotope ratios [1]. Huaman and Schumacher [41] distinguish convective from stratiform rain based on strength of vertical motion and type of raindrop growth (with shallow and deep convection distinguished by echo-top height). Based on such features of the various rainfall types, Huaman and Schumacher [41] extract latent heating profiles from radar data—in this case by combining TRMM Precipitation Radar (PR) with *CloudSat* Cloud Profiling Radar (CPR) data—to try to gain information on the vertical latent heating profile in the east Pacific. The TRMM PR is able to capture higher-level precipitation, but struggles with low-level shallow precipitation and has a threshold of 0.4 mm h^{-1}, hence it may underestimate low-level latent heating. The *CloudSat* CPR is better able to capture this low-level data, provided there is not too much attenuation due to heavy rain events.

Better understanding of how such observed rainfall types compare with those of model-world convective and large-scale rain could help to get the frac-

tion of large-scale rain right in models, however satellite data still may not give a complete picture. Difficulties and possible errors in satellite measurements prompt Huaman and Schumacher [41] to recommend more in situ observations to improve reanalysis datasets. There is room for improvement in representing the tropical circulation in reanalysis as well [100]. As alternative or complementary approaches, it may be possible, first, to repartition rainfall from models in a way that allows better comparison with existing observations. However, because there is no direct diagnostic for the altitude at which convective or large-scale rain forms in a given region, it is difficult to disentangle quantities better corresponding to observations from two-dimensional rainfall data. Hence it may be useful to have a model diagnostic carrying more information about where rainfall is generated. A second thought is prompted by the fact that models do not explicitly represent processes such as mesoscale convective systems (MCSs) which may be missed by the deep convective scheme. I speculate that some fraction of the rainfall currently handled by the large-scale routine may be more properly processed by a MCS parameterization.

3.5 Summary and Conclusion

I have shown that the fraction of large-scale rainfall in the tropics is strongly correlated with several aspects of global climate model behavior, including the rainfall response to CO_2 forcing and tropical circulation strength, but that these correlations are complex, running in different directions depending on model details. In light of the CCSM3 experiments described in

Chapter 2, it is especially interesting that increasing f_{LS} is associated with a weakening Hadley circulation in the CAM3.1 ensemble, because CCSM3 includes CAM3.1 as its atmospheric model. This chapter's findings hence corroborate the novel state Jackson et al. [44] observed in CCSM3.

These initial findings highlight additional issues worthy of further consideration, including the need for more information about the vertical distribution of large-scale condensation in climate models. A direct diagnostic for convective and large-scale condensation would allow for more detailed analysis of the sources of rainfall in models, which would in turn allow for both greater understanding of the effects of model rainfall partitioning and better comparison between observations and model behavior.

Furthermore, the full climatic response to CO_2 forcing will include ocean dynamics. The effects of SST anomalies on rainfall anomalies could not be addressed within the context of the CAM SMEs, but the CMIP5 results suggest they may be important. The importance of SST anomalies to rainfall responses has been explored [125], although not with a focus on partitioning between convective and large-scale rain. Additionally, the applicability of the modified Cess experiment design, with fixed SSTs, to this particular research question is uncertain. More study is necessary to determine whether the CAM5.3 experiments, initially intended to study cloud responses to global warming, can be justifiably extended to this analysis.

It is also noteworthy that CAM3.1 and CAM5.3 contain different dynamical cores. It is reasonable to expect that the choice of dynamic core will

affect moisture transport in the tropics. Hence the differences in model behavior I have identified could be partially attributable to choice of dynamical core. This could be tested through using, for example, the CAM3.1 dynamical core with the CAM5.3 physics, a type of experiment I have not carried out.

Another question that may be profitably pursued is whether multiple equilibria exist as f_{LS} changes. As noted above, CAM3.1 ensemble experiments at the high end of the f_{LS} distribution exhibit nonlinear behavior in both large-scale and shallow rainfall suggestive of a threshold crossing. Such behavior illustrates the complexity of the handoff from convective to other types of rain, and further study may provide insight into new types of model behavior and perhaps suggest tropical mechanisms for abrupt climate change.

Finally, because slight changes in f_{LS} can have dramatic effects on the modeled precipitation response to global warming, there is a need to study in greater detail whether this fraction is hitting the appropriate target and what the appropriate target is. The few studies that have investigated this ratio, for example Yang et al. [126], have typically assumed modeled convective and large-scale rain correspond to observed convective and stratiform rainfall, as described for instance by Schumacher and Houze [92] based on TRMM data, but the relationship is likely more complicated. More study is needed to assess how the different types of model rainfall correspond to different types of real-world precipitation, because I have found that relatively small differences in the location and type of rain that occurs in the tropics can have profound impacts on the structure of a model's response to CO_2 forcing.

Chapter 4

Sea Surface Temperature-Forced Abrupt Transitions in a Single-Column Model with Weak Temperature Gradient Approximation

4.1 Introduction

As discussed in Chapter 2, there are theoretical reasons to investigate the tropics as a potential source for abrupt climate change. Furthermore, experiments by Jackson et al. with the Community Climate System Model, version 3 (CCSM3), described in Section 2.5, suggest the possibility that rapid, large-scale, low-level convergence of sensible and latent heat in the western Pacific "warm pool" region may have triggered the abrupt change observed within that model [44]. That abrupt transition was associated with a sudden increase in the fraction of tropical large-scale rainfall, and it led to very different circulatory and energy-transport patterns throughout the tropics. In Chapter 3, among other things, I established that different ratios of tropical large-scale and convective rainfall within two global atmospheric model ensembles are associated with very different tropical circulation and energy-transport characteristics. However, to test the hypothetical trigger for this abrupt change, it is useful to recognize that the global model is built from many individual columns, and to operate on the assumption that the behavior observed within

the coupled model must be traceable to the column physics. Hence, rather than devising a means of repeatedly applying this particular forcing to a computationally expensive and more physically complicated global model, one can take a less expensive and more idealized approach by applying an appropriate forcing to a single atmospheric column equipped with physics similar to that of the full GCM.

In this chapter, I find that under a simple forcing, namely a continuous increase in sea surface temperature (SST) intended to mimic low-level convergence of sensible and latent heat, a single-column model (SCM) using physics parameterizations from the National Center for Atmospheric Research (NCAR) Community Atmosphere Model (CAM) responds by abruptly transitioning to new configurations, with important consequences for precipitation including an increase in the fraction of large-scale rain. These SCM experiments also show hysteresis upon reversing the forcing, indicating the existence of multiple equilibria. Among other features, these multiple equilibria show different relative amounts of convective and large-scale rainfall. These transitions appear to be a robust feature of the CAM single-column physics as long as the weak temperature gradient (WTG) approximation is implemented in the columns, making the transitions of interest in the tropics (see Section 2.3.2).

While the SCM deployed in this study shows rich behavior not all of which is yet fully understood, I propose a simple conceptual model to describe the transitions observed in a typical experiment. With the WTG approximation active in the column, delicate balances establishes themselves between the

various temperature and moisture forcings, differently but not independently for the upper and lower column. Increasing the SST strains these balances, the most critical of which appears to be the evaporative cooling in the lower column. As this cooling fails, heat builds up in the lower column until the deep and shallow convective routines respond, extending their reach higher into the free troposphere and pushing the upper-column temperatures higher. This resets the column balance with greater intensities of rainfall, but a proportionally greater increase in large-scale rain from the upper troposphere.

4.2 Background

As described in Section 2.3, a single-column model (SCM) is a one-dimensional atmospheric model often used to study general circulation (GCM) model physics in a simplified, less computationally expensive setting. A SCM typically settles into a quasi-stationary state behavior based on a balance between radiative heating and parameterized convection and hence sometimes called a radiative-convective equilibrium (RCE) model. A single-column RCE model can usually be set up to run with radiative forcing consistent with any latitude and can be run with any type of surface at its base (land surfaces of different types, ocean, or ice). However, because SCMs are isolated from the rest of the climate system, they generally do not conserve mass, energy, or momentum, and furthermore they do not account for large-scale atmospheric dynamics. The lack of large-scale dynamics limits the usefulness of a RCE SCM in modeling a particular region; hence Sobel and Bretherton developed

the WTG approximation as a means of accounting for or "parameterizing" the tropical large-scale dynamics in the SCM setting [99]. The WTG approximation is intended to stabilize temperatures in the free troposphere, consistent with theory and observations in the deep tropics (Section 2.3.2).

Abrupt transitions are predicated upon the existence of multiple equilibria between which a physical system can move, whether through stochastic forcing or through a gradual change in the system parameters eventually causing a threshold to be crossed (see Section 2.4.1). While multiple equilibria have been found in various types of idealized climate models (for a number of references, consider [6]), including SCMs (e.g., [86]), most interesting for present purposes are those found by Sobel et al. [98] and Sessions et al. [95]. Discussed in greater detail above in Chapter 2, Sobel et al. [98] and Sessions et al. [95] both document rainy- and dry-state multiple equilibria in, respectively, a SCM and a high-resolution cloud-resolving regional model using the WTG approximation. In Sobel et al. [98] in particular, these equilibria are obtained by varying the rate at which the column or region is moistened—if moistened slowly enough, an initially dry column can persist without precipitation even when brought to a moisture profile consistent with precipitation if initially or more quickly moistened. Sobel et al. [98] attribute the existence of these multiple equilibria to the interplay between parameterized convection and the large-scale motion parameterized by the WTG approximation. This is intriguing given the significant consequences this interplay was shown to have for the tropical climate in the previous chapter. In this chapter, I find this interplay

to be important as well in determining the fraction of large-scale rain.

4.3 Experimental Setup

The SCM used in this study is the Weather Research and Forecasting (WRF) model version 3.5, compiled in single-column mode and modified by Wang and Sobel [113] to implement the WTG approximation. Rather than being wedded to specific parameterization schemes for radiation, microphysics, and so on as a typical GCM would be, the more versatile WRF model can be run with a variety of physical parameterizations; this "menu" of physics options is one reason I chose to employ WRF for this study, since I can ultimately test any findings' sensitivity to the chosen parameterization schemes. However, because the immediate concern is to understand how low-level convergence can affect the tropics in a global model similar to CCSM3 described in Chapter 2, in this chapter I describe WRF-model experiments using the Community Atmosphere Model (CAM) physics parameterizations, including for radiation, microphysics, deep and shallow convection, and boundary layer processes. [It is important to note that in the available version of WRF incorporating the WTG approximation, some of the CAM physics parameterizations have been updated from those in CCSM3. A complete description of the WRF model version 3.5 can be found on the University Corporation for Atmospheric Research (UCAR) website.[1]] I note here an interesting observation, not explored in detail in this thesis: the abrupt transitions documented below do not occur

[1] `http://www2.mmm.ucar.edu/wrf/users/wrfv3.5/wrf_model.html`.

in the WRF model—even under the WTG approximation—unless the cloud microphysics scheme is set to yield fractional cloud amounts. Certain configurations of WRF assign values of zero or one only for cloud fraction, presumably because WRF is often used for high-resolution modeling wherein grid cells are small enough to be either cloudy or not.

In testing this chapter's results' sensitivity to various model settings, a range of horizontal and vertical resolutions were ultimately used, but the standard SCM setup was for a 100-km horizontal resolution (intentionally similar to that of a typical GCM) and 50 vertical levels up to a height of 20 km. Consistent with WRF model guidelines, the time step was set to 5 minutes, with the model state saved every 3 hours.

For radiation purposes, I set the column at a latitude of zero degrees. Because cloud-radiation feedbacks can complicate the interaction between convection and large-scale advection (which the WTG approximation is usually employed to study), WTG experiments often make use of prescribed radiative cooling, such that the column cools via emission of longwave radiation at a rate matching tropical observations. The WRF model as modified by Wang and Sobel [113] includes this option of idealized cooling in the troposphere (they use a rate of -1.5 K/day). Because I am interested in how the standard CAM physics parameterizations behave under SST forcing, I use the realistic CAM radiation scheme in my primary experiments, though I have tested the forcing under prescribed radiation and comment briefly on those results below. As Wang and Sobel [113] note, ice clouds in the upper troposphere can block

outgoing radiation in a realistic tropical setting, an effect they do not account for but which will be important in this study.

In this chapter, I again use the fraction of large-scale rain generated by the model as a basic diagnostic. Like a typical global atmospheric model, the WRF model generates both convective and large-scale rainfall (the latter is usually called "non-convective" rain in the WRF context). In Chapter 3, $f_{\rm LS}$ was defined as the tropical (30°S-30°N) mean large-scale rainfall rate divided by the tropical mean total rainfall rate (Eq. 3.1), where the convective rain rate P_C included any shallow convective rainfall. Since in this chapter I am using a simpler one-dimensional model, and because that model does not automatically sum deep and shallow convective rain, $f_{\rm LS}$ will hereafter be defined as

$$f_{\rm LS} \equiv \frac{P_{\rm LS}}{P_{\rm LS} + P_{\rm C}}, \tag{4.1}$$

where $P_{\rm LS}$ and $P_{\rm C}$ are the SCM large-scale and total convective rainfall rates respectively, where it will be understood that total convective rain rate is the sum of deep ($P_{\rm D}$) and shallow ($P_{\rm SH}$) convective rain rates: $P_{\rm C} \equiv P_{\rm D} + P_{\rm SH}$.

The equations governing the evolution of potential temperature θ and the water vapor mixing ratio q in the WRF SCM with the WTG approximation are

$$\frac{\partial \theta}{\partial t} = W + Q_r^\theta + Q_c^\theta + Q_s^\theta + Q_m^\theta + Q_b^\theta, \tag{4.2}$$

$$\frac{\partial q}{\partial t} = -\omega \frac{\partial q}{\partial p} + Q_c^q + Q_s^q + Q_m^q + Q_b^q, \tag{4.3}$$

where all variables are functions of time t and height z (or pressure p), and W in (4.2) represents the WTG Newtonian relaxation (see Section 2.3.2.2) back to the RCE "background" profile θ_{BG},

$$W = -\frac{\theta - \theta_{\mathrm{BG}}(z)}{\tau} = -\omega \frac{\partial \theta}{\partial p}. \tag{4.4}$$

As with the column resolution, a range of WTG relaxation time scales were tested, but the primary experiments were carried out with $\tau = 180$ min. The remaining forcing terms in (4.2) and (4.3) are from radiation (subscript r), the deep convective parameterization (c), the shallow convective parameterization (s), cloud microphysics (m), and the boundary layer parameterization (b).[2] Eq. 4.4 allows the program to solve for the vertical pressure velocity ω, which is then used to evaluate the term $-\omega \dfrac{\partial q}{\partial p}$ in (4.3).

As discussed in Section 2.3.2.1, it is possible to implement the WTG approximation such that the WTG term W exactly cancels the other forcing terms and the change in temperature is zero. Here, because the WTG relaxation term is not constrained to exactly balance the diabatic forcing terms, the potential temperature at a given height or pressure level will depart from the background value in proportion to the total diabatic forcing at that level. For example, if the sum of diabatic forcings at a given height is $\sum Q = 0.0045$ K/s, the background potential temperature at that height is $\theta_{\mathrm{BG}} = 324$ K, and the WTG timescale is $\tau = 180$ s, then the quasi-stationary state temperature

[2] As a practical matter, within the WRF code, the WTG forcing W in (4.2) is combined with the boundary layer forcing Q_b^θ, but they can be separated again later for analysis.

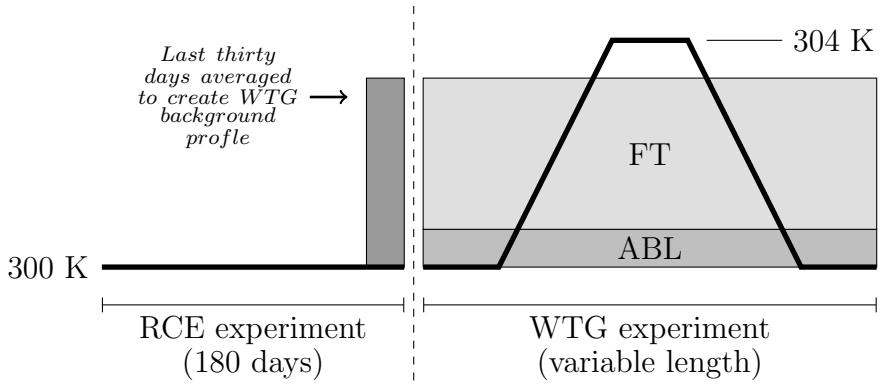

Figure 4.1: Basic design for the SCM experiments, where the dark line indicates SST, ABL stands for atmospheric boundary layer, and FT stands for free troposphere. The WTG approximation counters the diabatic heating in the free troposphere, but not in the boundary layer. The length of the WTG experiments depends on the rate of temperature change.

θ_{S} at that height will be

$$\sum Q = \frac{\theta_{\mathrm{S}} - \theta_{\mathrm{BG}}}{\tau} \quad \Longrightarrow \quad \theta_{\mathrm{S}} = \theta_{\mathrm{BG}} + \tau \sum Q \approx 324.8 \text{ K}.$$

Hence if $\sum Q$ were to abruptly increase at a given height, θ_{S} at that height would abruptly increase as well, despite the WTG relaxation scheme. A further complication arises from the fact, noted in Section 2.3.2, that the WTG approximation does not everywhere counter the diabatic heating, but only in the free troposphere—defined throughout this chapter as levels with pressure below 850 mb. Below the free troposphere in the boundary layer, the vertical velocity is reduced linearly from its value at $p = 850$ mb to zero at the ground, meaning its value is unrelated to the diabatic forcings in this region.

The SST-forcing experiments analyzed in this chapter were all done similarly (see Figure 4.1). Letting 300 K represent a typical tropical SST, the

WRF SCM is first run to RCE with this surface temperature over a period of 180 days. The final thirty days of this experiment are then averaged to extract equilibrated pressure, temperature, height, and humidity profiles, which are then used to determine the background profile θ_{BG} for the WTG routine, and then the experiments are started again at 300 K with the WTG approximation active. After an initial 90-day startup, the SST is continuously increased at some fixed rate for sufficient time to reach a specified maximum temperature (usually 304 K). The temperature is then held at the maximum value for a period of 90 days, and then continuously reduced back to 300 K where the SST is held for a final 90-day period. The experiments are all initialized with the same temperature and moisture profiles consistent with SST near 300 K.

4.4 Findings

This section is divided into four subsections. In the first, I describe general observations I have made using the WRF SCM with and without the WTG approximation, including the rainfall behavior for both cases and how the column balances the temperature and moisture forcings in each case. In the second subsection, I document the hysteresis and multiple equilibria I have found within the column under the WTG approximation with SST forcing, and in the third subsection I describe in greater detail the abrupt transitions that have been my primary focus in this project (to be further analyzed in the following Discussion section). In the final subsection, I briefly describe a unique state, characterized by $f_{\mathrm{LS}} = 1$, into which the column sometimes

abruptly transitions and from which it never seems to recover.

4.4.1 RCE vs. WTG experiments: general observations

I begin by describing the typical features of my WRF SCM RCE experiments and how these experiments are typically affected by activating the WTG approximation *without* anomalous SST forcing. Figure 4.2 displays tropical temperature and cloud profiles averaged from the last 30 days of two 180-day WRF SCM experiments, one a RCE experiment and one with the WTG approximation active. The temperature plot includes ERA-Interim reanalysis (observational) data for reference. Figure 4.2 shows several important effects of the WTG approximation: along with significantly increasing the free tropospheric moisture, it induces strong large-scale upward motion and hence condensation causing large cloud fractions in the upper column. The warming effect of this condensation above $\sim$700 mb is evident in the temperature sounding for the WTG experiment, although the highest parts of the column show cooling. While the large cloud fractions are unrealistic, they are a persistent feature of WTG experiments using the (realistic) CAM radiation parameterization.

The way the column balances the various forcing terms of (4.2) and (4.3) changes dramatically when the WTG approximation is active. In the RCE case (Figure 4.3, left side), the dominant θ-forcing balance over a large part of the column is between convective heating and radiative cooling, and (4.2) becomes $Q_r^\theta \approx Q_c^\theta$. Meanwhile, the q-forcing terms are small above roughly

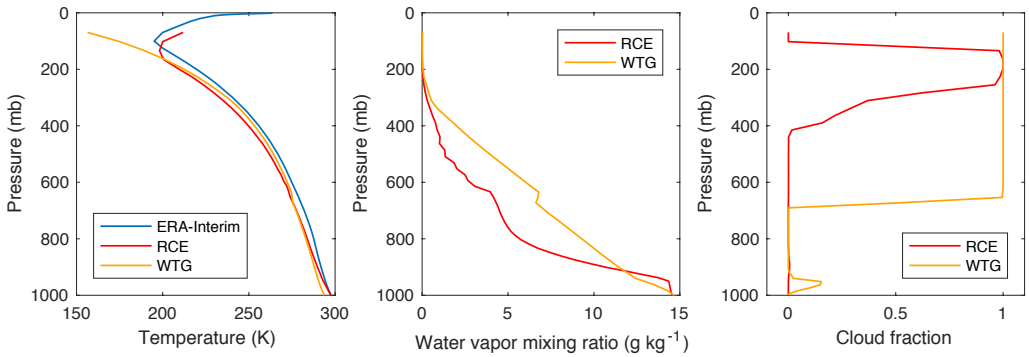

Figure 4.2: Left: Tropical soundings from ERA-Interim reanalysis (observational) data and averages over the last 30 days of two 180-day WRF SCM experiments, one a RCE experiment and one with the WTG approximation active both with fixed 300 K SST. Center: Water vapor mixing ratio profiles from the same RCE and WTG experiments. Right: Cloud fraction profiles from the same RCE and WTG experiments.

800 mb, with the convective and boundary layer schemes balancing each other below that level. With the WTG approximation active (Figure 4.3, right side), the balances are qualitatively and quantitatively different. Qualitatively, the WTG column now shows two different kinds of balance for the upper and lower troposphere. Above roughly 600 mb (the height of the cloud base), the dominant balance is between heating from condensation (microphysics) and cooling from the WTG relaxation, $W \approx Q_m^\theta$. In the lower column, the dominant balance is between convective heating and evaporative cooling (also microphysics), $Q_m^\theta \approx Q_c^\theta$, with shallow convection and the WTG relaxation playing more minor roles. Radiation plays a comparatively minor role in the WTG case, a consequence of the noted extreme cloudiness of the upper column; infrared radiation from below is absorbed at the cloud base and longwave radiative cooling dominates at the top of the column, while shortwave radiation from space is almost all absorbed by high-level clouds (Table 4.1). Because of

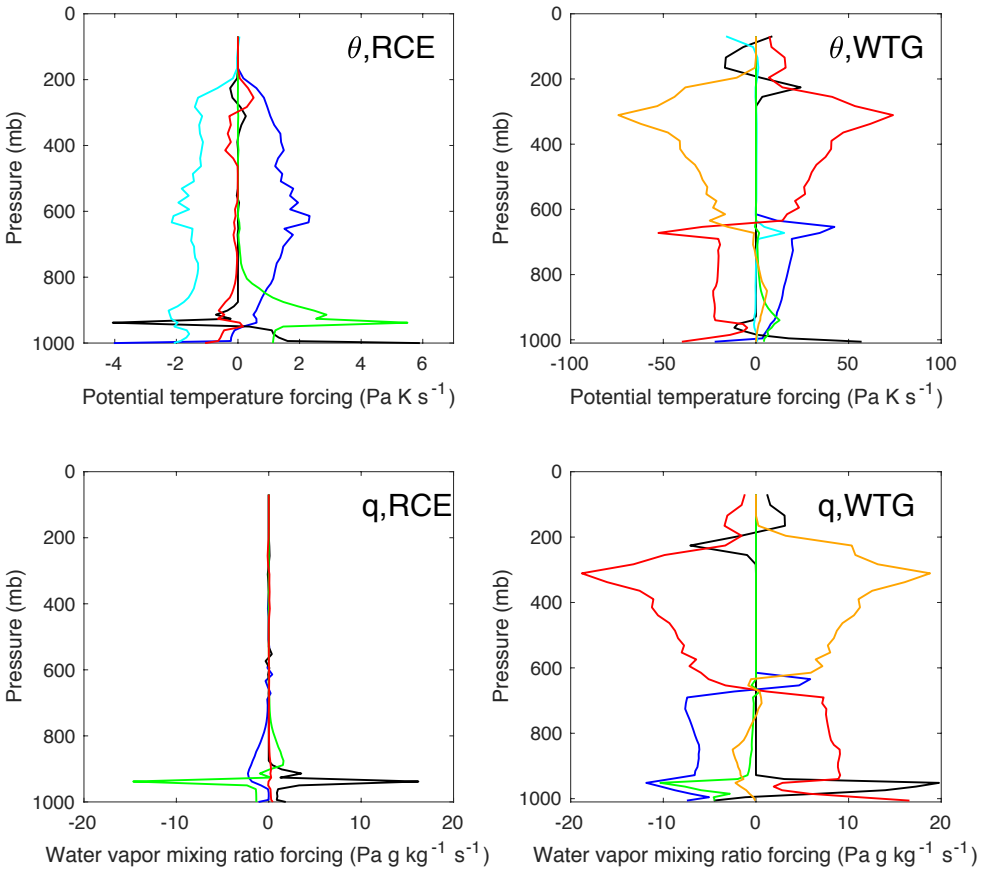

Figure 4.3: Top row: column profiles of the potential temperature (θ) forcings from Eq. 4.2 averaged over the last 30 days of RCE (left) and WTG (right) experiments, both run for 180 days with fixed SST of 300 K. The forcings are from the deep convective (blue), shallow convective (green), boundary layer (black), radiative (cyan), and microphysics (red) CAM parameterizations and the WTG relaxation scheme (orange). Bottom row: column profiles of the water vapor mixing ratio (q) forcings for the same two experiments. The WTG background profile was calibrated to a SST of 300 K.

	f_{LS}	P_{D}	P_{LS}	P_{SH}	SWD	GLW	OLR	HFX	LH
		mm/day	mm/day	mm/day	W/m^2	W/m^2	W/m^2	W/m^2	W/m^2
RCE	0.28	1.26	0.46	2.61e-4	270	358	272	8.94	99.3
WTG	0.56	9.55	12.1	2.0e-3	14.6	416	34.9	48.2	165

Table 4.1: A series of quantities averaged over the last 30 days from 180-day RCE and WTG approximation experiments without anomalous SST forcing. After f_{LS}, the three types of precipitation (deep convective P_{D}, large-scale P_{LS}, and shallow convective P_{SH}) are shown, followed by the shortwave radiation to the surface (SWD), the outgoing longwave radiation from the ground (GLW), the outgoing longwave radiation at the top of the column (OLR), and the surface sensible (HFX) and latent (LH) heat fluxes.

this, evaporation from the microphysics parameterization is the only available source of cooling in the lower column and will play a critical role in the abrupt transitions described below. As the lower panels of Figure 4.3 shows, the moisture forcings largely follow the θ-forcings in the WTG case, and indicate the much more important role played by moisture when the WTG approximation is active.

Quantitatively, the magnitudes of the forcings are much larger with the WTG approximation active, possibly a consequence of a positive heating feedback active in the upper column (discussed further in the Discussion section). Of particular interest in this connection is the fact that while mixing via deep convection is now largely restricted to $p \gtrsim 650$ mb—probably because of the reduced lapse rate and hence stabler profile near that level (see Figure 4.2)—the deep convective θ-forcing is much larger than in the RCE experiments. The greater convective heating cannot be attributed to greater CAPE, which is much larger in the RCE case, wherein the upper column is cooler. Rather, the greater deep convective θ-forcing is likely due to the greater abundance

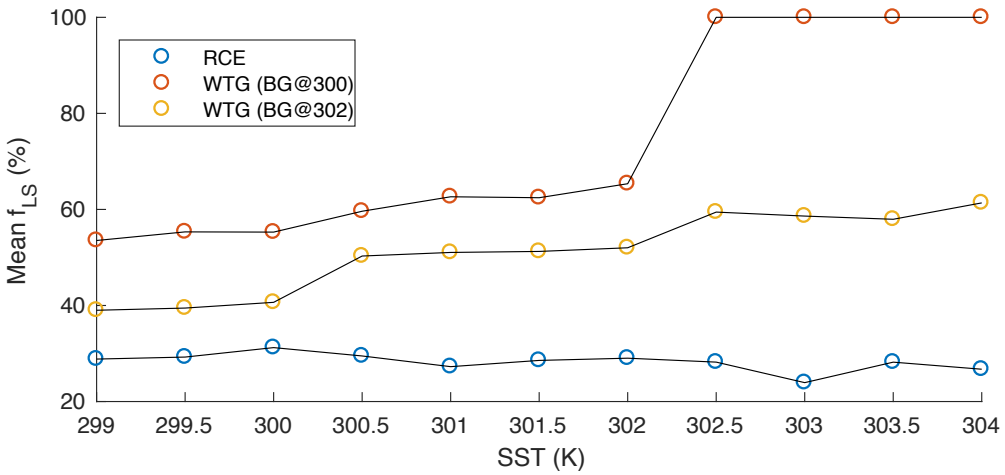

Figure 4.4: Average f_{LS} for the last 15 days of a series of 30-day RCE experiments and two series of WTG approximation experiments with different background profiles, one equilibrated to a SST of 300 K and another to a SST of 302 K. In the case of the WTG experiments using the 300 K background profile, the last four experiments demonstrate the fact that f_{LS} can go to unity in some cases.

of moisture and therefore larger heating through condensation as convective plumes rise into cooler air.

Considering the very different temperature and moisture forcing balances within the column, it is unsurprising that the RCE and WTG cases show different rainfall behavior, both in rainfall rates and type (Table 4.1). Using the CAM physics options, a typical f_{LS} for the standard WRF SCM is about 0.3, while with the WTG approximation active f_{LS} is generally larger due to the greater upper-column microphysics activity. Figure 4.4 documents how f_{LS} is affected by SST with and without the WTG approximation. Experiments show that f_{LS} drops with SST (although not monotonically) in RCE mode. With the WTG approximation active, f_{LS} is not only larger than in the RCE scenarios but also tends to *grow* with SST. However, the WTG scenario

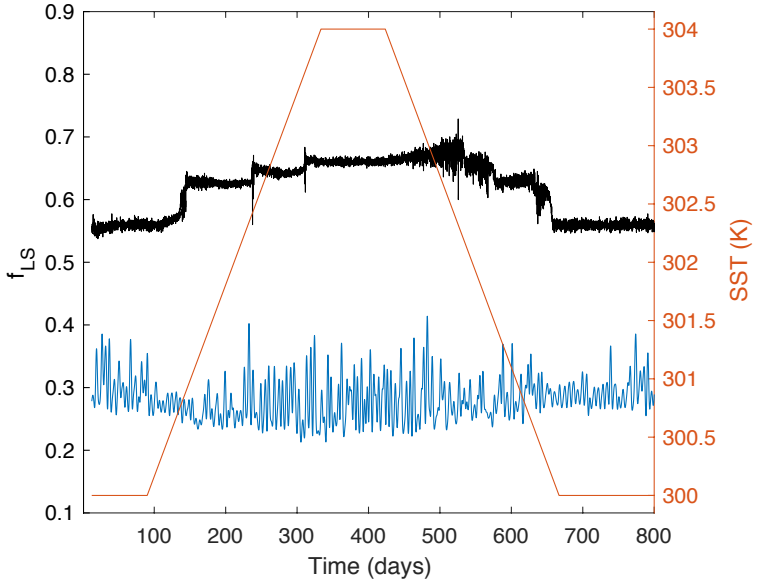

Figure 4.5: Left axis: f_{LS} for the WRF SCM over 800-day RCE (blue) and WTG (black) experiments. When running the SST-forcing experiment in a RCE configuration, the unfiltered f_{LS} has an average value of $\sim$0.28 and a standard deviation of $\sim$0.18. (The presented RCE f_{LS} data have been low-pass filtered for clarity.) Right axis: SST over the experiments.

is complicated by the fact that one must consider not only the active SST but also the SST used to generate the background temperature profile to which the free troposphere is being continuously nudged. Using a background profile appropriate for a SST of 302 K, f_{LS} grows fairly smoothly with SST. With a background profile calibrated to a SST of 300 K, the column shows more interesting behavior: for experiments carried out with higher SST, f_{LS} goes to one, an outcome mentioned above and described below.

The column response to increasing SST is very different with and without the WTG approximation active. In the RCE case, an increasing SST heats the column and leads to greater intensity of rainfall while driving the fraction

of large-scale rain down slightly (Figure 4.5). On the other hand, with the WTG approximation active, as SST increases the column begins to show stepwise abrupt transitions to larger f_{LS}, a robust outcome of such experiments (apart from the occasional $f_{\mathrm{LS}} \to 1$ behavior). Consistent with the results displayed in Figure 4.4, when the WTG approximation is inactive, f_{LS} is seen to decrease somewhat as the SST is increased and increase again as the SST is lowered. From Figure 4.4, it is apparent that when the column is run without the WTG approximation, higher SSTs result in greater convection, but with the WTG approximation active, the presence of a large-scale vertical pressure velocity ω allows the column an additional means of handling of the upward redistribution of energy.

4.4.2 Hysteresis and multiple equilibria

A close look at Figure 4.5 confirms that with the WTG approximation active, the column exhibits hysteresis: the evolution of f_{LS} as the column warms is different from its evolution as the column cools. To document the implied multiple equilibria, I carried out a modified version of the typical experiment described above, wherein I paused the SST increase/decrease at a specified "resting" SST and allowed the model to run for 30 days.

Table 4.2 and Figure 4.6 document two different SCM solutions averaged over those 30-day periods, which I call E1 and E2, for the same resting SST of 304.5 K (in this particular set of experiments, the SST was increased from 301 K to 305 K, but the qualitative behavior is similar to my standard

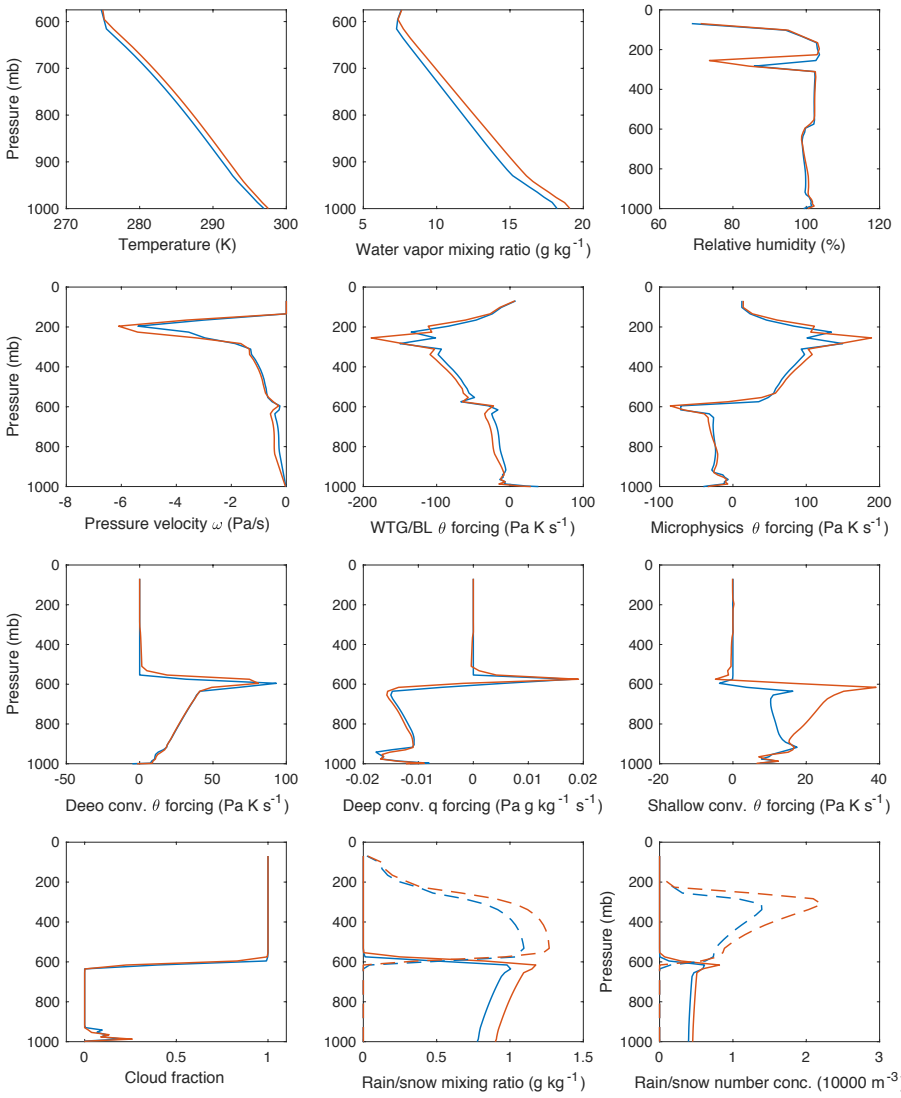

Figure 4.6: Average profiles for a number of variables for two SCM solutions at SST 304.5 K. Blue represents E1 (the equilibrium obtained during the warming phase), and red represents E2 (the cooling phase equilibrium). Forcing terms are mass-weighted in WRF, hence the units of Pa K s^{-1}. Note that the WTG forcing is combined with the boundary layer forcing here, but this quantity is dominated by the WTG forcing above the boundary layer. In the plots for rain/snow mixing ratio and number concentration, solid lines represent rain and dashed lines represent snow. See also Table 4.2.

	f_{LS}	P_{D}	P_{LS}	P_{SH}	SWD	OLR	HFX	LH
		mm/day	mm/day	mm/day	W/m^2	W/m^2	W/m^2	W/m^2
E1	0.61	42.4	66.0	0.026	12.9	39.9	67.3	267
E2	0.63	45.4	77.8	0.056	11.4	40.7	57.3	231

Table 4.2: Average values for a series of quantities for the two distinct SCM equilibria (E1 and E2) shown in Figure 4.6. After f_{LS}, the three types of precipitation (deep convective P_{D}, large-scale P_{LS}, and shallow convective P_{SH}) are shown, followed by the shortwave radiation to the surface (SWD), the outgoing longwave radiation at the top of the column (OLR), and the surface sensible (HFX) and latent (LH) heat fluxes.

300 K-to-304 K experiments). E1 is the solution obtained during the warming phase of the experiment, and E2 is obtained during the cooling phase. It is evident from Figure 4.6 that in the case of E2, the model has settled into a warmer, wetter solution with stronger vertical motion, although there is nuance in how the model achieves balance between heating and cooling in this case relative to E1. The clearest difference is in the shallow convective subroutine, where for E2 shallow convection plays a much greater role in heating the column between roughly 900-600 mb while the rate of shallow rainfall P_{SH} (while small compared to deep convective or large-scale rain) more than doubles (Table 4.2). Both convective parameterizations also reach slightly higher into the column. E2's enhanced shallow convective heating is offset between 900-650 mb by both the WTG relaxation and evaporative cooling from the microphysics scheme—it is noteworthy that the microphysics parameterization is unable to balance the lower-column heating alone. Near 600 mb, however, E2 shows a net increase in heating from shallow convection. The deep convection q-forcing shows that the E2 solution is furthermore removing more vapor from below 600 mb and depositing slightly more above.

	f_{LS}	P_{D}	P_{LS}	P_{SH}	SWD	GLW	OLR	HFX	LH
		mm/day	mm/day	mm/day	W/m^2	W/m^2	W/m^2	W/m^2	W/m^2
S1	0.56	9.58	12.2	2.1e-3	17.6	416	35.6	48.3	165
S2	0.63	14.6	24.5	5.3e-3	13.3	412	36.5	58.5	207
S3	0.64	19.5	35.4	14.8e-3	14.0	416	38.0	63.7	235
S4	0.66	23.4	45.7	31.9e-3	13.4	422	39.5	63.2	243

Table 4.3: Average values for a series of quantities for the four states from the experiment shown in Figure 4.7. After f_{LS}, the three types of precipitation (deep convective P_{D}, large-scale P_{LS}, and shallow convective P_{SH}) are shown, followed by the shortwave radiation to the surface (SWD), the outgoing longwave radiation from the ground (GLW), the outgoing longwave radiation at the top of the column (OLR), and the surface sensible (HFX) and latent (LH) heat fluxes.

Varying the rate of SST increase or decrease does not have a strong effect on the SCM's behavior. Qualitatively, it is difficult to distinguish the outcomes of experiments with different SST-forcing rates apart from their varying lengths. Quantitatively, a close look does reveal that the SSTs at which the column undergoes transitions do depend on the rate of SST increase, with faster rates of increase causing the transitions to occur, on average, at very slightly warmer temperatures. For example, when the SST is increased at 3 K yr^{-1}, the second (and most abrupt) transition occurs close to 302.3 K; when the rate is 12 K yr^{-1}, the same transition occurs closer to 302.5 K. Furthermore, varying the rate of SST increase has no discernible systematic effect on the characteristics of the two solutions at SST 304.5 K presented in Figure 4.6 and Table 4.2.

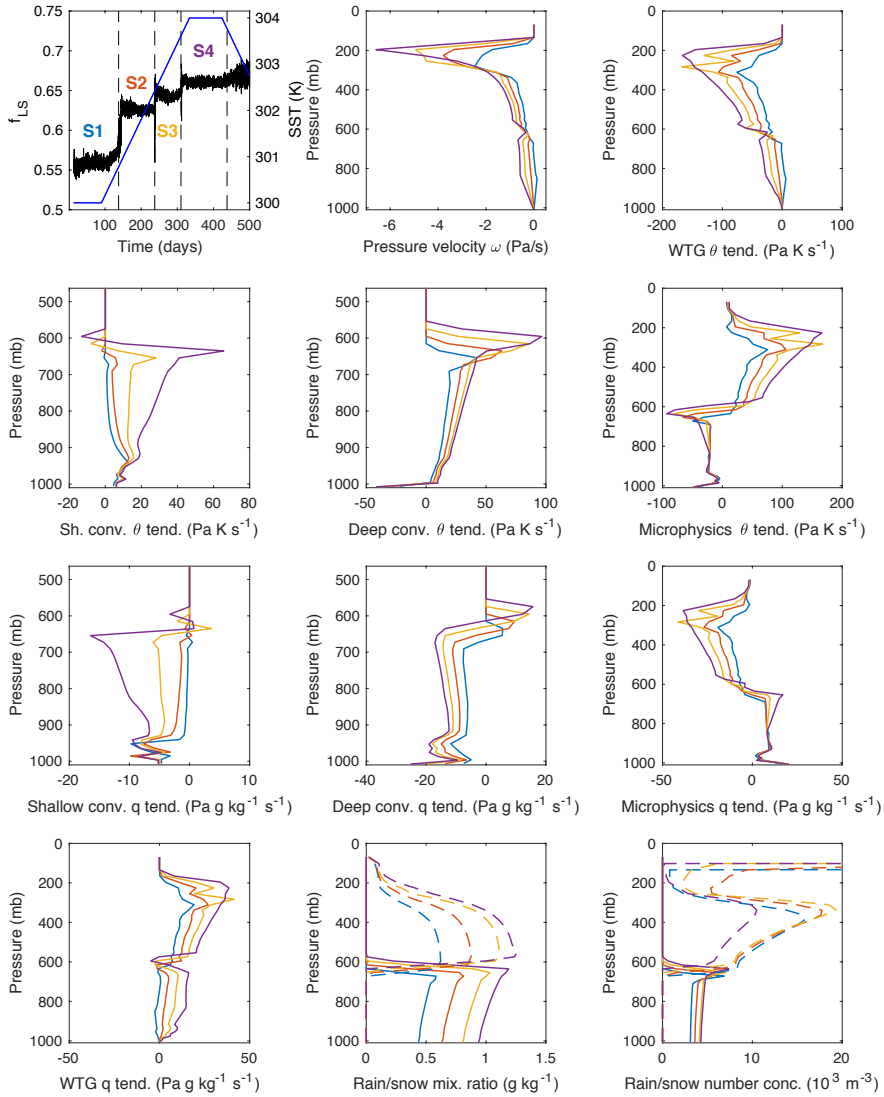

Figure 4.7: Four quasi-stationary states of the heating WRF SCM with WTG approximation. For the top left plot, the left axis shows $f_{\rm LS}$ for the WRF SCM over the first 500 days of an 800-day integration with the WTG approximation active and a background profile calibrated for 300 K SST. Four quasi-stationary states (S1, S2, etc.) are indicated. The right axis shows SST over the same integration. The remaining plots show vertical profiles for the labeled quantities, averaged over time for each of the four states (S1 blue, S2 red, S3 yellow, S4 purple). The four plots showing convective forcing profiles stop near 500 mb because they are zero above. WRF model forcings are mass-weighted, hence the units in terms of pressure. In the last two plots for rain/snow mixing ratio and number concentration, the solid lines represent rain and the dashed lines represent snow. See also Table 4.3.

4.4.3 Abrupt transitions and quasi-stationary states

The results described in this section and analyzed in the Discussion section below are taken from an RCE experiment at a SST of 300 K and a SST-forcing experiment increasing the temperature from 300 K to 304 K as illustrated in Figure 4.1, with a rate of increase of 0.5 K/month. The average f_{LS} for the last 30 days of the 180-day RCE experiment is 0.28. The WTG experiment first equilibrates with an f_{LS} of about 56.0%, but as the SST is increased, the column shows three abrupt transitions to higher f_{LS}, roughly 62.7%, 64.5%, and finally 66.1% (Figure 4.7, upper left panel). As noted, the column shows additional abrupt behavior and hysteresis as SST is decreased, but a close analysis of the cooling phase is left for future work.

Figure 4.7 and Table 4.3 show both the evolution of f_{LS} as the WRF SCM heats up and the major characteristics of the four quasi-stationary states (S1, S2, etc.) observed before/after the abrupt transitions. It is clear from the profiles of ω, the various θ- and q-forcing terms, and the rain and snow mixing ratios and number concentrations that, in general, the magnitudes of upward motion, heating, moistening, and rainfall grow as the surface temperature increases. There are, however, some features that show interesting qualitative changes as one state gives way to another. In particular—and as noted above in discussing the multiple equilibria at 304.5 K—the shallow convection profile shows the most marked change, with both the magnitude and shape of its profile changing from state to state, with progressively greater activity higher above the surface. Moreover, both the deep and shallow convective profiles

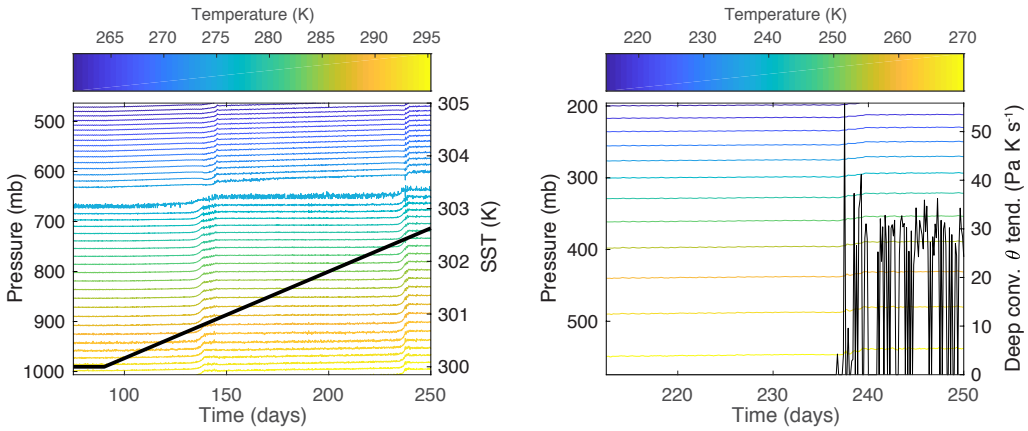

Figure 4.8: Left: A contour plot of temperature in the column, showing the first and second abrupt transitions. For reference, the SST is shown on top of the contour plot, referring to the right axis. Right: A contour plot of the upper-column temperature focusing on the second transition. On top of this contour plot, the (mass-coupled) θ-forcing due to deep convection at roughly 600 mb is shown, referring to the right axis. See also Figure 4.10.

reach higher into the column for higher SST. (Consistent with this observation, the cloud base moves one model level higher with each transition.)

Before looking closely at the abrupt transitions, it is worth noting some general features of the column evolution leading up to the transitions, evident in the left panel of Figure 4.8. As expected, temperatures near the surface begin to increase along with the SST forcing, but, for example, the temperature one level above the surface increases at only 0.15 K/month, much slower than the 0.5 K/month SST increase. (For comparison, in an identical SST-forcing experiment without the WTG approximation, the temperature one level above the surface increases at 0.46 K/month.) Also as expected, given the way the WTG approximation is designed to operate, as the height approaches $p = 850$ mb where the WTG relaxation becomes active, temperatures are more stable.

More surprising, however, is the column behavior above roughly 650 mb. Here, temperatures increase even more quickly than near the surface (e.g., at a rate of roughly 0.35 K/month at $p \approx 460$ mb, with some higher levels showing even larger warming rates). This can only be an effect of the convective parameterizations removing heat from near the surface and moisture from throughout the lower column, and depositing both near 650 mb (see Figures 4.3 and 4.7), where the large-scale advection generated by the WTG relaxation can "take over", carrying this moisture aloft into cooler air, where the microphysics generates the observed condensational heating. Moreover, convection is delivering this heat and moisture to the upper column at a growing rate—if the rate were constant, the WTG relaxation could stabilize the temperatures. This increasing rate of heat export from near the surface is probably consistent with the fact that the surface is heating so much more slowly than it would in the absence of the WTG relaxation. This general behavior causes the more stable "middle" part of the column, between roughly 900-650 mb, to grow increasingly out of sync with the regions heating above and below.

A close look at the abrupt transitions shows some features common to all. First, the forcing that most closely follows the lower-column heating is the microphysics, and within the microphysics routine it seems clear that a loss of evaporative cooling is the main driver of the rapid temperature increase at the transition. In the standard model output, this relationship is especially clear during the first transition (Figure 4.9). And while the microphysics forcing grows noisier as SST rises, making the relationship slightly less clear in

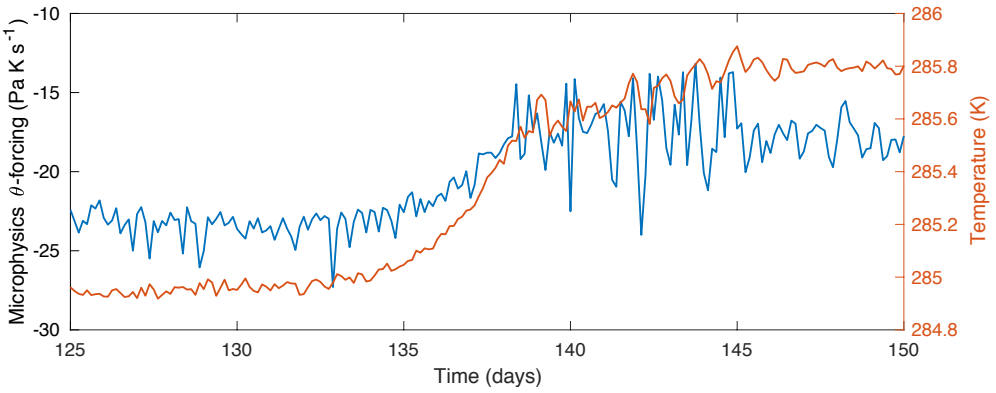

Figure 4.9: Left axis: the microphysics θ-forcing at roughly 835 mb (blue) during the first abrupt transition. Right axis: the temperature at the same level (red).

the standard output for the second and third transitions, unprocessed, high-resolution output obtained from the microphysics routine confirm the same pattern for the second and third transitions as well (not shown). As the evaporation starts to fail and temperature starts to increase, a new positive feedback develops: the WTG relaxation responds with cooling and stronger upward motion, advecting moisture upward and causing the mixing ratio and relative humidity to rapidly increase alongside temperature, despite the falling evaporation and likely exacerbating the evaporation shortfall. Moreover, the WTG relaxation plays a progressively greater cooling role in the lower column with each transition, while the microphysical cooling recovers but does not gain much ground between roughly 700-900 mb over the course of the SST forcing (see Figure 4.7). It is possible that generally high relative humidity in the lower column limits evaporative cooling, such that as the column warms the microphysics ultimately cannot provide enough cooling to balance the heating from the convective routines. Growing local relative humidity, and therefore

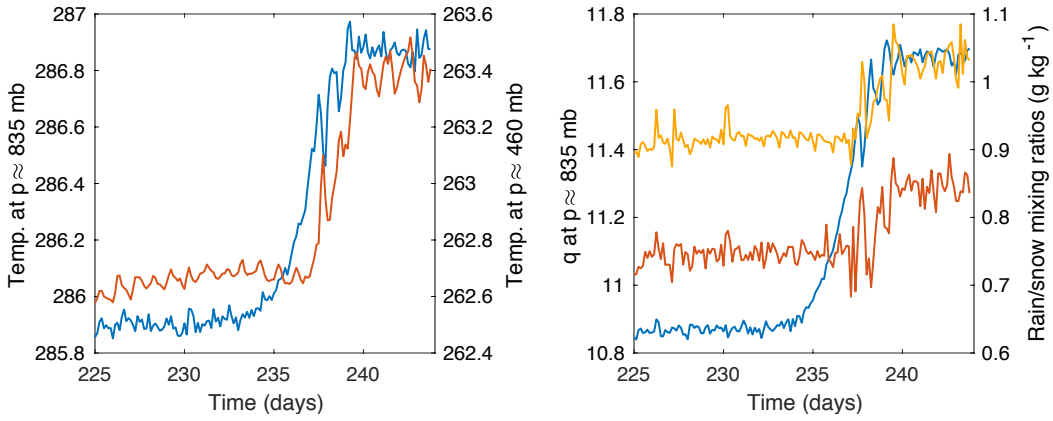

Figure 4.10: (Left panel) Left axis (blue): temperature (T) evolution at a randomly selected level from the lower part of the column ($p \approx 835$ mb). Right axis (red): temperature evolution at a randomly selected level from the upper part of the column (red, $p \approx 460$ mb). (Right panel) Left axis: water vapor mixing ratio (q) evolution at $p \approx 835$ mb (blue). Right axis: the rain (red) and snow (yellow) mixing ratios' evolution at $p \approx 835$ mb and $p \approx 460$ mb, respectively. The evolution of the latter (microphysics) variables is largely determined by the upper column.

less ability to take up additional water vapor, might even be suggested as a trigger for the transition, but the relative humidity does not increase markedly before the first transition, and is smoothly *decreasing* before the onset of the second and third transitions, most likely because the convective routines are quickly removing moisture from the lower column.

Second, the upper and lower parts of the column experience the transitions differently. Visible in the left plot of Figure 4.8 but shown more clearly in Figure 4.10, over the few days during which a transition takes place, the upper-column temperatures temporarily stabilize (or even slightly decrease) while the lower-column temperatures show a rapid but fairly smooth increase. Consistent with this, the upper-column diabatic heating and WTG relaxation also temporarily stabilize or reverse their trends. Toward the end of the rapid

temperature and moisture increase in the lower troposphere, the corresponding upper-column variables abruptly transition to new values. For clarity and simplicity, I will refer to these two types of transition behavior as "rolling" for the lower column and "snapping" for the upper column.

Third, it seems clear that the transition's transmission to the upper column and termination are closely connected to the convective parameterizations: the convective scheme's θ- and q-forcings briefly spike near the end of the lower-column "roll", just as the upper-column variables "snap" into their new quasi-stationary values (see the right panel of Figure 4.8, which shows the upper-column temperature evolution along with the abrupt increase in deep convective θ-forcing near 600 mb at the "snap"). These are among the rare occasions when the convective routine is able to penetrate above $\sim$600-650 mb, and after this burst of convection near the end of each transition, convective mixing reaches (usually one level) higher into the column than before. Aside from these spikes at the transitions, it is worth noting that the deep convective forcings grow quite linearly with SST.

Finally, while most variables follow the behavior of their corresponding part of the column (i.e. most lower-column variables show rolling behavior, while most upper-column variables show snapping behavior), some variables do not. The convective routines are one example, but the rain and snow mixing ratios (determined by the microphysics parameterization) also break the pattern, showing snapping behavior even in the lower column (Figure 4.10, right panel). This is consistent with precipitation changes initiated in the

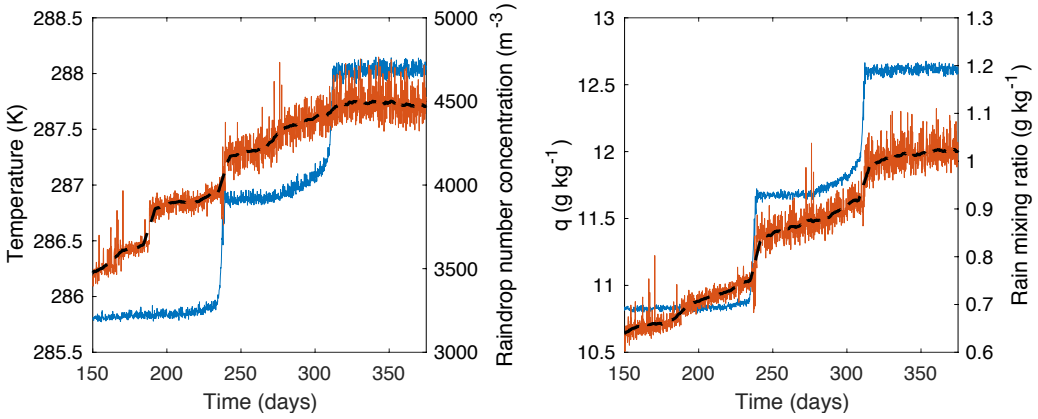

Figure 4.11: (Left panel) Left axis: temperature (T) evolution (blue). Right axis: raindrop number concentration evolution (red) with low-pass filtering shown in black. (Right panel) Left axis: water vapor mixing ratio (q) evolution (blue). Right axis: the rain water mixing ratio evolution (red) with low-pass filtering shown in black. All quantities are at $p \approx 835$ mb.

upper column subsequently becoming apparent in the lower column as the rain and snow precipitate out.

In some cases, there are sudden changes in certain variables prior to the transitions, although a causal relationship is not clear. The most intriguing of these "precursor" events involve abrupt changes in the mixing ratios and number concentrations of raindrops (lower column) and/or snowflakes (upper column). These shifts may signal threshold-crossing behaviors in the microphysics subroutine as it responds to the heating environment. Figure 4.11 gives an example of this type of precursor behavior for the first and second abrupt transitions. In the left panel, the raindrop number concentration N_r is shown against the temperature evolution; N_r clearly shifts abruptly at $t \approx 180$ days, again at the first temperature transition, and then there is another possible shift at $t \approx 275$ days before the second temperature transition. In the right

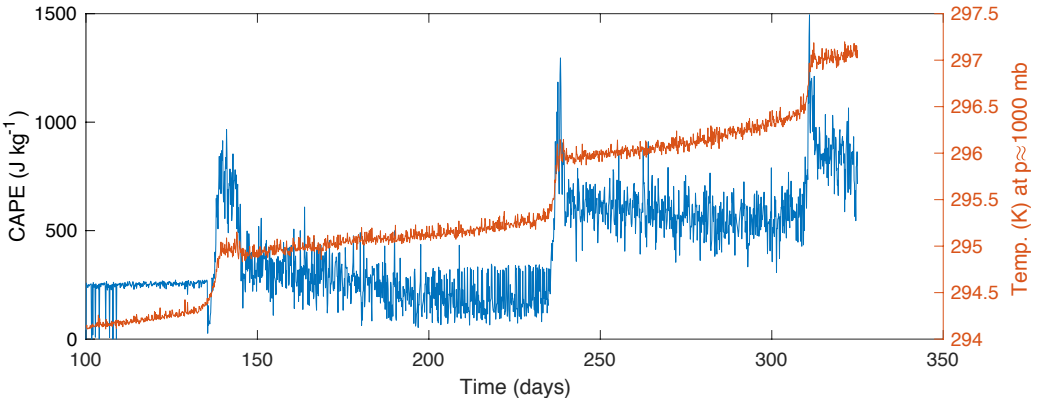

Figure 4.12: Left axis: convective available potential energy (CAPE, blue) Right axis: temperature (T) evolution near the surface (red). The CAPE stabilizes in the weeks leading up to the second and third transitions.

panel of Figure 4.11, the rain water mixing ratio q_r is shown against the water vapor mixing ratio. Again, it appears q_r shifts near $t \approx 180$ days, although a shift is less evident near $t \approx 275$ days. It must be borne in mind, however, that these plots are for one level only (around $p \approx 835$ mb) and are not representative of the entire column. The microphysics variables show rich behavior that is often difficult to interpret—no doubt a consequence of the richness of the microphysics routine, described briefly in the next section—but it is worth noting that the changes depicted in Figure 4.11 do seem to coincide with the initiation of a slow temperature increase leading up to the transitions, clearer in the second and especially third transition than in the first. This may imply correlation or causation but caution is warranted. Intriguing too is the behavior of the CAPE, which levels out as the temperatures begin this slow increase prior to the "roll" of the transitions (Figure 4.12).

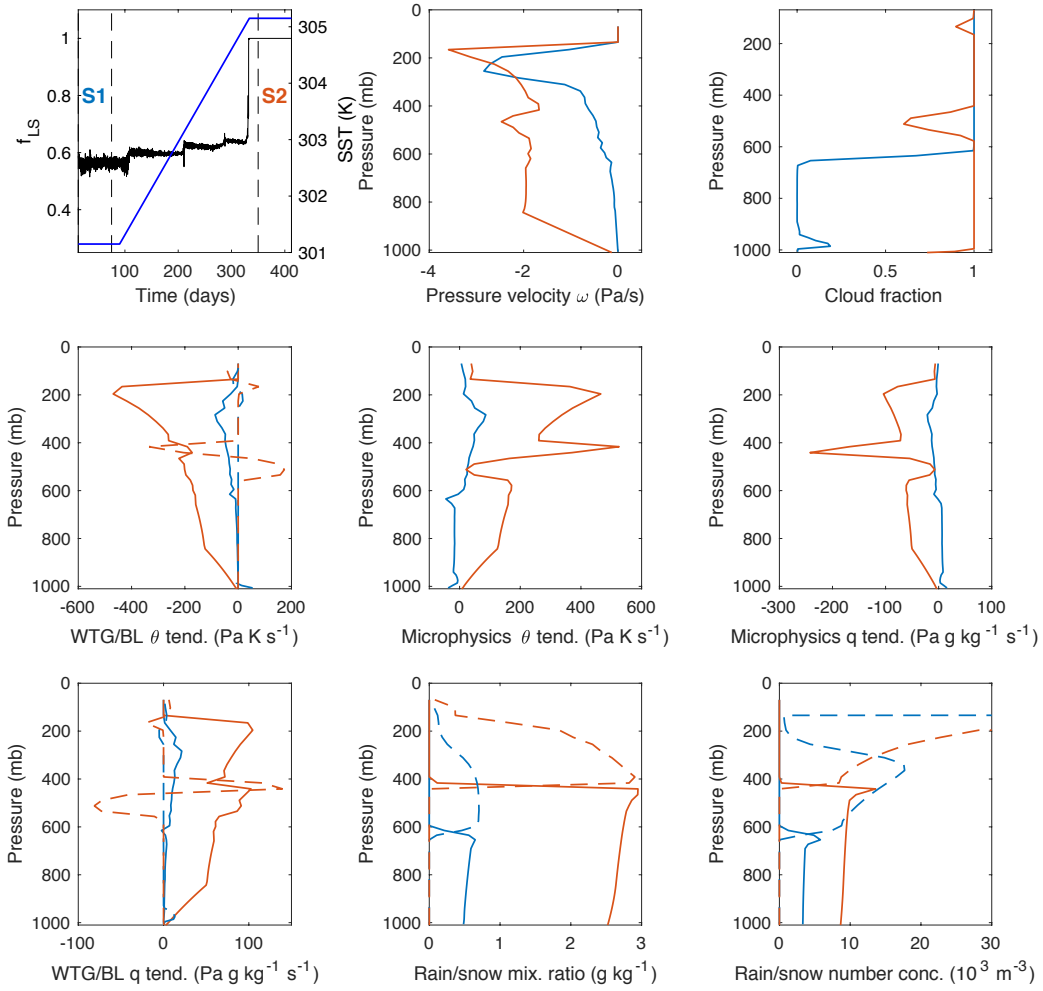

Figure 4.13: An experiment showing $f_{\rm LS} \to 1$. The left axis of the top left plot shows $f_{\rm LS}$ for the WRF SCM over the heating phase of an 800-day integration with the WTG approximation active and a background profile calibrated for 301.15 K SST, with SST forcing from 301.15 K (28°C) to 305.15 K. A typical quasi-stationary state (S1, blue) and the $f_{\rm LS} = 1$ state (S2, red) are indicated. The right axis shows SST for the integration. The remaining plots show vertical profiles for the labeled quantities, averaged over time for each of the two states. In the WTG/BL panels, solid lines show the WTG relaxation forcings and dashed lines show the boundary layer forcings. In the plots for rain/snow mixing ratio and number concentration, solid lines represent rain and the dashed lines represent snow. See also Table 4.4.

	f_{LS}	P_{D}	P_{LS}	P_{SH}	SWD	GLW	OLR	HFX	LH
		mm/day	mm/day	mm/day	W/m^2	W/m^2	W/m^2	W/m^2	W/m^2
S1	0.56	12.2	15.7	4.70e-3	19.2	423	42.8	41.1	152
S2	1.0	0	249	0	11.6	474	72.3	0.02	1.84

Table 4.4: Average values for various quantities for the S1 and S2 states from the $f_{\mathrm{LS}} \to 1$ experiment shown in Figure 4.13. After f_{LS}, the three types of precipitation (deep convective P_{D}, large-scale P_{LS}, and shallow convective P_{SH}) are shown, followed by the shortwave radiation to the surface (SWD), the outgoing longwave radiation from the ground (GLW), the outgoing longwave radiation at the top of the column (OLR), and the surface sensible (HFX) and latent (LH) heat fluxes.

4.4.4 The $f_{\mathrm{LS}} \to 1$ case

Under certain conditions, a complete analysis of which is left for future work, the WRF SCM under the WTG approximation can transition into a state with $f_{\mathrm{LS}} = 1$. This state is unique in that the convective parameterizations shut down completely, the column becomes cloudy almost top to bottom, the θ- and q-forcings grow to even larger magnitudes, and the lower-column pressure velocity ω becomes much larger than usual. Furthermore, once the column enters this state, it seems permanent; the column seems never to recover from the $f_{\mathrm{LS}} \to 1$ transition even when the SST is decreased again.

Figure 4.13 and Table 4.4 give average values for a number of variables for both a typical quasi-stationary state (S1) and the $f_{\mathrm{LS}} = 1$ state (S2) in an experiment showing the $f_{\mathrm{LS}} \to 1$ transition just before the end of the SST increase. This experiment is identical to the experiment analyzed in Section 4.4.3, except that the SST forcing is from 301.15 K (28°C) to 305.15 K and the WTG background profile is calibrated to SST 301.15 K.

Convective profiles are omitted from Figure 4.13 since they are zero

for the $f_{\rm LS} = 1$ state. Figure 4.13 also shows both the WTG relaxation forcings and the pure boundary layer forcings. Summed together, the cooling from the WTG and boundary layer θ- and q-forcings balance the heating from microphysics. It is interesting that the boundary layer scheme, which is also referred to as the moist turbulence scheme, is active higher in the column than usual, where it apparently plays a role in mixing heat and moisture across the critical cloud base layer, similar in some ways to the function previously performed by the convective parameterizations.

As is evident from Table 4.4, convective rainfall not only ceases for $f_{\rm LS} = 1$, but the microphysics forcings and associated large-scale rainfall show dramatic increases, with forcings and rainfall rates an order of magnitude larger than those obtained for lower $f_{\rm LS}$, and as much as two or three orders of magnitude larger than the forcings and rates for a typical RCE experiment (see Figure 4.3). Moreover, the balance of forcings in the column changes qualitatively again, with the WTG relaxation and boundary layer scheme now working together to balance microphysical heating (via melting or condensation) over the full depth of the column. Evaporation has now failed completely to cool the lower column and has switched over to warming.

4.5 Discussion

It seems clear that lower-column evaporative cooling plays the dominant role both in initiating the abrupt transitions and keeping the column from falling into the $f_{\rm LS} \to 1$ state. To better understand this, however, it

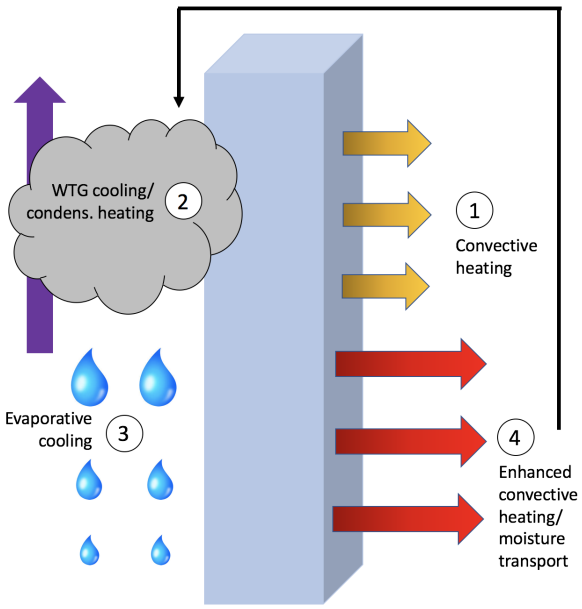

Figure 4.14: An illustration of the θ-forcing balances within the WRF SCM with WTG approximation, and the order in which they appear to be established in the first few time steps. The $4 \rightarrow 2$ arrow signifies the convective parameterizations delivering moisture across the cloud base into the upper troposphere.

is worth considering the overall balance of the column when the WTG approximation is active. I noted above that the magnitudes of the WRF SCM θ-forcings are much larger in the WTG case than in the RCE case. This leads to a consideration of how the column stabilizes itself at the beginning of the WTG experiments, a close look at which suggests a positive heating feedback active (at first) in the upper column which is ultimately balanced by a series of diabatic forcings (Figure 4.14). Because heating in the upper column (whether coming from the convective or microphysics parameterizations) can only be balanced here by radiative cooling or the WTG relaxation, but more efficiently by the latter, heating at high levels generates an upward large-scale

motion by (4.4), which then generates more heating due to condensation or freezing as water vapor is lifted into cooler air. The resulting cloudiness also blocks part of the outgoing infrared radiation from lower in the column, causing heating near the cloud base and causing the feedback to reach lower into the column. This feedback, which begins near the top of the column, causes upward motion lower and lower in the column, until the falling precipitation reaches levels at which its melting or evaporation generates enough cooling to stop the feedback mechanism from reaching even lower into the column. Meanwhile, the large-scale rain resulting from this upper-column activity generates proportionally greater evaporative cooling below as the large-scale rain falls through the lower column, with this cooling balanced in turn by enhanced heating from the convective parameterizations. Finally, enhanced convection (especially coming from the shallow scheme) is able to deliver moisture and heat from the lower column to the layers around the cloud base, feeding the upper-column microphysics routine and thus allowing the balances depicted in Figure 4.14 to hold for an overall warmer column.

Some temperature forcings can respond quickly and without strong limits to temperature changes, while other forcings are limited such that the column equilibrium could become strained. The WTG relaxation simply adds or removes heat from the system (while inducing a vertical velocity), and has no inherent limitations. The shallow convective parameterization too is unlimited in its vertical reach and precipitation rate; indeed, it can represent deep convection on its own if no deep convective parameterization is employed [76].

It seems likely that this ability of the shallow scheme to work well beyond its "shallow" capacity is responsible for the proportionally greater increase in its heating role as SST increases (Figure 4.7). On the other hand, the deep convection scheme is limited by the CAPE-consumption time scale τ_c; it consumes CAPE at a rate proportional to the amount of CAPE: $\frac{d(\mathrm{CAPE})}{dt} = -\frac{\mathrm{CAPE}}{\tau_c}$ [129]. Upper-column microphysical heating is limited by the availability of moisture there—if the convective routines and WTG lifting are unable to deliver enough moisture, the condensational heating will not be maintained.

Similarly, lower-column evaporation is limited by the abundance of rainfall coming from above and by the local relative humidity. Because evaporative cooling provided to the lower column by the microphysics parameterization appears to be the first element of the Figure 4.14 balance to fail as the system transitions to each new state—and because it most closely follows the heating of the lower column—I attribute the transitions to nonlinearities within the microphysics routine.

The CAM microphysics routine is due to Hugh Morrison and various collaborators including Andrew Gettelman [65, 66], and is based on equations for the number concentration N_r of rain droplets (or N_{sn} for snowflakes) and the mixing ratio q_r for rainwater (or q_{sn} for snow):

$$\frac{\partial N_r}{\partial t} = \frac{1}{\rho}\frac{\partial}{\partial z}\left(\rho\, V_N N_r\right) + \sum_i \left(\frac{\partial N_r}{\partial t}\right)_i \tag{4.5}$$

$$\frac{\partial q_r}{\partial t} = \frac{1}{\rho}\frac{\partial}{\partial z}\left(\rho\, V_q\, q_r\right) + \sum_i \left(\frac{\partial q_r}{\partial t}\right)_i, \tag{4.6}$$

where V_N and V_q are the terminal fall speeds for rain weighted by number and mass respectively, and i indexes a number of terms due to various microphysical processes (condensation, melting, droplet growth by accretion or self-interaction, etc.), among which is evaporation of falling rain. Evaporation of rain within the CAM microphysics, of primary interest here, is given by

$$P_E = \frac{2\pi N_0 (S-1)\left[0.78\Lambda^{-2} + 0.32 S_C^{1/3} a^{1/2} \nu^{-1/2} \Gamma(\frac{b+5}{2}) \Lambda^{-(b+5)/2}\right]}{\frac{L^2}{K R_v T^2} + \frac{R_v T}{e_s D_v}}. \qquad (4.7)$$

The derivation of (4.7) is given in Appendix B, but roughly, the numerator is related to the amount of evaporation while the terms in the denominator account for its thermal and diffusive effects: N_0 and Λ are spectral parameters determining the raindrop size distribution [these are functions of N_r and q_r from (4.5) and (4.6)]; a and b are empirically determined parameters giving the raindrop terminal fall velocity; $S \equiv e/e_s$ is the ratio of ambient vapor pressure to saturation vapor pressure; ν is the kinematic viscosity; K and D_v are the thermal conductivity[3] and mass diffusivity of water vapor in air respectively; and $S_C \equiv \nu/D_v$ is the Schmidt number. The temperature- and moisture-dependence of (4.7) is quite complicated, with most of the variables determined by temperature and/or moisture.

As mentioned above, raw, high-resolution output taken from this equation during the WTG experiment confirms that P_E diminishes in correlation

[3]The thermal conductivity can be written as $K = c_p \rho \kappa$, where κ is the thermal diffusivity. In the WRF code, κ is replaced by the mass diffusivity D_v, which seems to be acceptable for air-water vapor systems, which have a Lewis number (Le $\equiv \kappa/D_v$) approximately one.

with each lower-column rolling temperature increase. Moreover, analysis of the individual terms of (4.7) indicates that the numerator is stable during the onset of the transitions, an expected result considering that the raindrop mixing ratio q_r and number density N_r—related to terms in the numerator—transition with the upper-column "snap" rather than with the lower-column "roll." The saturation vapor pressure and thermal and diffusive terms, however, show rolling behavior alongside the temperature change, indicating that the local environment plays the stronger role in initiating the transition.

In this context, the $f_{\mathrm{LS}} \to 1$ behavior would seem to be a "runaway" case of the positive WTG heating feedback. If the only way in which the column can balance heating is via the WTG relaxation, this will generate additional heating above via lifting (and condensation) of moisture, and heating below via absorption of infrared radiation at the newly generated cloud base. Indeed, a preliminary look at the θ-forcings in several experiments showing the $f_{\mathrm{LS}} \to 1$ transition reveals that near the transition, there is a point at which the evaporative cooling from the microphysics routine switches over into condensational heating. This means the deep and shallow convective routines and the microphysics parameterization are all working to heat the column at these levels; at this point, the only way the column can balance this heating is via radiative cooling or the WTG relaxation, the latter of which is again the more efficient. Hence the lower part of the column now experiences the WTG feedback, which spreads over the lower column leading quickly to $f_{\mathrm{LS}} \to 1$. Presumably, convection shuts down because the WTG-induced upward wind

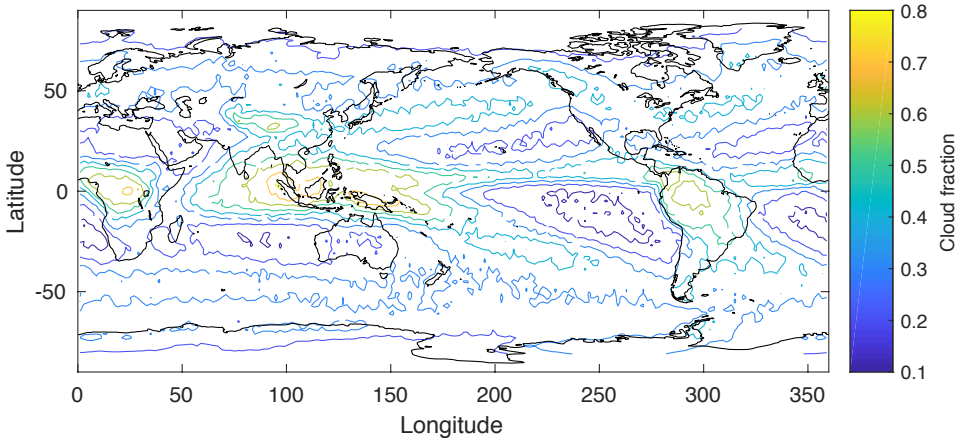

Figure 4.15: CALIPSO observational cloud fraction data averaged for $p < 440$ mb.

is able to stabilize the column by itself.

The extreme cloudiness shown by the WTG column, a consequence of using the realistic CAM radiation parameterization, is problematic. While cloud fractions can be fairly large in some areas of the tropics at high levels—for example, CALIPSO[4] 2006-2014 data shows cloud fractions as high as ∼0.8 for $p < 440$ mb in the area of the Maritime Continent (Figure 4.15)—the 100% cloud cover consistently observed over the upper half of the WRF SCM column with the WTG approximation is unrealistic. Prescribed radiative cooling seems to alleviate this problem (at least in the absence of anomalous SST forcing), keeping cloud fractions similar to their RCE values (which are also closer to observations), but this option is designed to isolate and study the interaction between convection and large-scale vertical advection. Since I am pursuing a different question involving the realistic case including cloud-radiation inter-

[4] `https://climserv.ipsl.polytechnique.fr/cfmip-obs/`.

actions, prescribed radiation is not an optimal solution. Furthermore, even with prescribed convection, SST forcing again generates the unrealistic 100% cloud fractions in the upper column.

As noted in the introduction, these transitions are a robust feature of the WRF SCM with CAM physics, as long as the WTG approximation is implemented. Varying horizontal resolution has little effect on the transition behavior. Varying the WTG relaxation timescale τ has a more significant effect, with the $f_{\mathrm{LS}} \to 1$ behavior more common and happening earlier for larger τ. Furthermore, I find broadly similar behavior with prescribed radiative cooling of -1.5 K/day over the troposphere. The nice steplike transitions are not as common, and f_{LS} can show more oscillatory behavior, but the column can still transition to higher f_{LS} and the $f_{\mathrm{LS}} \to 1$ transition can still occur.

4.6 Conclusion

Using the WRF single-column model with CAM physics parameterizations and incorporating the weak temperature gradient approximation, I have found that abrupt transitions occur when SST is continuously increased, mimicking low-level convergence of sensible and latent heat. Beyond certain threshold temperatures, the column abruptly transitions to a new configurations with larger fractions of large-scale (or non-convective) rainfall. The stability of the column under WTG conditions appears to depend on delicate balances established between the various temperature and moisture forcings, and the SST-induced transitions appear to be initiated by a breakdown in

the lower-column microphysical cooling. This breakdown can be traced to Eq. 4.7 which determines evaporative cooling; raw output from this equation suggests that the local temperature and moisture are more important than droplet number or mixing ratio in initiating the transitions.

While I have succeeded in narrowing down the source of the nonlinearity driving the abrupt transitions displayed by the WRF SCM in these experiments, ideally a more precise understanding of the relevant tipping point could be obtained. Hence future work includes further analysis of the these WRF transitions and testing for the existence of similar transitions when using the other physics parameterizations available in the WRF model. I also intend to analyze similar findings in a second SCM, the Rennó et al. [82] model incorporating Kerry Emanuel's convection scheme [31] and the Chou et al. [24] radiation scheme. This model, which was used by Sobel and Bretherton in their initial work with the WTG approximation [99], is capable of implementing the WTG approximation using the fixed-temperature scheme described in Section 2.3.2.1, and like the WRF SCM it also shows abrupt changes as the SST is continuously increased, although quasi-stationary state behavior seems to be less readily obtained. Future work could also include coupling SCMs to study the impact of additional degrees of freedom—this may be facilitated by the nature of the WRF model, which is normally run in a regional configuration with coupled columns.

The applicability of these findings to the CCSM3 hosing experiments described in Chapter 2 is less clear than in the case of the Chapter 3 findings.

The trigger for the abrupt change event observed in CCSM3 was thought to be low-level convergence of sensible and latent heat in the western Pacific warm pool region. And while it is encouraging that SST-forcing mimicking such low-level convergence causes abrupt increases in column f_{LS} similar to the abrupt increases in tropical f_{LS} seen in CCSM3, the interpretation is complicated by differences between the WRF and CCSM3 physics parameterizations. CAM physics parameterizations are updated with each version, and, despite some similarities, the CAM physics employed by the WRF SCM is that of a later version of CAM than that deployed in CCSM3. The use of the newer physics was necessitated by the version of WRF in which the WTG approximation had been implemented, but a clear extension of this work would be to implement the WTG approximation in a SCM containing the same physics parameterizations as CCSM3.

Chapter 5

Conclusion

As global climate change accelerates under anthropogenic GHG forcing, greater understanding of abrupt climate change—known to have occurred in the distant past—will be essential in helping communities around the world adapt. Heretofore, however, the study of abrupt climate change has often been limited both by a focus on the ocean as the source of abrupt change, and by the use of toy mathematical models or highly idealized numerical models. In this dissertation, inspired by the unusual tropical circulation and rainfall pattern discovered in the NCAR CCSM3 coupled climate model hosing experiments described in Chapter 2, I have investigated the question of whether the atmosphere may also initiate abrupt climate change and have used two types of realistic atmospheric model to do so.

I have demonstrated that the way models partition total precipitation between different types, primarily convective and large-scale rain, is both sensitive to external forcing and strongly linked to large-scale tropical circulation and rainfall patterns in global models, including in the modeled response to global warming. Moreover, the complexity of the relationships between external forcing and rainfall partitioning on the one hand, and rainfall partitioning

and large-scale circulation on the other, are such that abrupt transitions are possible as the equations representing the model physics are integrated forward in time. This is explicit in the case of the WRF SCM responding to increasing SST, where abrupt transitions in f_{LS} are readily observed when the weak temperature gradient approximation is implemented. But the possibility of abrupt transitions is also suggested by the behavior of the CAM3.1 ensemble described in Chapter 3, in which shallow convection seems to abruptly turn on for experiments with small deep convective rainfall rates.

As rainfall partitioning is likely to remain a feature of climate models for the foreseeable future, the questions addressed in this dissertation will remain relevant as well, and warrant further investigation. Regarding the behavior I have discovered in the WRF SCM, next steps include further clarifying the nature of the tipping point, ascertaining the generality of the abrupt transition behavior in other SCMs and using other physical parameterizations, and coupling SCMs together to see to what extent the features discovered here survive in models with more degrees of freedom. Regarding the CAM ensembles, a number of interesting and important questions remain to be addressed, including to what extent these results generalize to other atmospheric models, how these results are affected by coupling the atmosphere to a dynamic ocean, further exploration of nonlinearities present in the handoff between different rainfall types and implications for rainfall projections, and learning how to better translate between observed and model-world convective and large-scale rain.

Appendices

Appendix A

List of Abbreviations

AMOC	Atlantic meridional overturning circulation
CAM	Community Atmosphere Model
CAPE	convective available potential energy
CCSM3	Community Climate System Model, version 3
CIN	convective inhibition
CMIP	Coupled Model Intercomparison Project
DJF	December, January, February
EL	equilibrium level
EOF	empirical orthogonal functions
GCM	general circulation model
GHG	greenhouse gas
ITCZ	intertropical convergence zone
JJA	June, July, August
LCL	lifting condensation level
LFC	level of free convection
NCAR	National Center for Atmospheric Research
RCE	radiative-convective equilibrium
RCP	Representative Concentration Pathway
SCM	single-column model
SST	sea surface temperature
TRMM	Tropical Rainfall Measuring Mission
WRF	Weather Research and Forecasting (model)
WTG	weak temperature gradient

Appendix B

Some Derivations

B.1 Potential temperature

The potential temperature can be derived from integrating the adiabatic first law of thermodynamics after substituting in the ideal gas law:

$$c_p dT = \frac{dp}{\rho} \quad \Longrightarrow \quad \frac{c_p}{R} \int \frac{dT}{T} = \int \frac{dp}{p}.$$

This leads to

$$\frac{c_p}{R_d} \ln\left(\frac{T}{T_0}\right) = \ln\left(\frac{p}{p_0}\right) \quad \Longrightarrow \quad \frac{T}{T_0} = \left(\frac{p}{p_0}\right)^{R_d/c_p}.$$

Taking p_0 to be the surface pressure and $T_0 \equiv \theta$, we have the definition of potential temperature:

$$\theta = T\left(\frac{p_0}{p}\right)^{R_d/c_p}.$$

B.2 Virtual temperature

The virtual temperature T_v can be used in place of the usual temperature T to account for the presence of moisture. For moist air, the total pressure is the dry air pressure p_d and the water vapor pressure e: $p = p_d + e$. Since partial pressures behave independently, each satisfies its own ideal gas law at

the same temperature T but with separate specific gas constants and densities:

$$p = \rho_d R_d T + \rho_v R_v T.$$

Multiplying and dividing by the total density ρ, this can be written

$$p = \rho R_d \left(\frac{\rho_d}{\rho} + \frac{\rho_v}{\rho} \frac{R_v}{R_d} \right) T = \rho R_d \left(\frac{1 + q/\varepsilon}{1 + q} \right) T,$$

where $\varepsilon \equiv R_d/R_v$ and $q \equiv m_v/m_d = \rho_v/\rho_d$ is the usual water vapor mixing ratio. Hence virtual temperature is defined as

$$T_v \equiv \left(\frac{1 + q/\varepsilon}{1 + q} \right) T.$$

In practice it is often assumed that $q \ll 1$, giving $T_v \approx (1 + 0.62q)T$.

B.3 Meridional energy transport

To find the amount of energy per unit time transported across a particular latitude (i.e. in the meridional direction) at all heights, we integrate $\rho\, v\, \mathcal{E}$ (with $\mathcal{E}$ given by Eq. 2.19) over an annulus extending zonally around that parallel and from Earth's surface to the top of the atmosphere:

$$P = \iint \rho\, v\, \mathcal{E}\, dz\, d\lambda.$$

The integral over λ can be replaced with a zonal average over the energy transport multiplied by a factor of $2\pi R \cos\phi$:

$$P = 2\pi R \cos\phi \int \langle \rho\, v\, \mathcal{E} \rangle_\lambda\, dz = 2\pi R \cos\phi \int \langle\, v\, \mathcal{E} \rangle_\lambda\, \rho\, dz,$$

where $\langle\rangle_X$ denotes an average over the dimension given by X and in the last step we have taken the density ρ outside of the zonal average by the hydrostatic approximation (2.11), under which ρ depends only on the vertical coordinate. We can make further use the hydrostatic approximation to replace the factor of $\rho\, dz$, converting this to an integral over pressure:

$$P = \frac{2\pi R}{g} \cos\phi \int \langle v\, \mathcal{E} \rangle_\lambda \, dp.$$

[The minus sign in (2.11) goes away if we now integrate from the top of the atmosphere downward, in the direction of increasing pressure.]

We now discretize the integral into a sum, since one always deals with discrete data in both climate models and observations. We let i, j, and k index the zonal, meridional, and vertical directions respectively:

$$P_j = \frac{2\pi R}{g} \cos\phi_j \left(\frac{1}{N_\lambda} \sum_{i,k} v_{i,k} \mathcal{E}_{i,k}\, \Delta p_{i,k} \right).$$

We divide by N_λ—the number of grid cells in the zonal direction—when taking the zonal average. Expanding $\mathcal{E}$ again according to (2.19) gives (2.20).

B.4 Evaporation of raindrops

Here I give the derivation of Eq. 4.7 determining evaporation from raindrops in the CAM microphysics parameterization. Early steps toward this expression were published in the 1960s by Byers [11], who started with mass diffusion from a raindrop governed by

$$\frac{dM}{dt} = 4\pi r^2 D_v \frac{d\rho_v}{dr}, \tag{B.1}$$

where M is droplet mass, ρ_v is water vapor density, and D_v is the mass diffusion coefficient for water vapor. Integrating (B.1) and using $\frac{dM}{dt} = \rho_L 4\pi r^2 \frac{dr}{dt}$ (where ρ_L is the density of liquid water and r is the droplet radius) and the ideal gas law for water vapor leads to

$$r\frac{dr}{dt} = \frac{D_v}{\rho_L R_v T}\left[e - e(T_r)\right], \tag{B.2}$$

where R_v is the specific gas constant for water vapor and e and $e(T_r)$ are the ambient vapor pressure and the vapor pressure at the droplet surface (with temperature T_r) respectively. B.2 can be rewritten in terms of the saturation vapor pressure e_s as

$$\frac{e}{e_s} = \frac{e(T_r)}{e_s} + \frac{\rho_L R_v T}{e_s D_v} r\frac{dr}{dt}. \tag{B.3}$$

By relating the change in mass to the change in latent heat, it can also be shown that

$$r\frac{dr}{dt} = \frac{K}{\rho_L L}(T_r - T), \tag{B.4}$$

where K and L are the thermal conductivity and latent heat of vaporization respectively. B.4 can be written in terms of $e(T_r)/e_s$ (and hence inserted into B.3) by first integrating the Clausius-Clapeyron equation to obtain

$$\ln\frac{e(T_r)}{e_s} = \frac{L}{R_v T^2}(T_r - T),$$

where $T_r T \approx T^2$ has been assumed in the denominator. Substituting (B.4), we have $\frac{e(T_r)}{e_s} = \exp\left(\frac{\rho_L L^2}{K R_v T^2} r\frac{dr}{dt}\right)$, so that (B.3) becomes

$$S \equiv \frac{e}{e_s} = \exp\left(\frac{\rho_L L^2}{K R_v T^2} r\frac{dr}{dt}\right) + \frac{\rho_L R_v T}{e_s D_v} r\frac{dr}{dt}. \tag{B.5}$$

The next step is to assume the argument of the exponential is small, such that by a series expansion of the first term this can be rearranged as

$$r\frac{dr}{dt} = \frac{S-1}{\rho_L L^2/KR_vT^2 + \rho_L R_v T/e_s D_v}.$$

Again using $\frac{dM}{dt} = \rho_L 4\pi r^2 \frac{dr}{dt}$, this becomes the Byers [11] expression:

$$\frac{dM}{dt} = \frac{2\pi D(S-1)}{L^2/KR_vT^2 + R_vT/e_sD_v}\, f_V, \tag{B.6}$$

where $D = 2r$ is the raindrop diameter. The final term f_V is a "ventilation factor" accounting for enhanced evaporation due to air flow past the droplet. Byers [11] used $f_V = 1 + 0.22\mathrm{Re}^{1/2}F$, where Re is the Reynolds number and F was thought to be approximately unity for the Re of interest [11, 122]. By the early 1970s, the ventilation factor had become $f_V \approx 0.780 + 0.308 S_C^{1/3}\mathrm{Re}^{1/2}$ [4], where $S_C \equiv \nu/D_v$ is the Schmidt number and ν is the kinematic viscosity.

In cloud microphysics, condensed particle or "hydrometeor" size distributions are often written as gamma distributions. The standard derivation of Eq. 4.7 assumes a distribution of the form

$$N(D)\, dD = N_0 \exp\left(-\Lambda D\right) dD, \tag{B.7}$$

where N_0 and Λ are spectral parameters. The terminal fall speed for a particle of diameter D is also usually expressed as a function of D, $u_D = aD^b$ with a and b empirically determined. Wisner et al. [122] integrated (B.6) with (B.7) using the Byers [11] ventilation factor and $\mathrm{Re} = u_D D/\nu = (aD^b)D/\nu$:

$$P_E = \int \frac{dM}{dt} N(D)\, dD = \xi \int_0^\infty D\left[1 + 0.22\left(\frac{aD^{b+1}}{\nu}\right)^{1/2}\right] \exp\left(-\Lambda D\right)\, dD,$$

where $\xi \equiv 2\pi N_0(S-1)\left(L^2/KR_vT^2 + R_vT/e_sD_v\right)^{-1}$. This gives

$$P_E = \xi\left[\Lambda^{-2} + 0.22a^{1/2}\nu^{-1/2}\Gamma\left(\frac{b+5}{2}\right)\Lambda^{-(b+5)/2}\right].$$

More recent versions of the expression (e.g., [75], [57]) use a variant of the updated ventilation factor, and this is the form used in the Morrison-Gettelman CAM microphysics parameterization [66]:

$$P_E = \frac{2\pi N_0(S-1)\left[0.78\Lambda^{-2} + 0.32S_C^{1/3}a^{1/2}\nu^{-1/2}\Gamma\left(\frac{b+5}{2}\right)\Lambda^{-(b+5)/2}\right]}{\dfrac{L^2}{KR_vT^2} + \dfrac{R_vT}{e_sD_v}}.$$

Appendix C

CAM Ensemble Construction

This Appendix discusses the construction of the CAM3.1 and CAM5.3 ensembles used in Chapter 3, starting with a description of Bayesian calibration of climate models and the Multiple Very Fast Simulated Annealing (MVFSA) sampling method, based on [94], [47], [46], and [45]. I then detail the test statistics employed for each CAM ensemble and the observational data used to evaluate those test statistics.

C.1 Bayesian calibration and MVFSA

Climate models depend on a variety of physical parameters whose values are uncertain. The goal of Bayesian calibration is to use statistical methods and observational data to construct a posterior probability density function (PPD) indicating parameter values that allow a climate model to generate output consistent with observations, thus "calibrating" the model. From Bayes's rule, the PPD is

$$ppd(\mathbf{m}|\mathbf{d}) = \frac{p(\mathbf{d}|\mathbf{m})p(\mathbf{m})}{p(\mathbf{d})}, \tag{C.1}$$

where $\mathbf{m}$ and $\mathbf{d}$ are vectors representing model parameters and "data" respectively, $p(\mathbf{d}|\mathbf{m})$ is the conditional probability of obtaining data vector $\mathbf{d}$

with model parameters $\mathbf{m}$, $p(\mathbf{m})$ represents the prior probability of model vector $\mathbf{m}$, and $p(\mathbf{d})$ is the probability of data vector $\mathbf{d}$. In a climate-modeling context, one interprets $\mathbf{d}$ as observational data $\mathbf{d}_{\text{obs}}$, and, assuming Gaussian errors, $p(\mathbf{d}|\mathbf{m})$ is proportional to $\exp(-SE(\mathbf{m}))$, where S is a scaling factor and $E(\mathbf{m})$ is the test statistic which quantifies the significance of the difference between model output based on $\mathbf{m}$ and observational data $\mathbf{d}_{\text{obs}}$. Eq. C.1 thus becomes

$$ppd(\mathbf{m}|\mathbf{d}_{\text{obs}}) = \frac{\exp(-E(\mathbf{m}))p(\mathbf{m})}{\int \exp(-SE(\mathbf{m}))p(\mathbf{m})\, d\mathbf{m}}, \tag{C.2}$$

where the denominator ensures normalization and the dependence on $\mathbf{d}_{\text{obs}}$ is now contained within the test statistic. Determining $ppd(\mathbf{m}|\mathbf{d}_{\text{obs}})$ is now a matter of evaluating the right-hand side of (C.2) by running the numerical model for all $\mathbf{m}$, which for a complex model like CAM is prohibitively expensive. Hence one needs a way of efficiently sampling the parameter space.

We generate samples from the posterior distribution using an approximate Markov Chain Monte Carlo (MCMC) sampling algorithm MVFSA [47]. At each step through parameter space, the Markov chain uses Metropolis-Hastings sampling [63, 37] to select values for uncertain model parameters as well as Gibbs sampling [34] to select values for a precision hyper-parameter that accounts for sources of uncertainty affecting the gap between models and data such as model biases [45]. One of the primary sources of inefficiency in any MCMC sampling algorithm is due to a non-ideal step size. MVFSA mitigates this source of inefficiency by using an iteration-dependent Cauchy distribution to gradually reduce step size over the course of the calibration [42].

By deploying multiple Markov Chains in parallel and exercising convergence criteria that are tied to a problem's uncertainty space dimensionality, MVFSA is able to summarize important aspects of the posterior distribution with relatively few integrations of a computationally expensive numerical model [108]. Among those that use Bayesian calibration strategies for large-scale numerical codes, it is rather unusual to sample the posterior distribution directly using MCMC sampling. The more common approach is to develop a statistical emulator of one's numerical model based on a designed set of experiments such as a latin-hypercube structure. However, developing emulators of high-dimensional model output can be prohibitively difficult. The advantage of direct sampling, if it can be managed, is that it allows one to make use of sophisticated test statistics of model performance that account for skill in capturing observed dependencies in space and across multiple fields [67, 71]. This to be a favorable trade-off, especially if one only needs to generate an ensemble that spans a range of outcomes that is useful for exploring specific science questions.

C.2 Model skill test statistic

The methodology described in Section A1 was used to construct both the CAM3.1 and CAM5.3 ensembles analyzed in Chapter 3. For the CAM3.1 ensemble, the original intent was to sample the space of 15 parameters related to clouds and convection, while for the CAM5.3 ensemble, the intent was to sample the space of seven parameters related to clouds and convection, in both cases in order to find optimal parameters for the models to repro-

duce observations (see Table A1 for the parameters perturbed in the CAM ensembles). The test statistics used for the two ensembles, respectively, are a "traditional" test statistic and a "field-and-space" test statistic. In both cases, the schematic form of the test statistic, which follows from the assumption of Gaussian errors, is

$$E(\mathbf{m}) = \frac{1}{2} \sum_{i=1}^{N} \left\{ \left[\mathbf{d}_{\text{obs}} - \mathbf{g}(\mathbf{m}) \right]^T \mathbf{C}^{-1} \left[\mathbf{d}_{\text{obs}} - \mathbf{g}(\mathbf{m}) \right] \right\}_i . \tag{C.3}$$

Here there are N types of observations, $\mathbf{C}^{-1}$ is the inverse error covariance matrix (taking into account differences between model output and observations caused by internal variability), $\mathbf{g}(\mathbf{m})$ represents model output given parameters $\mathbf{m}$, and T denotes the transpose. The test statistics used in the construction of both CAM ensembles follow (C.3) schematically, but the form of the matrix $\mathbf{C}^{-1}$ differs. Jackson and Huerta [45] give the details of the test statistic calculations for the CAM3.1 ensemble; for the details of the CAM5.3 ensemble calculations, see [71] and [111].

Various sources of observational data were used in evaluating the test statistics for the two CAM ensembles. For the CAM3.1 ensemble, observational data were drawn from [119] (2 m air temperatures), ERA-40 data (vertically averaged air temperature and relative humidity, sea level pressure, and 300 mb zonal winds), [128] (ocean latent heat fluxes), Clouds and the Earth's Radiant Energy System (CERES2) data (long- and short-wave cloud forcing), Global Precipitation Climatology Project (GPCP) data (precipitation), and ERS-2 data for the 5°S-5°N Pacific Ocean wind stress [127]. For the

Name	Description	File/Scheme	Default	Low	High
	CAM3.1				
alfa (nondim.)	Initial cloud downdraft mass flux	zm_conv	1e–1	5e–2	6e–1
c0 (m^{-1})	Precipitation efficiency	zm_conv	3e–3	2.5e–4	6e–3
capnc (cm^{-3})	Cold, oceanic cloud particles	cldwat	150	50	50
capnsi (cm^{-3})	Sea ice cloud particles	cldwat	75	50	300
capnw (cm^{-3})	Warm continental cloud particles	cldwat	4e2	3e2	1e3
icritc (nondim.)	Threshold for autoconversion of cold ice	cldwat	11e–6	2e–6	18e–6
icritw (nondim.)	Threshold for autoconversion of warm ice	cldwat	8e–4	1e–4	10e–4
ke (kg m^{-2} s^{-1})$^{-1/2}s^{-1}$	Environmental air entrainment rate	zm_conv	3e–6	0.5e–6	1e–5
rhminh (%)	Critical relative humidity high clouds	cloud_fraction	0.80	0.60	0.90
rhminl (%)	Critical relative humidity low clouds	cloud_fraction	0.90	0.80	0.95
rliqice (μm)	Cloud droplet size, ice	pkg_cldoptics	14	7	18
rliqland (μm)	Cloud droplet size, liquid and continental	pkg_cldoptics	8	4	10
rliqocean (μm)	Cloud droplet size, liquid and oceanic	pkg_cldoptics	14	7	18
tau (s)	Consumption rate of CAPE	zm_conv	3.6e3	1.8e3	2.8e4
vice_small (cm s^{-1})	Ice fall velocity	pkg_cld_sediment	1	0.5	100
	CAM5.3				
micro_mg_dcs (m)	Threshold for autoconversion of cloud ice	Cld. micro.	2.5e–4	1e–4	5e–4
cldfrc_rhminl (%)	Critical relative humidity low clouds	Cld. macro.	0.8975	0.8000	0.9900
uwshcu_rpen (kg kg^{-1})	Ratio of penetratively entrained to detrained air	Sh. conv.	10	1	30
uwshcu_criqc (kg kg^{-1})	Maximum updraft condensate mixing ratio	Sh. conv.	7e–4	4e–4	1.5e–3
zmconv_tau (s)	Consumption rate of CAPE	Deep conv.	3600	1800	36000
zmconv_dmdpz (m^{-1})	Parcel fractional mass entrainment rate	Deep conv.	−1e–3	−2e–3	−2e–4
eddydiff_a2 (nondim.)	Moist entrainment enhancement parameter	Atmo. BL	30	10	60

Table C.1: Names and descriptions of the perturbed parameters for the CAM ensembles, along with the files/subroutines in which they are found and their default values and ranges within the MVFSA sampling [109]. For the CAM3.1 ensemble, the names of the physics files are given (i.e., \physics\filename.F90). For the CAM5.3 ensemble, the parameterization scheme is given.

CAM5.3 ensemble, GPCP data were used for rainfall; ERA-Interim reanalysis for temperature, humidity, wind speeds, and sea level pressure; CERES data for shortwave and longwave cloud forcings; and Cloud-Aerosol Lidar and Infrared Pathfinder Satellite Observations (CALIPSO) for cloud fractions [109].

C.3 Binning Schemes

Here I describe the binning scheme used to create Figs. 3.4, 3.5, and 3.6, which while somewhat arbitrary does not significantly affect the results of Chapter 3. Figure C.1 displays histograms in f_{LS} for the three ensembles, along with the details of the binning for the ensembles. The binning was carried out, somewhat arbitrarily, using the mean and standard deviation of f_{LS} for each ensemble. For CAM3.1 (Fig. 3.4; see Fig. C.1 here), the binning was done by grouping those models whose f_{LS} was more than one standard deviation from the mean above or below, those models whose f_{LS} was more than half the standard deviation from the mean but less than a full standard deviation away, and those models within half a standard deviation of the mean. For the CAM5.3 and CMIP5 ensembles, the three bins were created by grouping those models more than one standard deviation from the mean above or below, and those models within one standard deviation from the mean (Figs. 3.5 and 3.6).

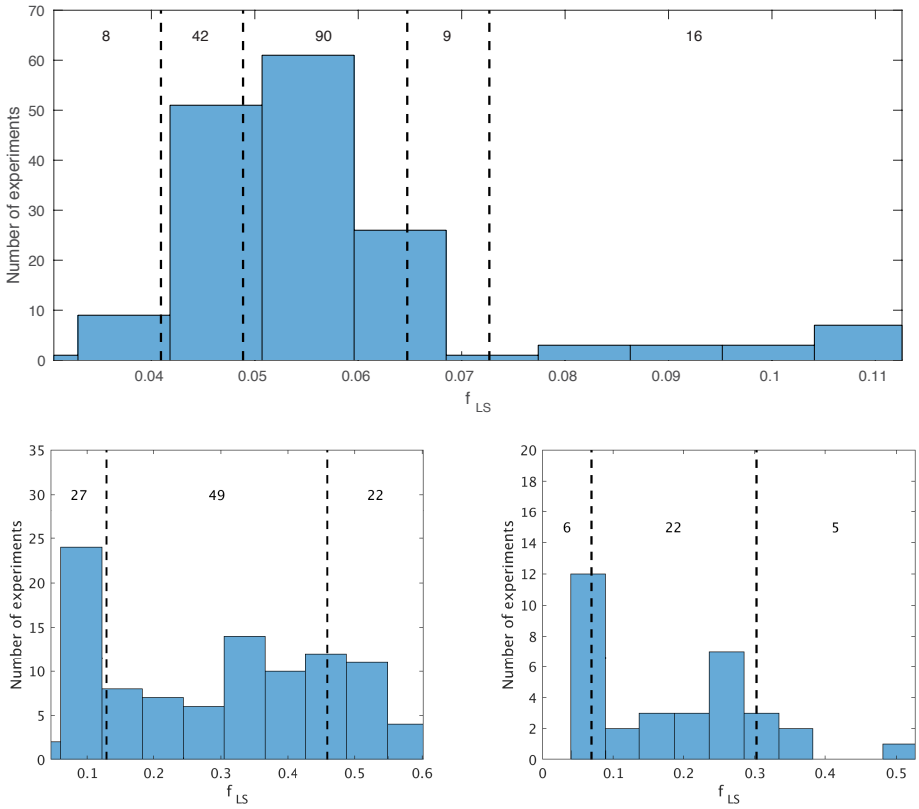

Figure C.1: Top: The distribution of f_{LS} for the CAM3.1 ensemble and dashed lines indicating the binning scheme and the number of experiments in each bin. The dashed lines, from left to right, are set at one standard deviation below the mean, half a standard deviation below the mean, half a standard deviation above the mean, and one standard deviation above the mean. Bottom left: The distribution of f_{LS} for the CAM5.3 ensemble and dashed lines indicating the binning scheme and the number of experiments in each bin. The dashed lines, from left to right, are set at one standard deviation below the mean and one standard deviation above the mean. Bottom right: The distribution of f_{LS} for the CMIP5 ensemble and dashed lines indicating the binning scheme and the number of experiments in each bin. The dashed lines, from left to right, are set at one standard deviation below the mean and one standard deviation above the mean.

Appendix D

EOF Calculations

This Appendix describes the steps of the empirical orthogonal function (EOF) analysis to arrive at the results accompanying Figs. 3.7 and 3.8. The goals of these calculations are to find the proportion of the total variance of the mean precipitation response attributable to f_{LS} and to see how linearly the response patterns vary with f_{LS}. The total variance within a field can be calculated by an eigenvalue decomposition of its covariance matrix, so I begin by vectorizing the responses for each ensemble member (i.e. turning each 2D map into a 1D array) to obtain a matrix of dimension (i, j) where i indexes the ensemble member and j indexes the ith member's vectorized response map. I then calculate the covariance matrix and decompose it into EOFs via the standard eigenvalue problem. I truncate the evaluation at ten EOFs. Each eigenvalue λ_k $(k = 1, \ldots, 10)$ quantifies the variance explained by its corresponding EOF, and the total variance within the response field is the sum $\sum_k \lambda_k$.

To quantify the proportion of the response attributable to f_{LS}, I start by defining

$$\Delta R = \overline{R}^{\mathrm{bin}}_{\text{high-}f_{\mathrm{LS}}} - \overline{R}^{\mathrm{bin}}_{\text{low-}f_{\mathrm{LS}}}, \tag{D.1}$$

where R refers to the response, "high-" and "low-" f_{LS} refer to those experiments more than one standard deviation from the mean, and the notation $\overline{X}^{\mathrm{bin}}$ indicates a bin average. (Fig. 3.7 shows both the mean response pattern and ΔR for CAM3.1.) I then center and normalize ΔR,

$$\Delta R' = \frac{\Delta R - \overline{\Delta R}}{|\Delta R|}, \tag{D.2}$$

where in the numerator I subtract the grid-point average of the map ($\overline{\Delta R}$) from each point of ΔR, and $|\Delta R|$ is the amplitude of ΔR, found by vectorizing the map and taking $|\Delta R| = \sqrt{(\Delta R)^T \Delta R}$. Assuming that $\Delta R'$ represents the spatial pattern associated with f_{LS} for the ensemble, I then subtract $\Delta R'$ from each ensemble member's anomaly map A_i, weighted by its amplitude with $\Delta R'$. That is, I define an $\tilde{A}_i$ for each ensemble member such that

$$\tilde{A}_i = A_i - \alpha_i \Delta R', \tag{D.3}$$

where $\alpha_i = A_i \cdot \Delta R'$. I expect this operation to remove the part of the response pattern attributable to f_{LS}. I then repeat the EOF analysis to quantify the remaining variance; that is, I repeat the steps described above to obtain a new value for $\sum_k \tilde{\lambda}_k$, where $\tilde{\lambda}_k$ are the new covariance-matrix eigenvalues calculated using the $\tilde{A}_i$.

Bibliography

[1] Pradeep K. Aggarwal, Ulrike Romatschke, Luis Araguas-Araguas, Dagnachew Belachew, Frederick J. Longstaffe, Peter Berg, Courtney Schumacher, and Aaron Funk. Proportion of convective and stratiform precipitation revealed in water isotope ratios. *Nature: Geoscience*, 9:624–629, August 2016.

[2] Richard B. Alley. The younger dryas cold interval as viewed from central greenland. *Quarternary Science Reviews*, 19:213–226, 2000.

[3] J. T. Bacmeister, M. F. Wehner, R. B. Neale, A. Gettelman, C. Hannay, P. H. Lauritzen, J. M. Caron, and J. E. Truesdale. Exploratory high-resolution climate simulations using the Community Atmosphere Model (CAM). *Journal of Climate*, 27(9):3073–3099, 2014.

[4] K. V. Beard and H. R. Pruppacher. A wind tunnel investigation of the rate of evaporation of small water drops falling at terminal velocity in air. *Journal of the Atmospheric Sciences*, 28:1455–1464, November 1971.

[5] Gilles Bellon and Adam H. Sobel. Multiple equilibria of the hadley circulation in an intermediate-complexity axisymmetric model. *Journal of Climate*, 23:1760–1778, April 2010.

[6] Sebastian Bethiany, Henk Dijkstra, Michel Crucifix, Vasilis Dakos, Victor Brovkin, Mark S. Williamson, Timothy M. Lenton, and Martin Scheffer. Beyond bifurcation: using complex models to understand and predict abrupt climate change. *Dynamics and Statistics of the Climate System*, 1(1):1–31, 2016.

[7] A. K. Betts. Climate-convection feedbacks: Some further issues. *Climate Change*, 39:35–38, 1998.

[8] Christopher S. Bretherton and Piotr K. Smolarkiewicz. Gravity waves, compensating subsidence and detrainment around cumulus clouds. *Journal of the Atmospheric Sciences*, 46(6):740–759, March 1989.

[9] Wally Broecker. *The Great Ocean Conveyor: Discovering The Trigger for Abrupt Climate Change*. Princeton University Press, 2010.

[10] M. I. Budyko. The effect of solar radiation variations on the climate of the Earth. *Tellus*, 11(5):611–619, 1969.

[11] Horace Robert Byers. *Elements of Cloud Physics*. The University of Chicago Press, 1965.

[12] M. P. Byrne and P. A. O'Gorman. The response of precipitation minus evapotranspiration to climate warming: why the "wet-get-wetter, dry-get-drier" scaling does not hold over land. *Journal of Climate*, 28:8078–8092, 2015.

[13] R. D. Cess, G. L. Potter, J. P. Blanchet, G. J. Boer, A. D. Del Genio, M. Déqué, V. Dymnikov, V. Galin, W. L. Gates, S. J. Ghan, J. T. Kiehl, A. A. Lacis, H. Le Treut, Z.-X. Liang, B. J. McAvaney, V. P. Meleshko, J. F. B. Mitchell, J.-J. Morcrette, D. A. Randall, L. Rikus, E. Roeckner, J. F. Royer, U. Schlese, D. A. Sheinin, A. Slingo, A. P. Sokolov, K. E. Taylor, W. M. Washington, R. T. Wetherald, I. Yagai, and M.-H. Zhang. Intercomparison and interpretation and climate feedback processes in 19 atmospheric general circulation models. *Journal of Geophysical Research*, 95(D10):16601–16615, September 1990.

[14] R. Chadwick, I. Boutle, and G. Martin. Spatial patterns of precipitation change in CMIP5: Why the rich do not get richer in the tropics. *Journal of Climate*, 26:3803–3822, 6 2013.

[15] Moustafa T. Chahine. The hydrological cycle and its influence on climate. *Nature*, 359:373–380, 1992.

[16] J. G. Charney. A note on large-scale motions in the tropics. *Journal of the Atmospheric Sciences*, 20:607–609, 1963.

[17] J. G. Charney. A further note on large-scale motions in the tropics. *Journal of the Atmospheric Sciences*, 26:182–185, 1969.

[18] H. Chen, J. Sun, and X. Chen. Projection and uncertainty analysis of global precipitation-related extremes using CMIP5 ensemble. *International Journal of Climatology*, 34:2730–2748, 2014.

[19] John C. H. Chiang. The tropics in paleoclimate. *The Annual Review of Earth and Planetary Sciences*, 37:263–297, 2009.

[20] C. Chou and C.-A. Chen. Depth of convection and the weakening of tropical circulation in global warming. *Journal of Climate*, 23:3019–3030, 2010.

[21] C. Chou and J. D. Neelin. Mechanisms of global warming impacts on regional tropical precipitation. *Journal of Climate*, 17:2688–2701, 2004.

[22] C. Chou, J. D. Neelin, C.-A. Chen, and J.-Y. Tu. Evaluating the "rich-get-richer" mechanism in tropical precipitation chnage under global warming. *Journal of Climate*, 22:1982–2005, 2009.

[23] C. Chou, T.-C. Wu, and P.-H. Tan. Changes in gross moist stability in the tropics under global warming. *Climate Dynamics*, 41:2481–2496, 2013.

[24] M.-D. Chou, D. P. Kratz, and W. Ridgway. Infrared radiation parameterizations in numerical climate models. *Journal of Climate*, 4:424–437, 1991.

[25] M. Collins, R. Knutti, J. Arblaster, J.-L. Dufresne, T. Fichefet, P. Friedlingstein, X. Gao, W. J. Gutowski, T. Johns, G. Krinner, M. Shongwe, C. Tebaldi, A.J. Weaver, and M. Wehner. Long-term climate change: Projections, commitments and irreversibility. In: *Climate Change 2013: The Physical Science Basis. Contribution of Working Group I to the*

Fifth Assessment Report of the Intergovernmental Panel on Climate Change, [Stocker, T. F., D. Qin, G.-K. Plattner, M. Tignor, S. K. Allen, J. Boschung, A. Nauels, Y. Xia, V. Bex and P. M. Midgley (eds.)]. Cambridge University Press, Cambridge, United Kingdom and New York, NY, USA, 2013.

[26] National Research Council. *Abrupt Impacts of Climate Change: Anticipating Surprises*. The National Academies Press, 2013.

[27] Thomas M. Cronin. *Paleoclimate: Understanding Climate Change Past and Present*. Columbia University Press, 2010.

[28] Aiguo Dai. Precipitation characteristics in eighteen coupled climate models. *Journal of Climate*, 19:4605–4630, 2006.

[29] C. L. Daleu, R. S. Plant, S. J. Woolnough, S. Sessions, M. J. Herman, A. Sobel, S. Wang, D. Kim, A. Cheng, G. Bellon, P. Peyrille, F. Ferry, P. Siebesma, and L. van Ulft. Intercomparison of methods of coupling between convection and large-scale circulation: 1. Comparison over uniform surface conditions. *Journal of Advances in Modeling Earth Systems*, 7:1576–1601, 2015.

[30] D. P. Dee, S. M. Uppala, A. J. Simmons, P. Berrisford, P. Poli, S. Kobayashi, U. Andrae, M. A. Balmaseda, G. Balsamo, P. Bauer, P. Bechtold, A. C. M. Beljaars, L. van de Berg, J. Bidlot, N. Bormann, C. Delsol, R. Dragani, M. Fuentes, A. J. Geer, L. Haimberger, S. B. Healy, H. Hersbach, E. V.

Hólm, L. Isaksen, P. Kållberg, M. Köhler, M. Matricardi, A. P. McNally, B. M. Monge-Sanz, J.-J. Morcrette, B.-K. Park, C. Peubey, P. de Rosnay, C. Tavolato, J.-N. Thépaut, and F. Vitart. The ERA-Interim reanalysis: configuration and performance of the data assimilation system. *Quarterly Journal of the Royal Meteorological Society*, 137:553–597, April 2011.

[31] K. A. Emanuel. A scheme for representing cumulus convection in large-scale models. *Journal of the Atmospheric Sciences*, 48:2313–2335, 1991.

[32] N. Feldl and S. Bordoni. Characterizing the Hadley circulation response through regional climate feedbacks. *Journal of Climate*, 29:613–622, January 2016.

[33] D. Frierson. The dynamics of idealized convection schemes and their effect on the zonally averaged tropical circulation. *Journal of the Atmospheric Sciences*, 64:1959–1976, 2007.

[34] A. E. Gelfand, A. F. Smith, and T.-M. Lee. Bayesian analysis of constrained parameter and truncated data problems using Gibbs sampling. *Journal of the American Statistical Association*, 87:523–532, 1992.

[35] A. Gettelman, J. E. Kay, and K. M. Shell. The evolution of climate sensitivity and climate feedbacks in the Community Atmosphere Model. *Journal of Climate*, 25(5):1453–1469, 2012.

[36] W. I. Gustafson, P.-L. Ma, and B. Singh. Precipitation characteristics of CAM5 physics at mesoscale resolution during MC3E and the impact of convective timescale choice. *Journal of Advances in Modeling Earth Systems*, 6:1271–1287, 2014.

[37] W. K. Hastings. Monte Carlo sampling methods using Markov chains and their applications. *Biometrika*, 57:97–109, 1970.

[38] Isaac M. Held and Arthur Y. Hou. Nonlinear axially symmetric circulations in a nearly inviscid atmosphere. *Journal of the Atmospheric Sciences*, 37:515–533, March 1980.

[39] Isaac M. Held and Brian J. Soden. Robust responses of the hydrological cycle to global warming. *Journal of Climate*, 19:5686–5699, November 2006.

[40] Isaac M. Held, Ming Zhao, and Bruce Wyman. Dynamic radiative-convective equilibria using GCM column physics. *Journal of the Atmospheric Sciences*, 64:228–238, 2007.

[41] L. Huaman and C. Schumacher. Assessing the vertical latent heating structure of the East Pacific ITCZ using the *CloudSat* CPR and TRMM PR. *Journal of Climate*, 31:2563–2577, April 2018.

[42] L. Ingber. Very fast simulated re-annealing. *Mathematical and Computer Modelling*, 12(8):967–973, 1989.

[43] IPCC. Summary for policymakers. In: Global warming of 1.5°C. An IPCC Special Report on the impacts of global warming of 1.5°C above pre-industrial levels and related global greenhouse gas emission pathways, in the context of strengthening the global response to the threat of climate change, sustainable development, and efforts to eradicate poverty [Masson-Delmotte, V., P. Zhai, H.-O. Pörtner, D. Roberts, J. Skea, P. R. Shukla, A. Pirani, W. Moufouma-Okia, C. Péan, R. Pidcock, S. Connors, J. B. R. Matthews, Y. Chen, X. Zhou, M. I. Gomis, E. Lonnoy, T. Maycock, M. Tignor, and T. Waterfield (eds.)]. World Meteorological Organization, Geneva, Switzerland, 2018.

[44] Charles S. Jackson, Ping Chang, Link Ji, and Vikram Parolkar. Dual-state behavior observed within the Community Climate System Model. (unpublished).

[45] Charles S. Jackson and G. Huerta. Empirical Bayes approach to climate model calibration. *Geoscientific Model Development Discussions*, pages 1–19, 2016.

[46] Charles S. Jackson, M. K. Sen, G. Huerta, Y. Deng, and K. P. Bowman. Error reduction and convergence in climate prediction. *Journal of Climate*, 21:6698–6709, 2008.

[47] Charles S. Jackson, M. K. Sen, and P. L. Stoffa. An efficient stochastic Bayesian approach to optimal parameter and uncertainty estimation for climate model predictions. *Journal of Climate*, 17(14):2828–2841, 2004.

[48] V. V. Kharin, F. W. Zwiers, X. Zhang, and M. Wehner. Changes in temperature and precipitation extremes in the CMIP5 ensemble. *Climatic Change*, 119:345–357, 2013.

[49] D. Khider, C. S. Jackson, and L. D. Stott. Assessing millennial-scale variability during the holocene: A perspective from the western tropical Pacific. *Paleoceanography*, 29:143–159, 2014.

[50] G. J. Kooperman, Y. Chen, F. M. Hoffman, C. D. Koven, K. Lindsay, M. S. Pritchard, A. L. S. Swann, and J. T. Randerson. Forest response to rising CO_2 drives zonally asymmetric rainfall change over tropical land. *Nature: Climate Change*, 8:434–440, 2018.

[51] G. J. Kooperman, M. S. Pritchard, T. A. O'Brien, and B. W. Timmermans. Rainfall from resolved rather than parameterized processes better represents the present-day and climate change response of moderate rates in the Community Atmosphere Model. *Journal of Advances in Modeling Earth Systems*, 10:1–18, 2018.

[52] Jan Kyselý, Zuzana Rulfová, Aleš Farda, and Martin Hanel. Convective and stratiform precipitation characteristics in an ensemble of regional climate model simulations. *Climate Dynamics*, 46:227–243, 2016.

[53] B. Langenbrunner, J. D. Neelin, B. R. Lintner, and B. T. Anderson. Patterns of precipitation change and climatological uncertainty among CMIP5 models, with a focus on the midlatitude pacific storm track. *Journal of Climate*, 28:7857–7872, 2015.

[54] Timothy M. Lenton. Early warning of climate tipping points. *Nature: Climate Change*, 1:201–209, July 2011.

[55] Timothy M. Lenton, Hermann Held, Elmar Kriegler, Jim W. Hall, Wolfgang Lucht, Stefan Rahmstorf, and Hans Joachim Schellnhuber. Tipping elements in the Earth's climate system. *Proceedings of the National Academy of Sciences*, 105(6):1786–1793, February 2008.

[56] Guangxing Lin, Hui Wan, Kai Zhang, Yun Qian, and Steven J. Ghan. Can nudging be used to quantify model sensitivities in precipitation and cloud forcing? *Journal of Advances in Modeling Earth Systems*, 8:1073–1091, 2016.

[57] Yuh-Lang Lin, Richard D. Farley, and Harold D. Orville. Bulk parameterization of the snow field in a cloud model. *Journal of Climate and Applied Meteorology*, 22:1065–1092, June 1983.

[58] B. R. Lintner and J. D. Neelin. Eastern margin variability of the south pacific convergence zone. *Geophysical Research Letters*, 35(L16701), 2008.

[59] Dongqing Liu, Ben Yang, Yaocun Zhang, Yun Qian, Anning Huang, Yang Zhou, and Lujun Zhang. Combined impacts of convection and microphysics parameterizations on the simulations of precipitation and cloud properties over Asia. *Atmospheric Research*, 212:172–185, 2018.

[60] Jian Ma and Shang-Ping Xie. Regional patterns of sea surface temperature change: a source of uncertainty in future projections of precipitation and atmospheric circulation. *Journal of Climate*, 26:2482–2501, April 2013.

[61] Jian Ma, Shang-Ping Xie, and Yu Kosaka. Mechanisms for tropical tropospheric circulation change in response to global warming. *Journal of Climate*, 25:2979–2994, April 2012.

[62] P.-L. Ma, P. J. Rasch, J. D. Fast, R. C. Easter, Jr. W. I. Gustafson, X. Liu, S. J. Ghan, and B. Singh. Assessing the CAM5 physics suite in the WRF-Chem model: implementation, resolution sensitivity, and a first evaluation for a regional case study. *Geoscientific Model Development*, 7:755–778, 2014.

[63] N. Metropolis, A. W. Rosenbluth, M. N. Rosenbluth, A. H. Teller, and E. Teller. Equation of state calculations by fast computing machines. *Journal of Chemical Physics*, 21:1087–1092, 1953.

[64] S. K. Mishra and J. Srinivasan. Sensitivity of the simulated precipitation to changes in convective relaxation time scale. *Annales Geophysicae*, 28:1827–1846, 2010.

[65] H. Morrison, J. A. Curry, and V. I. Khvorostyanov. A new double-moment microphysics parameterization for application in cloud and climate models. Part I: Description. *Journal of the Atmospheric Sciences*, 62:1665–1677, June 2005.

[66] Hugh Morrison and Andrew Gettelman. A new two-moment bulk stratiform cloud microphysics scheme in the Community Atmosphere Model, version 3 (CAM3). Part I: Description and numerical tests. *Journal of Climate*, 21:3642–3659, August 2008.

[67] Q. Mu, C. S. Jackson, and P. L. Stoffa. A multivariate empirical-orthogonal-function-based measure of climate model performance. *Journal of Geophysical Research: Atmospheres*, 109, 2004.

[68] Richard B. Neale, Jadwiga H. Richter, Sungsu Park, and Peter H. Lauritzen. The mean climate of the Community Atmosphere Model (CAM4) in forced SST and fully coupled experiments. *Journal of Climate*, 26:5150–5168, July 2013.

[69] J. D. Neelin, C. Chou, and H. Su. Tropical drought regions in global warming and El Niño teleconnections. *Geophysical Research Letters*, 30(24), 2003.

[70] David S. Nolan, Scott W. Powell, Chidong Zhang, and Brian E. Mapes. Idealized simulations of the intertropical convergence zone and its multilevel flows. *Journal of the Atmospheric Sciences*, 67:4028–4053, 2010.

[71] Alvaro Nosedal-Sanchez, Charles S. Jackson, and Gabriel Huerta. A new test statistic for climate models that includes field and spatial dependencies using Gaussian Markov random fields. *Geoscientific Model Development*, 9:2407–2414, 2016.

[72] T. A. O'Brien, W. D. Collins, K. Kashinath, O. Rubel, S. Byna, J. Gu, H. Krishnan, and P. A. Ullrich. Resolution dependence of precipitation statistical fidelity in hindcast simulations. *Journal of Advances in Modeling Earth Systems*, 8:1–15, 2016.

[73] H. Oeschger, J. Beer, U. Siegenthaler, B. Stauffer, W. Dansgaard, and C. C. Langway. Late glacial climate history from ice cores. *Climate Process and Climate Sensitivity*, 29, 1984.

[74] Yuko M. Okumura, Clara Deser, Aixue Hu, Axel Timmerman, and Shang-Ping Xie. North Pacific climate response to freshwater forcing in the Subarctic North Atlantic: oceanic and atmospheric pathways. *Journal of Climate*, 22:1424–1445, March 2009.

[75] Harold D. Orville and Fred J. Kopp. Numerical simulation of the life history of a hailstorm. *Journal of the Atmospheric Sciences*, 34:1596–1618, 1977.

[76] Sungsu Park and Christopher S. Bretherton. The university of washington shallow convection and moist turbulence schemes and their impact on climate simulations with the Community Atmosphere Model. *Journal of Climate*, 22:3449–3469, June 2009.

[77] Cécile Penland and Ludmila Matrosova. Studies of El Niño and interdecadal variability in tropical sea surface temperatures using a nonnormal filter. *Journal of Climate*, 19:5796–5815, November 2006.

[78] S. Pfahl, P. A. O'Gorman, and E. M. Fischer. Understanding the regional pattern of projected future changes in extreme precipitation. *Nature: Climate Change*, 7:423–427, 2017.

[79] Hans R. Pruppacher and James D. Klett. *Microphysics of Clouds and Precipitation*, volume 18 of *Atmospheric and Oceanographic Sciences Library*. Springer, 2010.

[80] Stefan Rahmstorf. Timing of abrupt climate change: A precise clock. *Geophysical Research Letters*, 30(10), 2003.

[81] Jouni Räisänen. How reliable are climate models? *Tellus*, 59A:2–29, 2007.

[82] Nilton O. Rennó, Kerry A. Emanuel, and Peter H. Stone. Radiative-convective model with an explicit hydrologic cycle. 1: Formulation and sensitivity to model parameters. *Journal of Geophysical Research*, 99(D7):14429–14441, July 1994.

[83] Jadwiga H. Richter and Philip J. Rasch. Effects of convective momentum transport on the atmospheric circulation in the Community Atmosphere Model, Version 3. *Journal of Climate*, 21:1487–1499, April 2008.

[84] Herbert Riehl and Joanne S. Malkus. On the heat balance in the equatorial trough zone. *Geophysica*, 6(3-4):503–537, 1958.

[85] D. Roche, D. Paillard, and E. Cortijo. Constraints on the duration and freshwater release of heinrich event 4 through isotope modelling. *Nature*, 432:379–382, November 2004.

[86] Nicolas Rochetin, Benjamin R. Lintner, Kirsten L. Findell, Adam H. Sobel, and Pierre Gentine. Radiative-convective equilibrium over a land surface. *Journal of Climate*, 27:8611–8629, December 2014.

[87] R. R. Rogers and M. K. Yau. *A Short Course in Cloud Physics*. Butterworth Heinemann, third edition, 1989.

[88] David M. Romps. Weak pressure gradient approximation and its analytical solutions. *Journal of the Atmospheric Sciences*, 69:2835–2845, September 2012.

[89] D. P. Rowell. Sources of uncertainty in future changes in local precipitation. *Climate Dynamics*, 39:1929–1950, 2012.

[90] Zuzana Rulfová and Jan Kyselý. Disaggregating convective and stratiform precipitation from station weather data. *Atmospheric Research*, 134:100–115, 2013.

[91] T. Schneider, P. A. O'Gorman, and X. J. Levine. Water vapor and the dynamics of climate changes. *Reviews of Geophysics*, 48(3), 2010.

[92] Courtney Schumacher and Robert A. Houze. Stratiform rain in the tropics as seen by the TRMM precipitation radar. *Journal of Climate*, 16:1739–1756, June 2003.

[93] William D. Sellers. A global climatic model based on the energy balance of the Earth-atmosphere system. *Journal of Applied Meteorology*, 8:392–400, 1969.

[94] Mrinal K. Sen and Paul L. Stoffa. Bayesian inference, Gibbs' sampler and uncertainty estimation in geophysical inversion. *Geophysical Prospecting*, 44:313–350, 1996.

[95] Sharon L. Sessions, Satomi Sugaya, David J. Randall, and Adam H. Sobel. Multiple equilibria in a cloud-resolving model using the weak temperature gradient approximation. *Journal of Geophysical Research*, 115, 2010.

[96] Len Shaffrey and Rowan Sutton. Bjerknes compensation and the decadal variability of the energy transports in a coupled climate model. *Journal of Climate*, 19:1167–1181, 2006.

[97] Steven C. Sherwood, Sandrine Bony, and Jean-Louis Defresne. Spread in model climate sensitivity traced to atmospheric convective mixing. *Nature*, 505:37–42, 2014.

[98] A. H. Sobel, G. Bellon, and J. Bacmeister. Multiple equilibria in a single-column model of the tropical atmosphere. *Geophysical Research Letters*, 34, 2007.

[99] Adam H. Sobel and Christopher S. Bretherton. Modeling tropical precipitation in a single column. *Journal of Climate*, 13:4378–4392, De-

cember 2000.

[100] Justin P. Stachnik and Courtney Schumacher. A comparison of the Hadley circulation in modern reanalyses. *Journal of Geophysical Research*, 116, 2011.

[101] J. Curt Stager, David B. Ryves, Brian M. Chase, and Francesco S. R. Pausata. Catastrophic drought in the Afro-Asian monsoon region during Heinrich Event 1. *Science*, 331:1299–1302, March 2011.

[102] Benjamin A. Stephens, Charles S. Jackson, and Benjamin M. Wagman. Effect of tropical non-convective condensation on uncertainty in modeled projections of rainfall. *Journal of Climate*, 32(19):6571–6588, October 2019.

[103] Thomas Stocker. *Introduction to Climate Modeling*. Springer, 2011.

[104] Henry Stommel. Thermohaline circulation with two stable regimes of flow. *Tellus*, 13(2):224–230, 1961.

[105] Rachel L. Storer, Guang J. Zhang, and Xiaoliang Song. Effects of convective microphysics parameterization on large-scale cloud hydrological cycle and radiative budget in tropical and midlatitude convective regions. *Journal of Climate*, 28:9277–9297, December 2015.

[106] Alan Thorndike. Multiple equilibria in a minimal climate model. *Cold Regions Sciene and Technology*, 76-77:3–7, 2012.

[107] Gabriel A. Vecchi and Brian J. Soden. Global warming and the weakening of the tropical circulation. *Journal of Climate*, 20:4316–4340, 2007.

[108] A. Villagran, G. Huerta, C. S. Jackson, and M. K. Sen. Computational methods for parameter estimation in climate models. *Bayesian Analysis*, 3:823–850, 2008.

[109] Benjamin M. Wagman. *Quantifying and constraining the cloud radiative feedback in perturbed physics Community Atmosphere Model ensembles*. PhD thesis, University of Texas at Austin, 2018.

[110] Benjamin M. Wagman and Charles S. Jackson. A test of emergent constraints on cloud feedback and climate sensitivity using a calibrated single-model ensemble. *Journal of Climate*, 31:7515–7532, September 2018.

[111] Benjamin M. Wagman and Charles S. Jackson. CAM5.3 single-model ensemble paper. *In preparation*, 2019.

[112] John M. Wallace and Peter V. Hobbs. *Atmospheric Science: An Introductory Survey*, volume 92 of *International Geophysics Series*. Academic Press, second edition, 2006.

[113] S. Wang and A. H. Sobel. Response of convective to relative sea surface temperature: Cloud-resolving simulations in two and three dimensions. *Journal of Geophysical Research*, 116, 2011.

[114] Shuguang Wang, Adam H. Sobel, and Ji Nie. Modeling the MJO in a cloud-resolving model with parameterized large-scale dynamics: Vertical structure, radiation, and horizontal advection of dry air. *Journal of Advances in Modeling Earth Systems*, 8:121–139, 2016.

[115] Warren M. Washington and Claire L. Parkinson. *An Introduction to Three-Dimensional Climate Modeling*. University Science Books, 2nd edition, 2005.

[116] Spencer R. Weart. *The Discovery of Global Warming, Revised and Expanded Edition*. Harvard University Press, 2008.

[117] D. Williamson. Exploratory ensemble designs for environmental models using k-extended Latin hypercubes. *Environmetrics*, 26:268–283, 2015.

[118] D. L. Williamson. The effect of time steps and time-scales on parametrization suites. *Quarterly Journal of the Royal Meteorological Society*, 139:548–560, 2013.

[119] C. J. Willmott and K. Matsuura. Terrestrial air temperature and precipitation: monthly and annual climatologies (version 3.01), 2000.

[120] R. C. Wills, M. P. Byrne, and T. Schneider. Thermodynamic and dynamic controls on changes in the zonally anomalous hydrological cycle. *Geophysical Research Letters*, 43:4640–4649, 2016.

[121] R. C. Wills, X. J. Levine, and T. Schneider. Local energetic constraints on Walker circulation strength. *Journal of the Atmospheric Sciences*, 74:1907–1922, 2017.

[122] Chester Wisner, H. D. Orville, and Carol Myers. A numerical model of a hail-bearing cloud. *Journal of the Atmospheric Sciences*, 29:1160–1181, September 1972.

[123] F. M. Woldemeskel, A. Sharma, B. Sivakumar, and R. Mehrotra. Quantification of precipitation and temperature uncertainties simulated by CMIP3 and CMIP5 ensembles. *Journal of Geophysical Research: Atmospheres*, 120:1–15, 2015.

[124] Carl Wunsch. Towards understanding the paleocean. *Quarternary Science Reviews*, 29:1960–1967, 2010.

[125] Shang-Ping Xie, Clara Deser, Gabriel A. Vecchi, Jian Ma, Haiyan Teng, and Andrew T. Wittenberg. Global warming pattern formation: sea surface temperature and rainfall. *Journal of Climate*, 23:966–986, February 2010.

[126] Ben Yang, Yun Qian, Guang Lin, L. Ruby Leung, Philip J. Rasch, Guang J. Zhang, Sally A. McFarlane, Chun Zhao, Yaocun Zhang, Hailong Wang, Minghuai Wang, and Xiaohong Liu. Uncertainty quantification and parameter tuning in the CAM5 Zhang-McFarlane convection scheme and impact of improved convection on the global circulation and

climate. *Journal of Geophysical Research: Atmospheres*, 118:395–415, 2013.

[127] Tokuta Yokohata, James D. Annan, Matthew Collins, Charles S. Jackson, Michael Tobis, Mark J. Webb, and Julia C. Hargreaves. Reliability of multi-model and structurally different single-model ensembles. *Climate Dynamics*, 39:599–616, 2012.

[128] L. Yu, X. Jin, and R. A. Weller. *Multidecade global flux datasets from the objectively analyzed air-sea fluxes (OAFlux) project: latent and sensible heat fluxes, ocean evaporation, and related surface meteorological variables.* Woods Hole Oceanographic Institution, Woods Hole, Massachusetts, OAFlux Project Technical Report. OA-2008-01 edition, 2008.

[129] G. J. Zhang and Norman A. McFarlane. Sensitivity of climate simulations to the parameterization of cumulus convection in the Canadian Climate Centre general circulation model. *Atmosphere-Ocean*, 33(3):407–446, 1995.

[130] Ming Zhao. An investigation of the connections among convection, clouds, and climate sensitivity in a global climate model. *Journal of Climate*, 27:1845–1862, March 2014.

Vita

Benjamin Andrew Stephens received a Bachelor of Arts in Anthropology from UT Austin in 2005 and a Master of Arts in International Relations from Boston University in 2009 before pursuing a career in physics. He earned his Bachelor of Science in Physics with Special Honors in 2011 from UT Austin. After working for two years in the office of then-Associate Dean of the College of Natural Sciences and Professor of Physics Sacha Kopp, Ben entered the Physics doctoral program at UT Austin. He worked on a project related to inflationary cosmology with the Weinberg Theory Group before shifting his focus to atmospheric physics in 2015. Starting spring 2020, he will be continuing work in atmospheric science as a Postdoctoral Research Associate at the University of Wisconsin Milwaukee Department of Mathematical Sciences.

Permanent address: benstephens@utexas.edu

This dissertation was typeset with LaTeX[†] by the author.

[†]LaTeX is a document preparation system developed by Leslie Lamport as a special version of Donald Knuth's TeX Program.